2021

# DEVELOPING ELECTROMAGNETIC AND PHOTONIC DEVICES BY USING ARTIFICIAL DIELECTRIC MATERIALS

Saeid Jamilan
*Michigan Technological University*, sjamilan@mtu.edu

# DEVELOPING ELECTROMAGNETIC AND PHOTONIC DEVICES BY USING ARTIFICIAL DIELECTRIC MATERIALS

By

Saeid Jamilan

A DISSERTATION

Submitted in partial fulfillment of the requirements for the degree of

DOCTOR OF PHILOSOPHY

In Electrical Engineering

MICHIGAN TECHNOLOGICAL UNIVERSITY

2021

This dissertation has been approved in partial fulfillment of the requirements for the Degree of DOCTOR OF PHILOSOPHY in Electrical Engineering.

Department of Electrical & Computer Engineering

Dissertation Advisor: *Elena Semouchkina*

Committee Member: *Durdu Guney*

Committee Member: *Warren F. Perger*

Committee Member: *Miguel Levy*

Department Chair: *Glen E. Archer*

# Table of Contents

# Author Contribution Statement

This dissertation includes the contents that have been published as journal and conference articles. Their citations are as follows.

(1) S. Jamilan, G. Semouchkin, N. P. Gandji, and E. Semouchkina, "Spatial Dispersion of Index Components Required for Building Invisibility Cloak Medium from Photonic Crystals," Journal of Optics, 20 (4), 045102, 2018.

(2) S. Jamilan and E. Semouchkina, "Employing GRIN PC-inspired Approach for Building Invisibility Cloak Media from Photonic Crystals," IEEE Photonics Conference, VA, USA, 2018.

(3) S. Jamilan and E. Semouchkina, "Using Self-collimated Wave-guiding in Invisibility Cloaks," SPIE Conference, Metamaterials XIII, 11769, 117690K, 2021.

(4) S. Jamilan and E. Semouchkina, "Collimation Effect in Strongly Modulated Anisotropic Photonic Crystals with Near-Zero Refractive Indices," CLEO: QELS_Fundamental Science, 2021.

(5) S. Jamilan, G. Semouchkin, N. P. Gandji, and E. Semouchkina, "Specifics of Scattering and Radiation from Sparse and Dense Dielectric Meta-surfaces," Journal of Applied Physics, 125 (16), 163106, 2019.

(6) S. Jamilan and E. Semouchkina, "Lattice Resonances in Metasurfaces Composed of Silicon Nano-Cylinders," 14th International Congress on Artificial Materials for Novel Wave Phenomena - Metamaterials, New York, USA, Sept. 28th – Oct. 3rd, 2020.

(7) S. Jamilan, G. Semouchkin, and E. Semouchkina, "Analog of Electromagnetically Induced Transparency in Metasurfaces Composed of Identical Dielectric Disks," Journal of Applied Physics, 129 (6), 063101, 2021.

Aforementioned publications were collaborative works. Saeid Jamilan, Dr. George Semouchkin, and Dr. Elena Semouchkina contributed to the theoretical analyses, numerical simulations, experimental measurements and writing of the manuscripts. Dr. Elena Semouchkina edited final text of all papers. Dr. Navid P. Gandji contributed for 1$^{st}$ and 5$^{th}$ papers in the list. For the 7$^{th}$ paper of the list, Fatemeh Safari collaborated in performing microwave experiments.

# Acknowledgements

I would like to express my sincere gratitude to my advisor, Prof. Elena Semouchkina, for mentoring me during my Ph.D. studies. I am thankful for her precious trust, support and guidance. Without these, I could not stand at this point today.

I would like to thank Dr. George Semouchkin for uncountable comments and helpful discussions that enriched many aspects of my research.

I would like to thank Dr. Durdu Guney, Dr. Warren Perger, and Dr. Miguel Levy for being members of my Ph.D. committee and for their time and valuable feedback.

I would like to acknowledge useful collaborations and helps of the research group's members: Dr. Xiaohui Wang, Dr. Ran Duan, Dr. Navid P. Gandji, Varsha Vijay Kumar, and Muhammad Danyal.

I would like to thank the chair, Dr. Glen E. Archer, and staff of Electrical Engineering Department of Michigan Tech and in particular, assistances of Laboratory Supervisors, Mr. Chuck Sannes and Mr. Mark Sloat, at developing and maintaining the experimental setups in Microwave Characteristics Lab.

I would like to acknowledge the financial supports provided by National Science Foundation throughout my Ph.D. studies and Finishing Fellowship awarded to me by Graduate School of Michigan Tech for 2021 Spring Semester.

I am deeply grateful to my dear father, mother, grandmother, and two beautiful sisters for unconditional support, love, and encouragement.

My life in the Upper Peninsula of Michigan at Michigan Technological University was an amazing journey and it was exceptionally rewarding.

## List of Abbreviations

| | |
|---|---|
| TO | Transformation Optics |
| PhC | Photonic Crystal |
| PC | Photonic Crystal |
| MM | Metamaterial |
| SRR | Split-Ring Resonator |
| GRIN | Graded Index |
| NZRI | Near-Zero Refractive Index |
| SC | Self-Collimation |
| TSCW | Total Scattering Cross Width |
| DR | Dielectric Resonator |
| MS | Metasurface |
| EDR | Electric Dipolar Resonance |
| MDR | Magnetic Dipolar Resonance |
| MQR | Magnetic Quadrupolar Resonance |
| KK | Kerker |
| FS | Forward Scattering |
| BS | Backward Scattering |
| LR | Lattice Resonance |
| RA | Rayleigh Anomaly |
| EIT | Electromagnetically Induced Transparency |

## Abstract

Transformation-Optics (TO) is a new theoretical tool that allows for designing advanced electromagnetic and photonic devices. TO theory often prescribes material parameters for transformed media that cannot be found in nature. Metamaterials (MMs) were initially used for realization of TO-based devices. However, conventional MMs possess noticeable losses caused by their metallic parts that prevents their utilization in optical range. Alternatively, photonic crystals (PhCs) formed from arrays of low-loss all-dielectric elements can be good substitutes for building TO-prescribed devices. Metasurfaces (MSs) comprised from 2D arrays of dielectric resonators (DRs) have been found as other promising candidates for realizing flat and efficient devices. In our work, we explored incorporation of all-dielectric artificial media in invisibility cloaks, representing the most exciting TO application, wave collimators, and MSs. We studied associated electromagnetic and photonic phenomena and solved engineering problems met at the development of device prototypes.

We designed and used anisotropic PhCs composed of rectangular lattice dielectric rod arrays to build up a cylindrical cloak medium realizing prescriptions of TO (Chapter 2). We also formed another cylindrical invisibility cloak by utilizing the self-collimation phenomenon in PhCs without considering TO prescriptions for turning the wave in the cloak medium (Chapter 3). Furthermore, we designed a wave collimator by employing high-anisotropic rectangular lattice dielectric rod arrays with unidirectional near-zero refractive indices (Chapter 4). Then, we studied the resonance and scattering responses of MSs composed of dielectric disks, while altering the periodicity of MSs. Our results demonstrated that periodicity of arrays has significant influence on defining the responses of MSs. (Chapter 5). Increasing lattice constants of dielectric MSs provided us with an opportunity to investigate interactions between lattice resonances (LRs) and dipolar electric and magnetic resonances that affected characteristics of MSs (Chapter 6). We analyzed the formation of Fano responses and wave interference processes in dense MSs to reveal the nature of electromagnetically induced transparency (EIT) that was detected at the frequency of electric dipolar resonance. (Chapter 7).

# 1 Introduction

## 1.1 Transformation Optics

Transformation optics (TO) was proposed and developed by Pendry et. al. in 2006 as a new method [1, 2] that enabled creation of electromagnetic and photonic devices, such as invisibility cloaks, lenses, and beam splitters, which control the properties of wave propagation in terms of direction, velocity, and phase [3, 4]. It is worth noticing that the roots of TO theory can be found in Einstein's theory of relativity [5]. Original form of Maxwell equations does not change in different coordinate systems. This provides an opportunity to manipulate the wave propagation by transforming the reference coordinate system into a new coordinate system. In any coordinate system, trajectories of electromagnetic wave are defined with respect to the geometry of the coordinate system. In a conventional Cartesian coordinate system, wave has a straight trajectory while in a new coordinate system with curved geometry obtained by transforming the original reference coordinate system, wave propagation follows curved paths [4]. Applying new and proper values of permittivity and permeability into the transformed space calculated by using specific mapping functions preserves the fundamental form-invariance of Maxwell equations. If the medium in the reference coordinate system of ($x$, $y$, $z$) has the relative permittivity and permittivity tensors of $\varepsilon$ and $\mu$ and the transformation medium has the relative permittivity and permeability tensors of $\varepsilon'$ and $\mu'$, the relation between reference and transformation media is given by TO theory as [3, 5]:

$$\varepsilon' = \frac{A \varepsilon A^T}{\det(A)} \tag{1.1}$$

$$\mu' = \frac{A \mu A^T}{\det(A)} \tag{1.2}$$

$A$ is Jacobina matrix that can be found as:

$$A = \begin{bmatrix} \frac{\partial x'}{\partial x} & \frac{\partial x'}{\partial y} & \frac{\partial x'}{\partial z} \\ \frac{\partial y'}{\partial x} & \frac{\partial y'}{\partial y} & \frac{\partial y'}{\partial z} \\ \frac{\partial z'}{\partial x} & \frac{\partial z'}{\partial y} & \frac{\partial z'}{\partial z} \end{bmatrix} \tag{1.3}$$

Material parameters prescribed by TO for the media of electromagnetic devices with unusual functionalities often appear anisotropic and spatially varying with singular values, i.e. near-zero values. Therefore, their realization is very challenging. Natural materials do not provide all required values of permittivity and permeability. They also have weak magnetic responses at high frequencies preventing them from providing relatively big permeabilities. Accordingly, artificial media have been designed and utilized for realization of various TO applications in recent years. In contrast to natural materials, artificial media such as metamaterials (MMs), which were the first candidates for TO-based applications, consist of specifically designed dielectric or metallic resonators, which represent meta-atoms [6, 7]. At electromagnetic resonances in meta-atoms, these media can exhibit unusual electromagnetic properties. While TO is a robust theoretical tool to advance electromagnetic and photonic devices, realization of TO-based devices urges designing artificial media which can satisfy TO prescriptions.

In this dissertation, we explore and design artificial media formed from all-dielectric materials for developing electromagnetic and photonic devices with advanced functionalities.

## 1.2 Invisibility Cloak

Invisibility cloak was proposed as the most exciting application of TO [1]. The invisibility cloak guides the incident wave around the hidden object without any reflection or scattering. Then, it reconstructs the original shape of the incident wave without casting shadows. Using TO approaches, it is possible to prescribe the material parameters of cloak media that will render the object invisible. In first attempt for realizing a TO-prescribed invisibility cloak media, MMs composed from metallic split-ring resonators (SRRs) were employed by Schurig et. al. [8] MMs are a class of artificial media that were realized in 2000 by Pendry and Smith et. al. [9, 10]. MMs could demonstrate unconventional electromagnetic characteristics such as negative refraction and backward wave propagation caused by simultaneous negativity of permeability and permittivity of the media [11, 12]. It is worth noticing that the concept of negative refractive index and its electrodynamic consequences were introduced earlier by Veselago in 1968 [13]. Conventional MMs are formed from arrays of metallic elements such as SRRs and cut wires and they can support formation of magnetic or/and electric resonances. Electromagnetic responses of MMs can be studied by using the effective medium theory [14]. According to the effective medium theory, if the size and periodicity of artificial media's unit cells are much smaller than the wavelength of incident wave, such medium can be considered as a homogenous medium and characterized in terms of effective permittivity ($\varepsilon_{\text{eff}}$) and effective permeability ($\mu_{\text{eff}}$). In SRRs, magnetic resonances are formed by the currents excited on the circumference of metallic rings and induce spectral changes of effective permeability that could be described as Lorentz-type resonances [9]. In addition, electric responses of cut wire arrays result in spectral variations of effective permittivity that were described with Drude model [15]. Changes of effective permittivity and permeability of MMs demonstrate extraordinary values such as negative, near-zero, or large positive values. However, resonant nature of these responses makes the performance of MMs very narrow-band.

According to TO approach employed in designing the cylindrical invisibility cloak media at TE polarized incidence in [8], these media should be prescribed a radial permeability (

$\mu_r$) dispersion with near-zero values rapidly increasing from inner to outer layers of cloak. The function of near-zero material parameters is to enhance phase velocity in the cloak media, realizing superluminal wave propagation. Inside the cloak, wave traverses a longer distance along curvilinear paths around the hidden object in comparison with the straight wave flow in free space. Superluminal wave propagation is necessary for compensating the phase mismatch between two aforementioned wave paths.

TO prescriptions in [8] also requested constant positive values for $\mu_\theta$ and $\varepsilon_z$ in the cloak media. In addition to accelerating the waves, cloak media with described above material parameters bends the wave flow around the hidden object. These two functions of cloak media are necessary for achieving wave-front reconstruction. It is worth noting that exact TO-prescribed $\mu_r$, $\mu_\theta$ and $\varepsilon_z$ distributions in the cylindrical cloak media are proportional to the ratio between the inner and outer radii of the cloak [8]. For realizing a TO-prescribed cylindrical cloak media in [8], SRRs with properly chosen parameters were arranged in the concentric circular layers around a metal cylinder. In the operating frequency range, SRRs could realize near-zero permeability values. Geometrical parameters of SRRs were slightly altered to gradually change the frequency of their magnetic resonances. This resulted in the changes of SRRs' effective permeability at the operating frequency of the cloak. Consequently, at the operating frequency, changes of effective material parameters of SRRs located in different layers could represent the TO prescriptions. Realized cloak could guide the incident microwave radiation around the hidden metal cylinder and reduce the scattering. However, significant losses attributed to the skin effect in metallic SRRs prevented implementation of such cloak at optical frequencies.

For decreasing the losses in the cloak media, it was proposed to use all-dielectric MMs instead of structures such as metallic SRRs. The cloaks presented in [16, 17] were composed from arrays of glass or ceramic cylinders and were capable of operating in, respectively, infrared and microwave regimes. In these cloaks, gradual shift of magnetic resonance frequency through neighboring circular layers was achieved by varying the air gaps between identical deictic resonators in arrays. Diameter of hidden metal cylinder was several times bigger than wavelength of incident wave while obtained cloaking effect was also narrowband because of resonant nature of all-dielectric MMs.

Further intriguing works [18-20] showed that low-loss all-dielectric photonic crystals (PhCs) can be promising candidates for realization of material properties requested by TO. PhCs, i.e. photonic bandgap materials, are a category of artificial structures formed from periodic elements. PhCs were introduced by Sajeev John and Eli Yablonovitch in 1987 [21]. They have been employed in designing numerous photonic devices such as waveguides, modulators, lenses, and multiplexers [22]. PhCs' electromagnetic responses are attributed to their periodicity while the periodicity of a PhC can be along one or more axes. In contrast to MMs, periodicity of PhCs elements can be comparable with the wavelength of incident wave. Therefore, they do not have the problem of homogenization.

PhCs can be characterized by using their dispersion diagrams depicting the dependencies between frequency and wave number. Emergence of band gaps when transmission is prohibited inside the PhC at a specific range of frequencies, is also detectable in dispersion diagrams. Refractive indices of PhCs can be calculated based on their dispersion data. Notomi showed that PhCs are capable of providing negative, near-zero, and positive values of refractive indices in their transmission bands [23]. It was also shown that PhCs can demonstrate the phenomenon of self-collimation (SC) [22, 24]. Direction of self-collimated wave movement is defined with respect to the crystallographic axis of the lattice and by gradually changing the orientation of unit cells, it is possible to control the wave path. SC phenomenon expands perspectives for using PhCs at designing electromagnetic and photonic devices [25].

In [19], it was shown that a low-loss dielectric cloak media built from bilayer PhCs could bend a gaussian beam around the hidden object. However, proposed cloak media was not operating under plane wave illumination and did not result in a significant cloaking effect. In a later work of our team [26], a novel TO-based cylindrical invisibility cloak media was designed by using 2D PhCs composed from dialectic rod arrays. For realization of the cylindrical cloak media by using PhCs characterized by dispersion diagrams and refractive indices, TO-prescribed material parameters were recalculated in the terms of azimuthal and radial components of refractive index. Azimuthal component of index dispersion had to have superluminal indices (near-zero values) while values of radial component had to be bigger than unity. As described earlier, near-zero indices are necessary for accelerating wave propagation in the cloak media and obtaining phase-matching and flat wave-front beyond the cloak. Meanwhile, bigger than unity radial indices are expected to result in turning the wave trajectories in the cloak media around the hidden object.

PhCs made from square lattice arrays of dielectric rods were found capable of providing near-zero refractive indices in the lower edge of their 2$^{nd}$ transmission band. Square lattice PhC fragments with properly chosen lattice constants were coiled around a metal cylinder to realize TO-prescribed azimuthal indices in the cloak media at an operating frequency corresponding to PhCs' 2$^{nd}$ transmission bands. Gradually altering the lattice constants of PhC fragments provided an opportunity to slightly shift the frequencies of their 2$^{nd}$ transmission bands and approximate TO-prescribed azimuthal index changes in the cloak media at a specific operating frequency. Simulated field patterns of the cloak media confirmed that it could guide the wave path around hidden metal cylinder at an operational frequency. Obtained results demonstrated that PhCs composed from dielectric rod arrays can be used for realizing invisibility cloak. However, employing square lattice dielectric rod arrays with near-zero indices could not satisfy the TO-prescribed bigger than unity radial indices in the cloak media. Metal cylinder's scattering cross width was not decreased significantly and shadows were observed in the wave-front beyond the cloak. Accordingly, it appeared imperative to look for other opportunities to design a new PhC-based media that can realize both TO-prescribed azimuthal and radial index dispersions, i.e. anisotropic index distribution. Furthermore, possible contribution of SC phenomenon in PhC-based cloak media for turning the wave around hidden object at absence of TO-prescribed radial indices, had to be investigated.

## 1.3 Dielectric Metasurfaces

Another artificial media composed of periodic arrays of dielectric resonators (DRs) are planar 2D metasurfaces (MSs), which have been designed in recent years to realize flat and efficient components for electromagnetic and optical devices with important functions such as beam steering, wave-front manipulation, tailored directional scattering, lensing, sensing, and holography [27-30]. Dielectric MSs are comprised from same constituents as dielectric MMs and PhCs and their development requires investigating the electromagnetic characteristics of DRs. In a study published by Kerker et. al. in 1983, it was shown that for a hypothetical particle, if $\varepsilon=\mu$, backward-scattering (BS) will be totally diminished providing forward-scattering (FS) [31]. This phenomenon could not attract attentions because its realization demanded having access to components with both electric and magnetic responses. An opportunity for realization of so-called 1st Kerker effect and directional scatterings was found in recent years at employing subwavelength DRs [32-37]. DRs support formation of Mie resonances that were studied by Gustav Mie. Interplay between radiations of different Mie resonances including dipolar magnetic and electric resonances (MDR and EDR), quadrupolar magnetic resonance (MQR) and other higher-order resonances governs scatterings of DRs [38]. In particular, destructive interreferences between radiations of MDR and EDR of a single dielectric sphere, suppresses the backward scattering (BS) and only allows forward scattering (FS). This intriguing phenomenon realizes the so-called 1st Kerker effect at an off-resonance frequency which is smaller than MDR's frequency. Kerker effect was confirmed with experimental measurements carried out for dielectric spheres operating in microwaves (mm-sized sphere) [33].

EDRs in DRs are formed due to boundary between dielectric and air and enhancement of electric field in central area of DR. If wavelength of wave inside DR is comparable to the size of DR, displacement currents induced by electric field will form loops in DR. These loops of displacement currents excite MDRs in DRs [39]. In a single subwavelength dielectric sphere, MDR and EDR are spectrally separated while MDR appears at a frequency smaller than EDR's frequency. Meanwhile, 1st Kerker effect happens in longer-wavelength side of spectrum. Considering that frequency of 1st Kerker effect is corresponding to the tails of EDR and MDR, the power scattered in forward direction (FS) is very small. Scattering is maximal at the frequencies of Mie resonances peaks. At respective frequencies, BS and FS values are similar and therefore, directional scattering cannot be achieved. One possible approach for enhancing the FS that is necessary for realizing efficient devices, could be shifting the frequency of 1st Kerker effect towards frequencies of Mie resonances peaks.

It was shown that in dielectric cylinders, changing the height/diameter ratio provides an opportunity for adjusting the spectral distance between MDR and EDR [40]. In particular, Staude et. al. proposed that when cylinder's dimeter was approximately double the height, frequencies of MDR and EDR were overlapping [41]. Then, it was suggested that coincidence of MDR and EDR leads to formation of 1st Kerker effect at the same overlapping frequency providing a maximal FS. However, resonant responses of DRs with overlapping EDR and MDR demanded further analyzes because coincidence of EDR and MDR was expected to perturb their normal formation inside DR.

Dielectric MSs are comprised from various meta-atoms arranged in a periodic lattice while each meta-atom is composed of one or several DRs. Geometrical design and permittivity of meta-atoms are adjusted to control their resonant responses affecting phase change of transmitted wave at frequency of 1st Kerker effect where there is a high transmission ratio. In particular, MDR or EDR produce π radians phase change [27]. Staude et. al. suggested that overlapping MDR and EDR in dielectric disks can combine their effects at changing the phase-shift of transmitted waves and extend it to 2π radians at the frequency of MDR and EDR coincidence [41]. Effects of lattice periodicity on responses of MSs have not been typically considered in design procedure of MSs. Authors of these works speculated that Mie resonances are confined inside DRs and coupling effects between resonators can be ignored. They assumed that electromagnetic responses of arrays can be characterized by responses of single "meta-atoms. It is essential to investigate the effect of periodicity on the responses of MSs. Specifically, characteristics of 1st Kerker effect and directional scatterings from MSs composed of DRs arrays at changing the periodicity have to be explored.

## 1.4 Objectives

Development of low-loss electromagnetic and photonic applications by employing all-dielectric artificial media is the primary goal of this dissertation. We worked on finding the solutions to the problems revealed in published literature and described in previous sections. We were able to develop invisibility cloaks and collimators using rectangular lattice arrays of low-loss dielectric rod. Our results revealed that anisotropic rectangular lattice PhCs can provide TO-requested material characteristics. Furthermore, we studied electromagnetic responses of DRs, in particular dielectric cylinders, and MSs in the terms of resonance, scattering, radiation, transmission, and phase. In our studies, we altered the height/diameter ratio of dielectric disks and periodicity of MSs.

Employing square lattice PhCs with superluminal indices in the cylindrical invisibility cloak media could not realize TO-prescribed radial index dispersion with bigger than unity values. The goal of the work presented in Chapter 2 was realizing both TO-prescribed distributions of azimuthal and radial refractive index components in the cylindrical invisibility cloak media by using anisotropic PhCs. We studied frequency dependencies of the directional refractive indices of PhCs composed of rectangular lattice dielectric rod arrays and observed that they were comparable with TO-prescriptions at a frequency range corresponding to 2nd transmission band of the PhCs. Our results demonstrated that in a suitable frequency range for the TM polarized waves moving along short side of the cells in rectangular lattice PhCs, indices could have near-zero values while for the wave propagation along long side of the cells, indices appeared bigger than unity. We built up cylindrical cloak media employing fragments of concentric dielectric rod arrays with rectangular lattices coiled around a metal cylinder. We faced challenges at approximating the TO prescribed anisotropic index dispersions with PhC fragments in the cylindrical cloak media for several reasons. TO prescribed relatively big radial indices in inner layers of the cloaks with acceptable thicknesses that exceeded degree of index anisotropy attainable in rectangular lattice PhCs. In addition, it was cumbersome to mimic steep changes of index dispersions in the cloak media at incorporating PhC fragments. We could propose proper solutions for these challenges. Our cloak media formed using rectangular lattice dielectric rod arrays led to wave-front restoration beyond the cloak and reduction of total scattering cross-width (TSCW) of hidden metal cylinder.

In Chapter 3, we used self-collimation (SC) phenomenon instead of realizing TO prescribed indices, in particular difficult bigger than unity radial indices, in a cylindrical invisibility cloak media. SC effect in a bent square lattice dielectric PhC fragment allowed for turning the wave around the hidden object. Employment of self-collimated waveguiding to bend the wave path in the cloak medium requested transforming the straight wave paths in free space into circular wave movement in the cloak. A specific TO approach was used to design transformation areas at the beginning and end of SC part in the cloak. We found proper index dispersions for transformation parts of the cloak and realized them by using rectangular lattice dielectric rod arrays. Our proposed SC-based cloak media provided a significant unidirectional cloaking effect.

In Chapter 4, we explored collimation effect in high-anisotropic rectangular lattice PhCs with near-zero indices and presented an application for it. We showed that in rectangular lattice dielectric rod arrays with properly selected lattice parameters, superluminal propagation with near-zero refractive indices could be formed along short side of the cells while propagation along long side of the cells was fully suppressed. Operating frequency was correlated with the lower edge of $2^{nd}$ transmission band. The proposed media could effectively collimate a divergent incident radiation at the operating frequency.

In Chapter 5, we investigated resonance phenomena in dielectric MSs. We studied interactions between electric and magnetic resonances inside single DRs and their effects on directional scatterings. We altered height/diameter ratio in a single dielectric disk and could study the responses at varying the spectral distance between peak frequencies of magnetic and electric dipolar resonances. Most substantial directional scattering, i.e. optimum $1^{st}$ Kerker effect, could be obtained when MDR and EDR were not overlapping. We also studied the couplings between DRs inside the arrays in MSs. In particular, we analyzed the effects of periodicity in dense and sparse arrays on responses of MSs. Our obtained results revealed that characteristics of dense MSs in the terms of resonances and scatterings have significant differences in comparison with MSs having sparse arrays. In densely composed MSs, dipolar electric resonance was correlated with a narrow-band full transmission. It is worth noting that dipolar resonances are conventionally reflective. We performed our analysis for both optical and microwave MSs comprised of, respectively, silicon nano-disks and ceramic mm-sized disks and revealed that their responses are analogous.

In Chapter 6, we investigated the formation of lattice resonances (LRs) in MSs comprising arrays of dielectric disks, which appear due to in-plane propagation of surface waves at normal wave incidence. We widely extended the periodicity of arrays to study the interactions between LRs and elementary Mie resonances in vicinity of Rayleigh anomaly (RA) area where array's periodicity was comparable with the wavelength of incident wave. We described the responses of MSs including resonance, transmission, and reflection spectra and 1$^{st}$ Kerker effect in the presence of LRs. LR formation excited high-intensity field spots nearby DR edges in the gaps between DRs that could be responsible for red shifting of electric and magnetic dipolar resonances at approaching RA condition.

The goal of Chapter 7 was to explore the nature of extraordinary narrow-band transmission that was detected at the dipolar electric resonances in dense MSs composed from dielectric disks. The response was analogous of electromagnetically induced transparency (EIT) initially observed in atomic systems. We studied destructive and constructive processes between resonant fields and incident wave fields and formation of Fano resonances in dense MSs to reveal the nature of this promising effect. Analyzing the electric field intensity and phase signals at specific spatial points disclosed the competing processes that shaped the Fano responses and led to realization of conditions providing transparency of the MS.

## References


1. J. B. Pendry, D. Schurig, and D. R. Smith, “Controlling electromagnetic fields,” Science, 312, 1780-1782, 2006.

2. D. Schurig, J. B. Pendry, and D. R. Smith, “Calculation of material properties and ray tracing in transformation media,” Opt. Express, 14, 9794-980, 2006.

3. N. B. Kundtz, D. R. Smith, J. B. Pendry, “Electromagnetic design with transformation optics,” Proc. of the IEEE, 99 (10), 1622 – 1633, 2011.

4. F. Sun, B. Zheng, H. Chen, W. Jiang, S. Guo, Y. Liu, Y. Ma, and S. He, “Transformation Optics: From Classic Theory and Applications to its New Branches,” Laser & Photonics Reviews, 11, 1700034, 2017.

5. J. B. Pendry, “Transformation optics and the near field,” in “Roadmaps on transformation optics,” Edited by: Martin McCall, J. Opt., 20, 063001, 2018.

6. N. Engheta and R. W. Ziolkowski, “Metamaterials: Physics and Engineering Explorations,” Wiley-IEEE Press, 2006.

7. R. Liu, T. J. Cui, D. H., B. Zhao, and D. R. Smith, “Description and explanation of electromagnetic behaviors in artificial metamaterials based on effective medium theory,” Phys. Rev. E, 76, 026606, 2007.

8. D. Schurig, J. J. Mock, B. J. Justice, S. A. Cummer, J. B. Pendry, A. F. Starr, and D. R. Smith, “Metamaterial Electromagnetic Cloak at Microwave Frequencies,” Science, 10, pp. 977-980, 2006.

9. J. B. Pendry, A. J. Holden, D. J. Robbins, and W. J. Stewart, “Magnetism from conductors and enhanced nonlinear phenomena,” IEEE Transactions on Microwave Theory and Techniques, 47, 2075-2084, 1999.

10. D. R. Smith, W. J. Padilla, D. C. Vier, S. C. Nemat-Nasser, and S. Schultz, “Composite Medium with Simultaneously Negative Permeability and Permittivity,” Physical Review Letters. 84 (18), 4184–87, 2000.

11. J. B. Pendry, “Negative Refraction Makes a Perfect Lens,” Phys. Rev. Lett., 85, 3966, 2000.

12. R. A. Shelby, D. R. Smith, and S. Schultz, “Experimental verification of a negative index of refraction,” Science, 292 (5514), 77-79, 2001.

13. V. G. Veselago, “The electrodynamics of substances with simultaneously negative values of ε and μ”. Physics-Uspekhi., 10 (4), 509–514, 1968.

14. D. R. Smith, D. C. Vier, Th. Koschny, and C. M. Soukoulis, “Electromagnetic parameter retrieval from inhomogeneous metamaterials,” Phys. Rev. E, 71, 036617, 2005.

15. J. D. Jackson, “Classical Electrodynamics,” 3rd edition, Published by John Wiley and Sons, 1998.

16. E. Semouchkina D. H. Werner, G. B. Semouchkin, and C. Pantano, “An infrared invisibility cloak composed of glass” Appl. Phys. Lett., 96 (23), 233503, 2010.

17. X. Wang, F. Chen and E. Semouchkina, “Implementation of low scattering microwave cloaking by all-dielectric metamaterials,” IEEE Microwave Compon. Lett., 23 (2), 63–65, 2013.

18. D. Xiao and H. T. Johnson, “Approximate optical cloaking in an axisymmetric silicon photonic crystal structure,” Opt. Lett., 33, 860-862, 2008.

19. Y. A. Urzhumov and D. R. Smith “Transformation Optics with Photonic Band Gap Media,” Phys. Rev. Lett., 105, 163901, 2010.

20. A. Hosseinzadeh and E. Semouchkina “Effect of permittivity on energy band diagrams of dielectric metamaterial arrays” Microwave Opt. Technol. Lett., 55 134–137, 2013.

21. E. Yablonovitch, “Inhibited Spontaneous Emission in Solid-State Physics and Electronics,” Physical Review Letters, vol. 58, no. 20, pp. 2059-2062, 1987.

22. J. D. Joannopoulos, S. G. Johnson, J. N. Winn, and R. D. Meade, “Photonic Crystals,” Princeton: Princeton University Press, 2011

23. M. Notomi, “Theory of light propagation in strongly modulated photonic crystals: refraction like behavior in the vicinity of the photonic band gap,” Phys. Rev. B, 62, 10696–705, 2000.

24. R. C. Rumpf, J. Pazos, C. R. Garcia, L. Ochoa, and R. Wicker, “3D printed lattices with spatially variant self-collimation,” Progress In Electromagnetics Research, 139, 1–14, 2013.

25. M. Noori, M. Soroosh, H. Baghban, “Self-collimation in photonic crystals: applications and opportunities,” Annalen der Physik, 530, 1700049, 2018.

26. E. Semouchkina, R. Duan, N. P. Gandji, S. Jamilan, G. Semouchkin, and R. Pandey, “Superluminal media formed by photonic crystals for transformation optics-based invisibility cloaks,” J. Opt., 18, 044007, 2016.

27. Y. F. Yu, A. Y. Zhu, R. Paniagua-Domınguez, Y. H. Fu, B. Luk’yanchuk, and A. I. Kuznetsov, “High-transmission dielectric metasurface with 2π phase control at visible wavelengths,” Laser Photonics Rev., 9 (4), 412–418, 2015.

28. E. Arbabi, A. Arbabi, S. M. Kamali, Y. Horie, and A. Faraon, “Multiwavelength polarization-insensitive lenses based on dielectric metasurfaces with meta-molecules,” Optica, 3, 628-633, 2016.

29. W. Zhao, H. Jiang, B. Liu et. al., “Dielectric Huygens’ metasurface for high-efficiency hologram operating in transmission mode,” Sci. Rep., 6, 30613, 2016.

30. P. Genevet, F. Capasso, F. Aieta, M. Khorasaninejad, and R. Devlin, “Recent advances in planar optics: from plasmonic to dielectric metasurfaces,” Optica, 4, 139–52, 2017.

31. M. Kerker, D.-S. Wang, and C. L. Giles, “Electromagnetic scattering by magnetic spheres,” J. Opt. Soc. Am., 73, 765–767, 1983.

32. R. Gomez-Medina, B. Garcia-Camara, I. Suarez-Lacalle, F. González, F. Moreno, M. Nieto-Vesperinas, and J. J. Saenz, “Electric and magnetic dipolar response of germanium nanospheres: interference effects, scattering anisotropy, and optical forces,” J. of Nanophotonics, 5 (1), 053512, 2011.

33. J. Geffrin, B. García-Cámara, and R. Gómez-Medina et. al. “Magnetic and electric coherence in forward- and back-scattered electromagnetic waves by a single dielectric subwavelength sphere,” Nat. Commun., 3, 1171, 2012.

34. B. S. Luk’yanchuk, N. V. Voshchinnikov, R. Paniagua-Domínguez, and A. I. Kuznetsov, “Optimum forward light scattering by spherical and spheroidal dielectric nanoparticles with high refractive index,” ACS Photonics, 2, 993–995, 2015.

35. A. I. Kuznetsov, A. E. Miroshnichenko, M. L. Brongersma, Y. S. Kivshar, and B. Luk’yanchuk, “Optically resonant dielectric nanostructures,” Science, 354, 6314, 2016.

36. S. Person, M. Jain, Z. Lapin, J. J. Sáenz, G. Wicks, and L. Novotny, “Demonstration of zero optical backscattering from single nanoparticles,” Nano Lett., 13, 1806–1809, 2013.

37. Y. H. Fu, A. I. Kuznetsov, A. E. Miroshnichenko, Y. F. Yu, and B. Luk'yanchuk, "Directional visible light scattering by silicon nanoparticles," Nat. Commun., 4, 1527, 2013.

38. W. Liu and Y. S. Kivshar, "Generalized Kerker effects in nanophotonics and meta-optics," Opt. Express, 26 (10), 13085–13105, 2018.

39. Y. Kivshar and A. Miroshnichenko, "Meta-Optics with Mie Resonances," Optics & Photonics News, 28 (1), 24-31, 2017.

40. A. B. Evlyukhin, C. Reinhardt, and B. N. Chichkov, "Multipole light scattering by nonspherical nanoparticles in the discrete dipole approximation," Phys. Rev. B, 84, 235429, 2011.

41. I. Staude, A. E. Miroshnichenko, M. Decker, N. T. Fofang, S. Liu, E. Gonzales, J. Dominguez, T. S. Luk, D. N. Neshev, I. Brener, and Y. Kivshar, "Tailoring directional scattering through magnetic and electric resonances in subwavelength silicon nanodisks," ACS Nano, 7 (9), 7824–7832, 2013.

# 2 Realization of TO-based Invisibility Cloak with Rectangular Lattice Photonic Crystals

## 2.1 Spatial Dispersion of Index Components Required for Building Invisibility Cloak Medium from Photonic Crystals[1]

### 2.1.1 Introduction

Transformation optics (TO) has opened new perspectives for designing advanced electromagnetic (EM) devices with superior functionalities [1]. TO employs coordinate transformations to control EM wave paths by imposing specific spatial dispersion of the media parameters [2]. Coordinate transformations can be derived for compressing, expanding, or bending space, enabling designs of invisibility cloaks, field concentrators, perfect lenses, beam shifters, etc. Realization of these devices, however, depends on the possibility to create transformation media with prescribed properties [3], which include highly anisotropic dispersion of material parameters, as well as parameters providing wave propagation with superluminal phase velocities. Therefore, metamaterials (MMs), which were expected to exhibit most versatile properties, were considered as first candidates for realizing TO-based devices [4, 5]. Application of conventional MMs composed of spilt ring resonators and cut wires, however, met serious challenges, such as increased losses in metal elements at higher frequencies, extremely narrow frequency band of operation, inter-resonator coupling, and the need to provide homogenization. In order to decrease losses, dielectric MMs, instead of metal ones, were used for developing invisibility cloaks for infrared range [6, 7]. However, resolving all of the above listed problems would require substituting MMs in the cloak media by alternative materials. Photonic crystals (PhCs) could be considered as promising substitutes [8].

In [9] it was shown that the cloak medium, formed from fragments of 2D photonic crystals composed of dielectric rods, supported wave propagation around metal cylinder with superluminal phase velocity that provided wave-front restoration beyond the target. These results have demonstrated the perspectives of PhC applications in transformation media, although used in [9] crystals with square lattices could not provide TO-requested asymmetry of spatial index dispersion. It is worth noting that one complication with building a cloak from PhCs was that the number of periods required to form the band structures in PhC fragments affected the minimum volume of the cloak. In addition, boundaries between PhC fragments in the cloak medium could contribute to reflections.

---

[1]Reprinted from 'S. Jamilan, G. Semouchkin, N. P. Gandji, and E. Semouchkina, "Spatial Dispersion of Index Components Required for Building Invisibility Cloak Medium from Photonic Crystals," Journal of Optics, 20 (4), 045102, 2018'; with permission from © IOP Publishing.

However, as it was shown in [9], the problems of both reasonable cloak thickness and excessive reflections could be solved by properly designing the cloak.

In this work, we, first, investigate the roles of spatial dispersions prescribed for orthogonal index components on the performance of cylindrical invisibility cloaks that allows for relating successful operation of PhCs-based cloak in [9] to the phenomenon of self-collimation (Section 2). Then we explore the opportunity to realize TO-requested asymmetry of dispersion laws for orthogonal index components by forming the cloak medium from anisotropic 2D PhCs with rectangular lattices of dielectric rods. We show that, although TO-prescribed index dispersion asymmetry could be qualitatively achieved in these PhCs, providing the exact TO-prescribed index values by varying parameters of rod arrays in practically acceptable ranges presents a serious challenge (Sections 3 and 4). To solve the problem, we propose reduced prescriptions for spatial dispersion of radial component of index, which are compatible with capabilities of PhCs. We demonstrate that following these prescriptions does not cause significant changes in the cloak performance compared to performance of the cloak medium with parameters satisfying full TO prescriptions (Section 5). The results of full-wave field simulations presented in this work were obtained by using COMSOL Multiphysics software package, while dispersion diagrams for PhCs were calculated by using last versions of MPB software developed at MIT [10].

### 2.1.2 TO-based Prescriptions for Orthogonal Index Components and Functions of These Components in the Cylindrical Cloak Medium

TO-prescriptions for the effective parameters, permittivity and permeability, of a cylindrical cloak medium have been originally proposed in [1] and later modified in [11], to avoid impedance mismatch at the outer boundary of the cloak. In order to form the cloak medium from PhCs instead of MMs, TO-prescriptions need to be re-formulated for radial and azimuthal index components of refractive index [8]. Following our earlier work [9], here we consider prescriptions to be defined by a coordinate transformation, which shrinks infinitely long cylindrical space, represented in cylindrical coordinate system by radius $r'$, into an annular cylindrical space, represented by radius $r$:

$$r = f(r') = \left(1 - \frac{R_{\text{in}}}{R_{\text{out}}} + \frac{R_{\text{in}}}{R_{\text{out}}^2}(r' - R_{\text{out}})\right) r' + R_{\text{in}} \ ; \ \ \theta = \theta' \ ; \ \ z = z' \qquad (1)$$

where $0 \leq r' \leq R_{\text{out}}$ and $R_{\text{in}} \leq r \leq R_{\text{out}}$, while the values $R_{\text{in}}$ and $R_{\text{out}}$ are, respectively, the inner and the outer radii of the cloaking shell (Fig. 1 (a)). At TM polarization of incident waves (magnetic field directed along $z$-axis of the cylindrical cloak), prescriptions for effective permeability of the cloak medium could be reduced to $\mu_z = 1$ [5], while for the components of effective permittivity in E-field plane (normal to the cloak axis) following expressions could be obtained following [11]:

$$\varepsilon_r = \left(\frac{r'}{r}\right)^2 \; ; \; \varepsilon_\theta = \left(\frac{df(r')}{dr'}\right)^{-2} \tag{2}$$

Expressions (2) could be then used to derive index components for wave propagation in azimuthal and radial directions (Fig. 1 (a)) by utilizing dependencies of these components on effective parameters of the medium: $n_r = \sqrt{\varepsilon_\theta \mu_z}$ and $n_\theta = \sqrt{\varepsilon_r \mu_z}$. Accordingly, we obtain:

$$n_r = \left(1 - \frac{2R_{\text{in}}}{R_{\text{out}}} + \frac{2R_{\text{in}}r'}{R_{\text{out}}^2}\right)^{-1} \tag{3}$$

$$n_\theta = \frac{r'}{r} \tag{4}$$

where $r'$ could be found from equation (1) as following:

$$r' = \frac{2R_{\text{in}}R_{\text{out}} - R_{\text{out}}^2 + R_{\text{out}}^2\sqrt{\left(1 - \frac{2R_{\text{in}}}{R_{\text{out}}}\right)^2 - \frac{4R_{\text{in}}}{R_{\text{out}}^2}(R_{\text{in}} - r)}}{2R_{\text{in}}} \tag{5}$$

Equations (3-5) could be used for calculating prescribed by TO spatial dispersions of index components. Curves A and F in Fig. 1 (b) present these dispersions for a cloaking shell having $\frac{R_{\text{out}}}{R_{\text{in}}} = 3.5$, which is hiding the target with the diameter of 74 mm. As seen in the figure, TO prescribes ascending dispersion from inner to outer cloak layers (curve A) for azimuthal index component and descending dispersion (curve F) for radial index component. In addition, azimuthal index component should have values less than 1 within the entire cloak, i.e. these values should support wave propagation with superluminal phase velocities, while radial index component, just opposite, should be higher than 1, i.e. its values should support refraction phenomena, turning waves around the cloak axis.

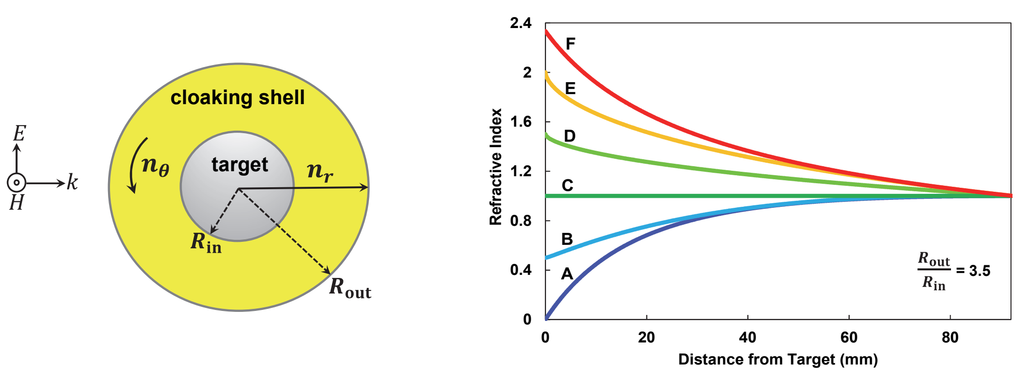


(a) (b)

Figure 1. (a) Cross-section of cylindrical cloak and (b) various spatial distributions of index within cloaking shell with $\frac{R_{\text{out}}}{R_{\text{in}}} = 3.5$.

Considering the described above functions of two index components caused by their specific spatial dispersions, it could be suggested that employing PhCs with square lattices in the cloak medium, as in [9], should exclude obtaining the cloaking effect. In fact, providing superluminal index values in azimuthal direction in PhCs with square lattices had to introduce similar values for indices in radial direction. Fig. 2 (a) presents the wave pattern simulated for the cloak model with identical dispersions of index components in two directions (corresponding to curve A in Fig. 1 (b)). The frequency of 11.4 GHz was taken arbitrary, since index values in the model were taken to be frequency-independent. As seen in the figure, a typical shadow behind the metal target is observed instead of the cloaking effect. Wave-patterns presented in Figs. from 2 (b) to 2 (f) correspond to the cloak models with dispersions for radial index component changing from curve B to curve F in Fig. 1 (b), respectively, while dispersion for azimuthal index component was kept as curve A in Fig. 1 (b). It can be seen that significant decrease of the shadow occurred only at radial index values exceeding 1 (and essentially exceeding 1 near the target) with radial dispersion approaching curve F in Fig. 1 (b). It is obvious from the obtained results that the media with dispersions following curve A for both index components should not provide the cloaking effect, unless any other physical mechanism, instead of refraction, can support wave turning around the target.

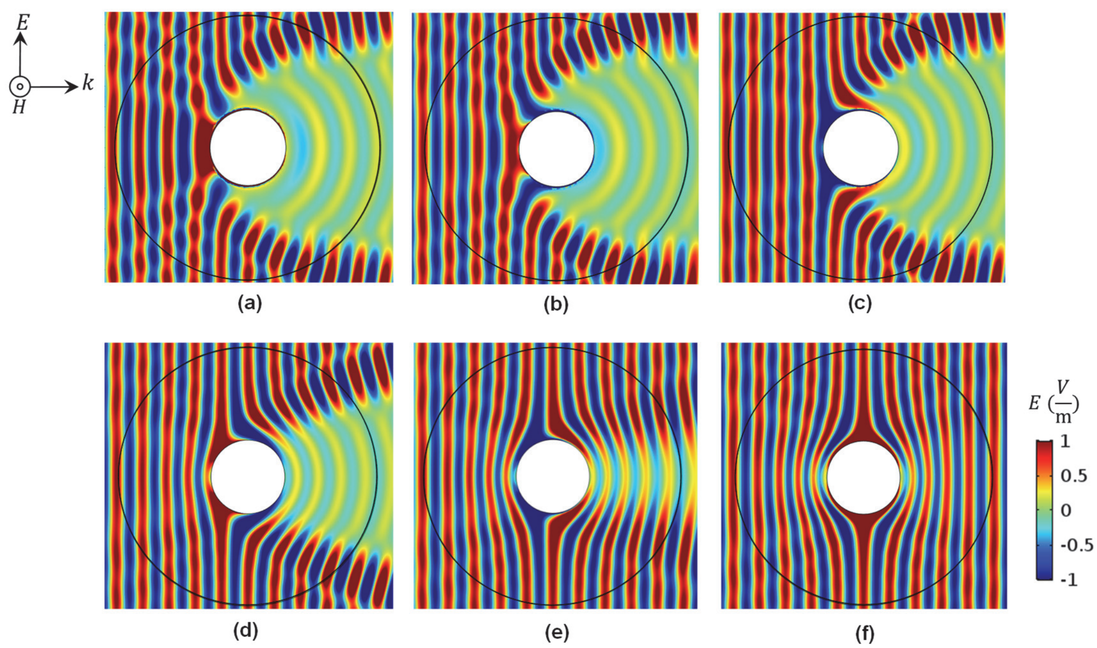


Figure 2. Simulated wave patterns at 11.4 GHz for the cloak with $\frac{R_{\mathrm{out}}}{R_{\mathrm{in}}} = 3.5$ for (a) curve A in Fig. 1 (b) as radial and azimuthal index dispersions; (b), (c), (d), (e), and (f): curve A as azimuthal index dispersion, while radial index dispersion is following curves B, C, D, E, and F in Fig. 1 (b), respectively.

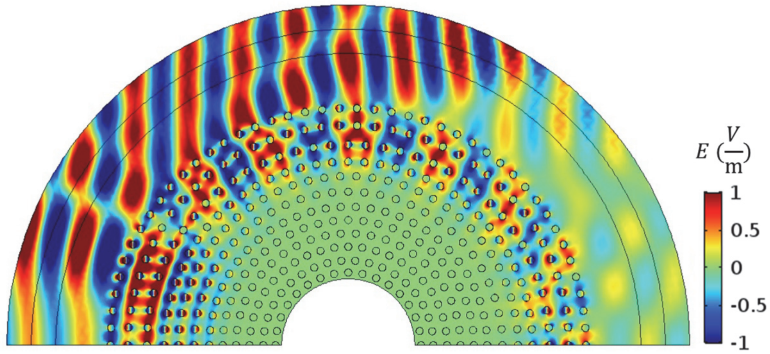


Figure 3. Wave-pattern for the cloak in [9] formed from square-lattice PhCs demonstrates the effect of self-collimation at 13.6 GHz.

This mechanism could be related to the known in PhCs phenomenon of self-collimation. According to [12], due to this phenomenon, PhCs could support wave propagation along crystallographic axes, even if they are bent. Indeed, Fig. 3 taken from a row of images of wave-patterns in [9] just demonstrates self-collimated wave movement in outer PhC layers of the cloak, while beyond the cloak, a shadow similar to that presented in Fig. 2 (a) can be clearly seen. This observation opens up an opportunity for employing self-collimation in PhCs for providing TO-requested functionalities of the cloak medium, when prescriptions for material properties could not be realized in full.

### 2.1.3 Achieving Anisotropic Index Dispersion in PhC-based Cloak Media

As it was shown in Section 2, if self-collimation is not realized in the cloak medium formed by PhCs with square lattices, cloaking effect could not be observed in such medium, since TO-prescribed difference between spatial dispersions for azimuthal and radial index components could not be provided. However, according to [13, 14], difference between index component for wave propagation in two orthogonal directions could be achieved in PhCs with rectangular lattices. Therefore, we explored an opportunity to employ such PhCs in the cloak medium for obtaining desired difference of spatial dispersions of $n_r$ and $n_\theta$.

In [9] it was demonstrated that changing the lattice constant of PhC caused shifting of the 2nd transmission band in its dispersion diagram along the frequency axis. This also caused respective shift of the extracted from the dispersion diagram frequency dependence of index values. It was also proven in [9] that the 2nd branch of array dispersion diagram supplied index values in the range from zero to higher than 1. Therefore, it was possible to determine a set of array lattice constants providing at some frequency a collection of index values representing the spatial dispersion law depicted by curve A in Fig. 1 (b). The requested dispersion law was then realized in the cloak medium by building it from fragments of PhCs with respective lattice constants.

In order to investigate, how the difference in lattice constants along two directions would affect the dependencies of index values on frequency, we first calculated dispersion diagrams for PhCs with rectangular lattices at TM wave incidence along either one of two crystallographic directions, which we denoted as $x$ and $y$. Fig. 4 (a) presents 2$^{nd}$ branches of dispersion diagrams within Γ-X range of wave-vectors for arrays with relative rod permittivity $\varepsilon$ = 35 and $R$ = 1.5 mm (same rod parameters as in [9]), with the same lattice constant $a_x$ and with various lattice constants $a_y$. As seen in the figure, difference between $a_y$ and $a_x$ results in changes of dispersion diagrams, i.e. in anisotropy of array properties. From dispersion diagrams, the values of $x$- and $y$-components of index were calculated by using well-known relation given in [15]:

$$n_{\text{eff}} = \text{sgn}(v_g . k)(\frac{c}{\omega}|k|) \tag{6}$$

where $c$ is the speed of light in free space and $v_g = \frac{d\omega}{dk}$ is the group velocity, while $k$ and ω are wave vector and angular frequency, respectively. Equation 6 characterizes the dominant refractive index. As discussed in [9, 15, 16], this approach provides the effective values of phase refractive indices in the second transmission bands of 2D PhCs. In [9], this approach has been verified by comparing the indices obtained from the dispersion diagrams of 2D rod arrays (at various rod permittivities) with the results of the index retrieval procedure.

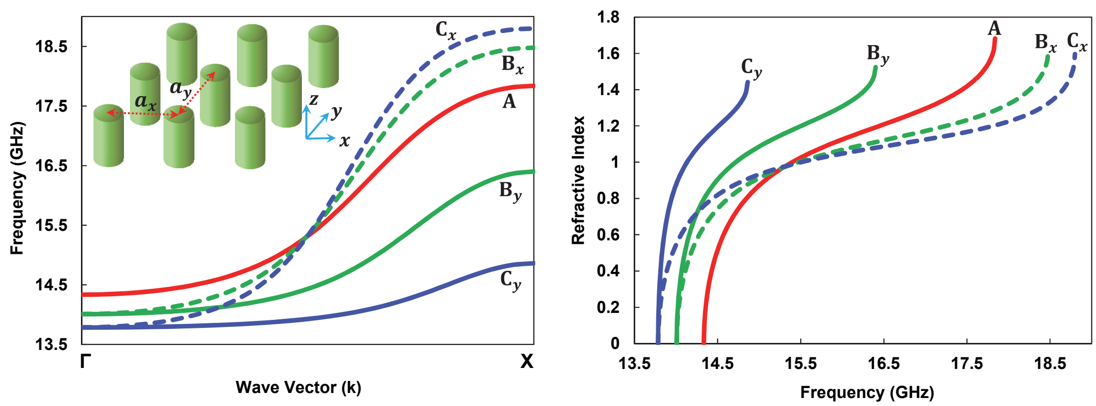


(a) (b)

Figure 4. (a) 2$^{nd}$ branch of dispersion diagrams for rod arrays when incident TM waves are propagating in either $x$ or $y$ directions: $a_x$ is fixed at 5 mm while $a_y$ for curves A, B, and C is 5 mm, 6 mm, and 7 mm, respectively. (b) Dependencies of refractive index components $n_x$ and $n_y$ on frequency calculated using dispersion diagrams in (a).

Fig. 4 (b) presents frequency dependencies of $n_x$ and $n_y$ found by using respective diagrams in Fig. 4 (a). As seen in Fig. 4 (b), at $a_x = a_y$ frequency dependencies of $n_x$ and $n_y$ coincide (curve A). At $a_y > a_x$ dependencies for $n_x$ and $n_y$ shift and split, so that dependencies for $n_y$ get steeper, while dependencies for $n_x$ become less steep and, therefore, cross the curve A. Shifting of the spectra of $n_y$ and $n_x$ reflects lowering of the edge of the 2nd transmission band, which is well seen in Fig. 4 (a). It could be also noticed in Fig. 4 (b) that at increased values of $a_y$, $n_y$ values become significantly exceeding 1 at such frequencies, at which the values of slower growing $n_x$ still remain below 1. Such difference between $n_y$ and $n_x$ in arrays with rectangular lattices seems to point out at an opportunity of realizing desired anisotropy of TO prescriptions for index components in two orthogonal directions.

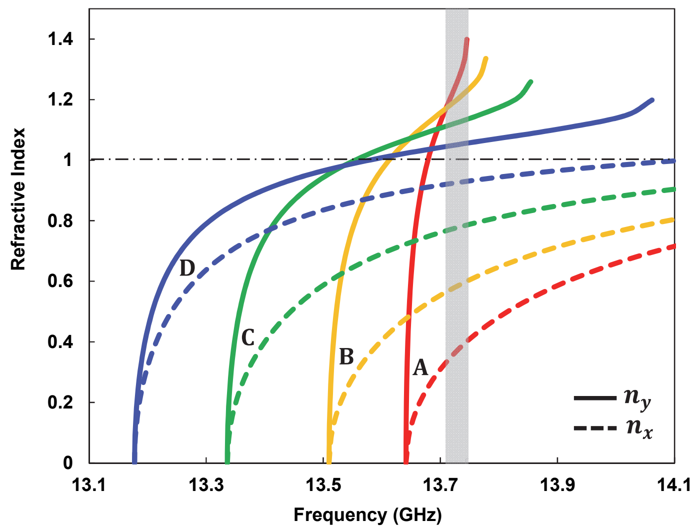


Figure 5. Frequency dependencies of directional index values in the 2nd transmission bands for four arrays with rod parameters: $\varepsilon$ = 35 and $R$ = 1.5 mm, and with rectangular lattices; $a_x$ and $a_y$ values (in mm) for the curve couples A, B, C, and D, are, respectively: (5 ; 7.8), (5.5 ; 8.15), (6.5 ; 8.6), and (8 ; 8.9).

Further investigations, however, have shown that obtaining thus high values of $n_y$, as defined by curve F in Fig. 1 (b), is challenging for PhCs, since having much bigger $a_y$ compared to $a_x$ does not allow for achieving much higher index values than those presented in Fig. 4 (b). Instead, it leads, first, to extinction of the 2nd branch and then, to switching of the sign of $n_y$ from positive to negative, which is not suitable for controlling wave propagation in the cloak. Thus, there are limits for increasing $a_y$ at any chosen $a_x$. For example, at $a_x$ = 5 mm, $a_y$ should not exceed 8 mm to avoid negative index values. At $a_y < 8$ mm and used in [9] rod parameters ($\varepsilon$ = 35 and $R$ = 1.5 mm), $n_y$ values bigger than 1.5 cannot be achieved, while they should be close to 2.4 near the target, according to curve F in Fig. 1 (b) for the cloak with $\frac{R_{\text{out}}}{R_{\text{in}}} = 3.5$. Taking this into account, we looked for a set of arrays with rectangular lattices and with the same, as in [9], rod parameters, which could be used for providing, at some frequency, best fit of index values to dispersion curves A and F in Fig. 1 (b). We considered a set of four arrays, the fragments of which could be used for assembling the cloak, for which prescribed dispersion curves for index components would be represented by step-functions consisting of four steps. Fig. 5 shows extracted from dispersion diagrams frequency dependencies of $n_y$ and $n_x$ values for such four arrays, having different combination of lattice constants $a_x$ and $a_y$. The presented data demonstrate that combining fragments of these arrays in the cloak medium can provide descending spatial dispersion for radial index component and ascending spatial dispersion for azimuthal component at the operation frequency of 13.73 GHz, although the prescribed maximal value of 2.4 for $n_y$ cannot be achieved. This result pushed us to searching for opportunities to decrease maximal $n_r$ values, prescribed by TO, by varying cloak dimensions and to increase $n_y$ values, achievable in rod arrays with rectangular lattices, by modifying rod radius and permittivity.

### 2.1.4 Fitting Capabilities of Rod Arrays to TO Prescriptions for Index Components

From the expressions given in Section 2, it follows that requested index values strongly depend on the ratio $\frac{R_{\text{out}}}{R_{\text{in}}}$. Fig. 6 demonstrates that by increasing this ratio, prescribed radial index values near the target can be essentially reduced, while azimuthal index values are just slightly affected. Thus, as seen in Fig. 6, capabilities of rod arrays would become sufficient for satisfying TO prescriptions at $\frac{R_{\text{out}}}{R_{\text{in}}} > 4.6$. This ratio, however, characterizes, in fact, the thickness of the cloak, so that increasing this ratio means significant increase of the cloak thickness at fixed size of the target. In particular, changing the ratio from 3.5 to 4.6 corresponds to 44% increase of the cloak thickness, which is, obviously, not desirable for practical applications.

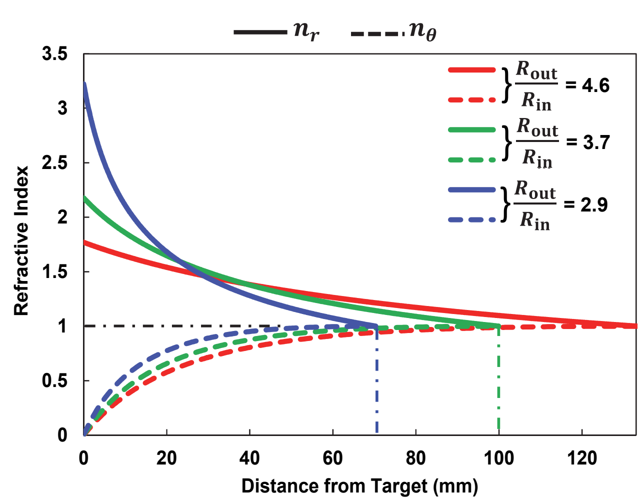


Figure 6. TO-prescribed radial and azimuthal index distributions for three different ratios $\frac{R_{\text{out}}}{R_{\text{in}}}$ of the cloak, when $R_{\text{in}}$ is fixed.

Another approach to satisfying TO prescriptions for the cloak medium formed from rod arrays could be seen in manipulating parameters of rods. As demonstrated in Fig. 7 (a), increasing rod radius from 1.5 mm up to 1.9 mm provided an increase of highest achievable $n_y$ value in PhCs up to 1.8, which corresponded to TO requirements for cloak thickness defined by the ratio $\frac{R_{\mathrm{out}}}{R_{\mathrm{in}}} = 4.6$, although it was still below the requirements for smaller cloak thickness, when $\frac{R_{\mathrm{out}}}{R_{\mathrm{in}}} = 3.5$. The effect of another parameter, i.e. rod permittivity, on achievable index values in rod arrays, is demonstrated in Fig. 7 (b). As seen in the figure, changing rod permittivity did not influence effectively the highest values of $n_y$, however, it allowed for decreasing the asymmetry of array responses along $x$ and $y$ directions and made frequency dependences of both index components $n_y$ and $n_x$ less steep that opened up a window for playing with radii of rods and/or lattice parameters of arrays with the aim of providing higher $n_y$ values. Fig. 7 (c) shows the effect of increasing rod radius in arrays with slightly higher rod permittivity than that used in Fig. 7 (a). From comparing Figs. 7 (a) and (c), it can be seen that an increase of rod permittivity from 35 to 39 allows for approaching $n_y$ value of 2.0, while at permittivity of 35 (as in [9]) it was impossible to reach values of $n_y$ exceeding 1.8. Although performed studies have shown that combined variations of cloak thickness, rod permittivity, and rod radii allow for approaching TO-requested prescriptions for index components in the cloak medium, it would be desirable to search for such reduced prescriptions, which could make practical implementation of PhC-based cloak much more feasible.

### 2.1.5 Reduced Prescriptions for Spatial Dispersion of Index Components in the Cloak Medium

Here we consider an opportunity to replace TO-based prescriptions by reduced spatial dispersion law for radial index component. Our approach is based on understanding of the main function of radial index component in governing wave propagation in the cloak. As it follows from Section 2, the role of radial indices can be described as turning waves around the target. To accomplish this task, TO prescriptions for the radial index component demand very high index values near the target and steep decrease of these values further from the target. In order to restrict TO demands by physically achievable in rod arrays index values, we were looking for reduced dispersion laws for $n_r$, which would still be able to accomplish the function of turning waves around the target. In particular, we looked for dispersion laws with decreased against TO prescriptions $n_r$ values near the target and increased, for compensating this decrease, $n_r$ values in outer cloak layers, as shown by solid red curve in Fig. 8. To choose appropriate analytical expression describing $n_r$ dispersion (solid red curve in Fig. 8), various functions were tested. Basic criteria, employed for the choice, were restoration of the flat wave front behind the cloak and maximal decrease of the total scattering cross-width of the cloaked target versus that of the bare target. Based on these criteria, the expression given below, which is controlled by three parameters, was used as the reduced prescription for $n_r$ dispersion:

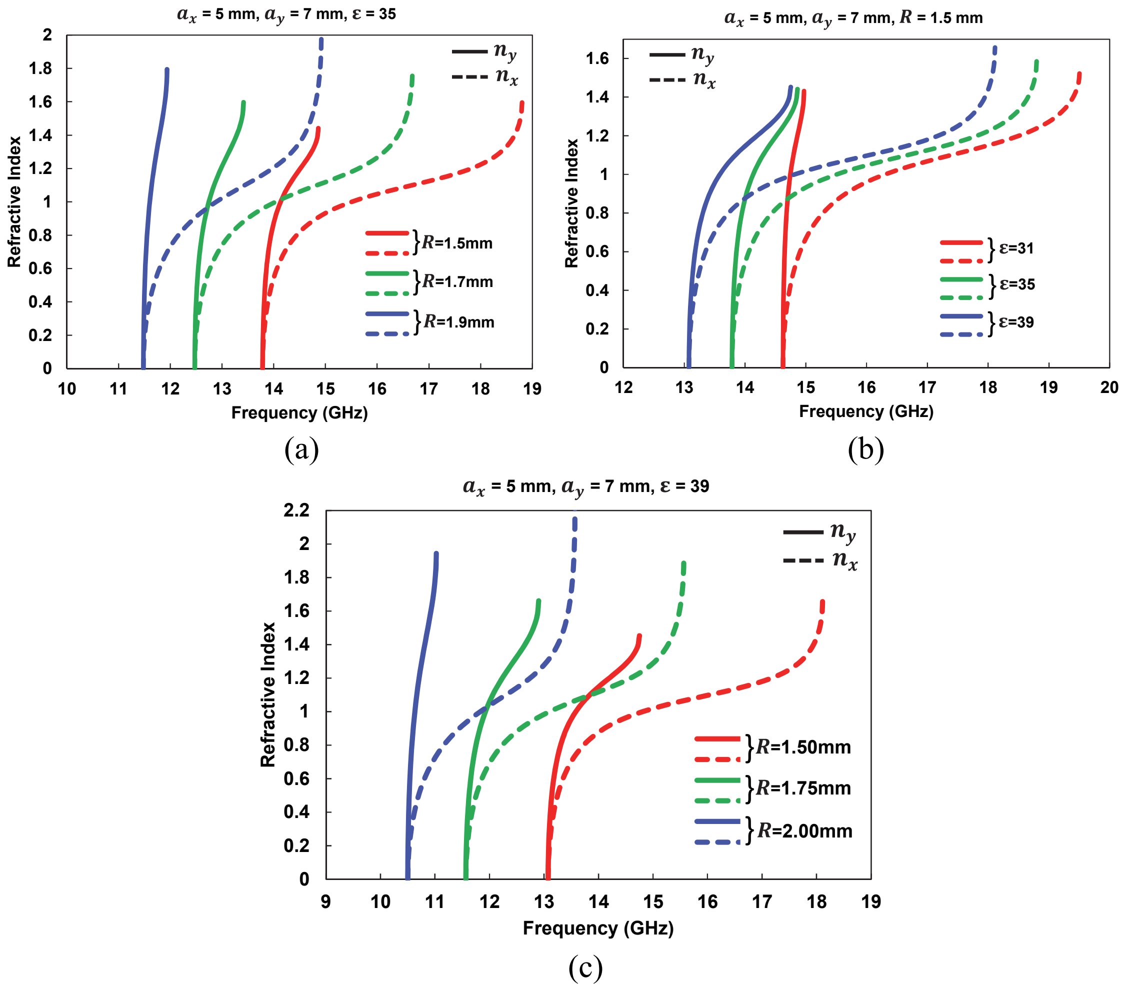


Figure 7. Frequency dependencies of directional index values in 2nd transmission bands of rectangular arrays with $a_x$ = 5 mm and $a_y$ = 7 mm for various values of: (a) rod radius at $\varepsilon$ = 35, (b) rod permittivity at $R$ = 1.5 mm, and (c) rod radius at $\varepsilon$ = 39.

$$n_r = \alpha^{1-\left(\frac{\frac{r}{R_{\text{in}}}-1}{\beta}\right)^{\gamma}} \quad ; \quad R_{\text{in}} \leq r \leq R_{\text{out}} \tag{7}$$

where $\alpha$, $\beta$, and $\gamma$ are, respectively, the parameter controlling the value of $n_r$ at inner boundary of the cloak, the parameter controlling the lowest level of $n_r$ (at outer boundary of the cloak), and the parameter managing the steepness of radial index dispersion. Expression (7) has been obtained at transforming the well-known decaying function $n_r = \alpha^{1-x}$, where $0 < x < 1$ is the distance from some origin. Since, in our case, the distance of interest was defined by the distance between $R_{\text{in}}$ and $R_{\text{out}}$, we, first, replaced $x$ by expression $\frac{r}{R_{\text{in}}} - 1$, which became equal to zero at $R = R_{\text{in}}$ and, thus, provided $n_r = \alpha$ at the inner boundary of the cloak. Then we introduced additional complication in the definition of $x$ as: $x = \frac{\frac{r}{R_{\text{in}}}-1}{\beta}$, which led to $x = 1$ at the outer cloak boundary and, respectively, to $n_r = 1$, if $\beta = \frac{R_{\text{out}}}{R_{\text{in}}} - 1$. Taking the value of $\beta$ bigger than $\frac{R_{\text{out}}}{R_{\text{in}}} - 1$ allowed for requesting the value of $n_r$ at the outer boundary of the cloak to be bigger than 1 up to desired level. Introducing coefficient $\gamma$ in the expression for $n_r$ provided additional option for manipulating the dispersion law at the search for the law providing better fit to the described above criteria.

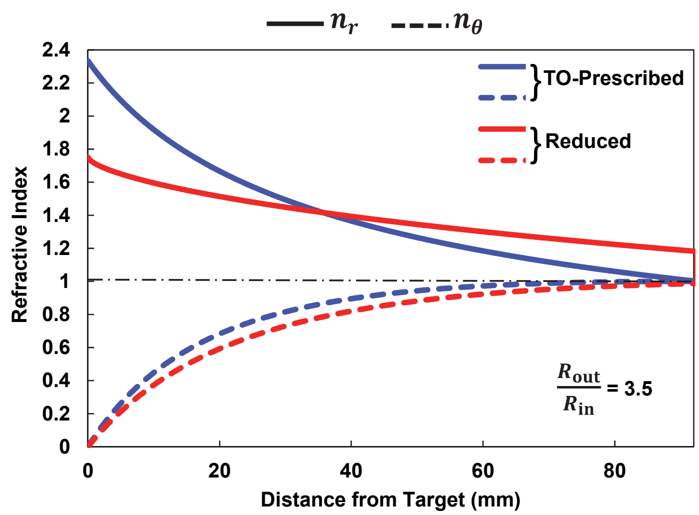


Figure 8. TO-prescribed and reduced (based on Eq. 7 at $\alpha = 1.75$, $\beta = 4.3$, and $\gamma = 0.65$) index dispersions for cloak with $\frac{R_{\text{out}}}{R_{\text{in}}} = 3.5$.

Proposed approach can be illustrated by finding an appropriate reduced prescription for the cloak with $\frac{R_{\text{out}}}{R_{\text{in}}} = 3.5$. First, we determined the values of parameters $\alpha$, $\beta$, and $\gamma$, at which the dispersion law, prescribed by expression (7), would fit TO-prescribed dependence presented by curve F in Fig. 1 (b). Red curve in Fig. 9 (a) illustrates the result of fitting. Then, by reducing the value of $\alpha$, as shown in Fig. 9 (a), the highest value of $n_r$ near the target has been lowered down to less than 1.8, which was attainable in rod array with rectangular lattice, rod radius $R = 1.9$ mm, and $\varepsilon = 35$ (blue curve in Fig. 9 (a)). Then, to increase $n_r$ values in outer layers of the cloak with the aim to compensate for weaker refraction caused by reduced values of $n_r$ near the target, we employed higher than 2.5 values of $\beta$ in expression (7) and have chosen $\beta$ to be equal 4.3 to obtain $n_r \simeq 1.25$ at the outer boundary of the cloak (blue curve in Fig. 9 (b)). Finally, we varied $\gamma$ around the value of 0.7 used at fitting the dispersion law prescribed by expression (7) to TO-prescribed law given by curve F in Fig. 1 (b) (see Fig. 9 (c)).

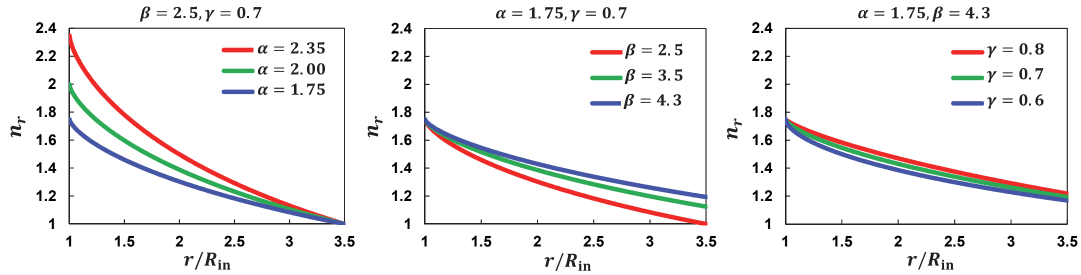


(a) (b) (c)

Figure 9. Calculated radial index dispersions according to expression (7) for various $\alpha$, $\beta$, and $\gamma$ at $\frac{R_{\text{out}}}{R_{\text{in}}} = 3.5$.

Wave propagation through cloaks with media obeying different dispersion laws for $n_r$, was simulated and compared to wave propagation through the cloak with TO-prescribed dispersion (red curve in Fig. 9 (a)). In addition, COMSOL software was used to calculate total scattering cross-widths for the cloaks under study, following [17]. The best performance of the cloak employing reduced prescriptions, which was quite comparable to the performance of the cloak based on TO prescriptions at $\frac{R_{\text{out}}}{R_{\text{in}}} = 3.5$, was demonstrated for the values of parameters $\alpha$, $\beta$, and $\gamma$ equal to 1.75, 4.3 and 0.65, respectively. Fig. 10 demonstrates that the target (metal cylinder) covered by the cloak having reduced index dispersion, causes only slightly higher scattering compared to scattering caused by the target covered with TO-prescribed cloak, both being much lower than scattering caused by bare target.

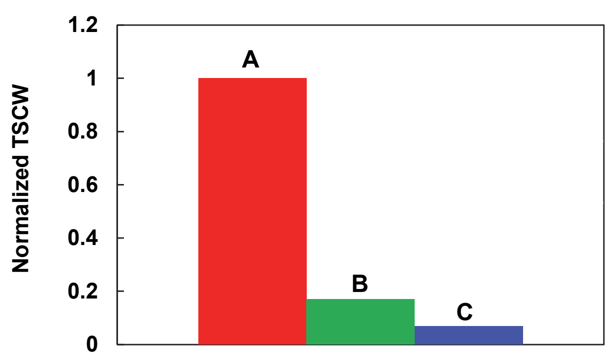


Figure 10. Calculated total scatterings cross-width of bare target (A), of target covered by cloak with reduced index dispersion (B), and of target covered by cloak with TO-prescribed index dispersion (C**).**

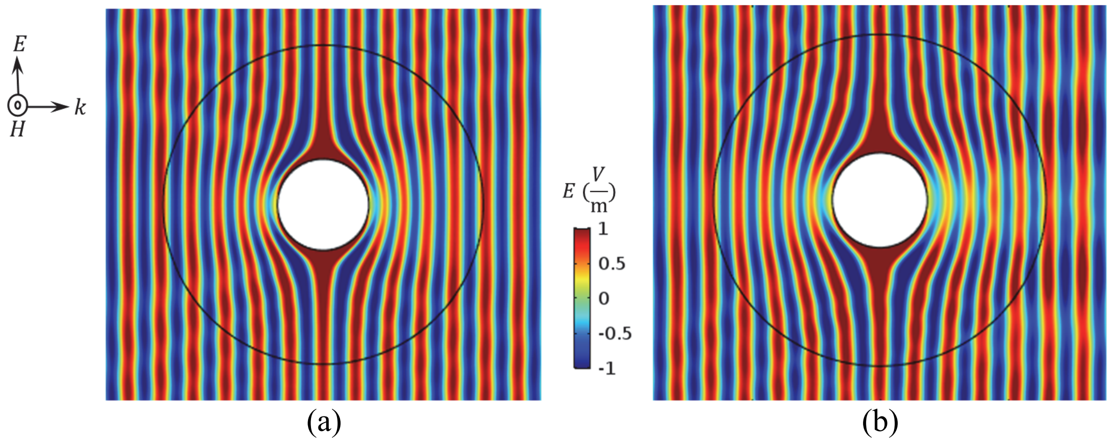


Figure 11. Simulated wave-patterns at an arbitrary frequency of 11.4 GHz, at TM wave incidence from left on cloaked targets with $\frac{R_{\text{out}}}{R_{\text{in}}} = 3.5$: (a) at TO-prescribed index dispersion, (b) at reduced dispersion of radial index component.

As seen in Fig. 11, simulated field patterns for wave propagation through metal cylinders concealed by cloaks with TO-prescribed and reduced index dispersions, look almost identical. It could be concluded, that the main function of TO-prescribed spatial dispersion for radial index component in the cloak medium, which can be described as turning the paths of incident waves around the target with minimal reflection or scattering, could be achieved at reduced prescriptions, if they provide compensation of weaker refraction near the target by enhanced refraction in outer cloak layers. The main advantage of reducing the maximum value of $n_r$ near the target is an opportunity to realize properly performing cloak by using dielectric PhCs with rectangular lattices. It is worth mentioning here that earlier in [3], where the cloak medium was composed of MMs, TO requests to spatial dispersions of material parameters have also been reduced. Original $\varepsilon_Z$ and $\mu_\theta$ distributions in [3] were approximated by constant values, and $\mu_r$ was the only radially varied parameter that made the realization of the cloak essentially easier. However, this cloak did not provide appropriate wave-front reconstruction beyond the target and demonstrated a non-negligible shadow, characteristic for improper realization of refraction demands. Similar, as in [3], approach was used at building the cloak from dielectric-metal MMs in [18], where $\mu_z$ and $\varepsilon_\theta$ were reduced to constant values, while $\varepsilon_r$ was changing from 0 at inner boundary of the cloak to 1 at outer boundary. Similar to [3], power flow beyond the cloak with reduced material parameters was found to be essentially lower than that in the case of the cloak with full parameters prescribed by TO.

We have shown that for obtaining proper cloaking effect, cloak medium, formed from PhCs, should have its radial index component changing from values exceeding 1 near the target down to 1 at the outer boundary of the cloak, in addition to ascending dispersion for azimuthal index component, unless waves are guided around the target due to self-collimation phenomenon mimicking refraction effects. It is demonstrated that two types of spatial dispersions prescribed for index components of cylindrical cloaks can be realized in the media built from 2D PhCs with rectangular lattices of dielectric rods. Such crystals were shown capable of supporting, in the $2^{nd}$ transmission bands, index values ranging from zero to those significantly exceeding 1. Increasing PhC's lattice constants allowed for shifting their $2^{nd}$ bands in dispersion diagrams down to lower frequencies thus providing spatial dispersion of indices in the cloak composed of PhCs fragments with different lattice constants. However, maximal values of radial indices, which could be obtained in PhCs at increasing lattice asymmetry, appeared to be less than those prescribed by TO because of restrictions imposed on crystal asymmetry by extinction of the $2^{nd}$ transmission band. Changes of the cloak thickness and rod parameters were found incapable of completely closing the gap between TO prescriptions and modalities of used PhCs. To solve this problem, we proposed reduced prescriptions for radial index dispersion. Reduced dispersion law suggested employing essentially smaller values of radial index near the target, than those requested by TO, so that these values would be achievable by using crystal asymmetry. To compensate for weaker refraction in inner layers, we proposed to provide higher than requested by TO index values in outer layers of the cloak. Conducted simulations of the cloaks with reduced spatial dispersions of radial indices have shown that these cloaks perform similarly to TO-following cloaks, i.e. support wave front restoration beyond the target and drastic decrease of the total scattering cross-width by the cloak. These results make feasible practical realization of invisibility cloak by using PhCs with rectangular lattices.

## 2.2 Employing GRIN PC- inspired Approach for Building Invisibility Cloak Media from Photonic Crystals[2]

### 2.2.1 Introduction

Dielectric photonic crystals (PCs) provide a low-loss platform for designing various photonic devices. One of perspective applications for PCs is their employment in transformation media, in particular, in invisibility cloaks [8]. It is known that Transformation Optics (TO) requests materials with properties, which cannot be found in nature. In our recent work [9] it was demonstrated that in cylindrical cloaks formed from 2D PCs with square lattices, waves could move with superluminal phase velocities. Later in [19] we have shown that at employment of PC with rectangular lattices, anisotropic dispersions of refractive index components could be achieved in the cloak media, in addition to superluminal wave propagation.

In this work, in order to decrease scattering from cloaked objects, we investigate an opportunity of using an approach, inspired by GRIN PCs [20, 21], to form the cloak medium with prescribed index dispersions. As known, GRIN PCs are formed by

[2]Reprinted from 'S. Jamilan and E. Semouchkina, "Employing GRIN PC-inspired Approach for Building Invisibility Cloak Media from Photonic Crystals," IEEE Photonics Conference, VA, USA, 2018'; with permission from © IEEE Publishing.

appropriate gradual changes of PC lattice constants in one direction. For the cloak medium, we had to solve a more complicated task of providing gradual modification of PC parameters in two directions to control radial dispersions of azimuthal and radial index components. Obtained results demonstrate that employed approach allows for substantial decreasing the thickness of the cloak without deteriorating expected according to TO predictions wave front reconstruction beyond cloaked target. Decreased thickness of the cloak leads to essentially less scattering from cloaked object compared to scattering from bare target thus providing more efficient cloaking effect. Full-wave simulations in this work have been performed by using COMSOL Multiphysics software, while MPB package was employed for calculating dispersion diagrams of PCs.

### 2.2.2 TO Prescriptions for Cloak Medium Built from Anisotropic PhCs

To provide proper performance of cylindrical invisibility cloak, TO requires specific radial dispersions for azimuthal index component $n_\theta$ and for radial index component $n_r$. The value of $n_\theta$ has to grow up from zero at inner boundary of the cloak towards 1 at outer boundary of the cloak, while the value of $n_r$ has to descend from bigger than 1 values at inner boundary of the cloak to 1 at the outer cloak's boundary [9]. PCs with rectangular lattices were found capable of providing anisotropy of refractive indices along two normal to each other crystallographic axes of crystals [19]. However, modifications of rectangular unit cells did not allow for ensuring such high degree of index anisotropy, which was prescribed by TO for cloak layers located close to inner boundary of the medium. As described in [19], the possibility to overcome this discrepancy was found in replacing TO-prescribed dispersion law for $n_r$ by reduced dependence incorporating achievable in PC values of $n_r$ near the cloaked object and higher than TO-prescribed values of $n_r$ in outer layers of the cloak. Careful balancing of these changes has allowed for observing the TO-predicted cloaking effect in cloak models with reduced index dispersion that justified an employment of proposed reduction. Fig. 12 presents TO-prescribed dispersion for $n_\theta$ and the reduced dispersion for $n_r$. The figure also shows an approximation of the dispersion curves by step-functions made of six gradual steps. These steps were used to determine the values of index components for circular arrays, which represented fragments of PCs necessary to form the cloak.

Fig. 13 demonstrates frequency dependencies of index components calculated for two orthogonal directions *X* and *Y* in six infinite PCs composed of dielectric rods with different sets of lattice constants $a_x$ and $a_y$. Presented dependencies have been obtained from the 2nd transmission branches in dispersion diagrams of respective PCs [9]. It is well seen in the figure that at the frequency of 11.2 GHz chosen as operating frequency, indices controlling wave propagation along *X*-axis are spread in the range from 0.3 up to 1 and, so, are capable of supporting "superluminal" phase velocity of waves, while indices controlling *Y*-direction are in the range between 1.25 and 1.8, and so, can provide reduced dispersion of $n_r$. Therefore, using properly rolled-up concentric fragments of PCs from series A-F in

Fig. 13 provided an opportunity to build the cloak medium with dispersions presented by step-functions in Fig. 12.

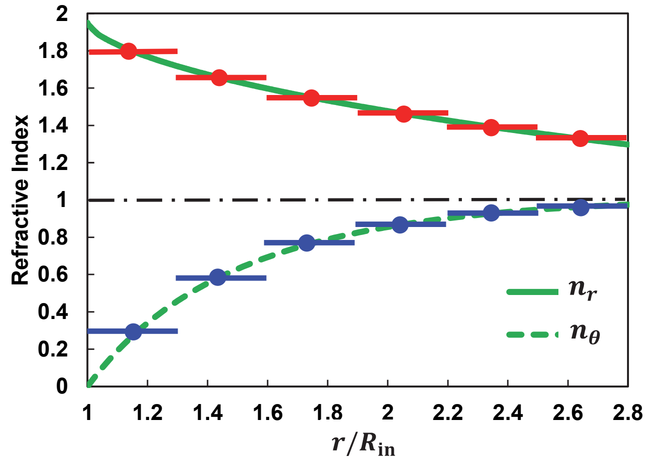


Fig. 12. Green curves-dispersions of index components chosen for building a cloak with $R_{\text{out}}/R_{\text{in}}$= 2.8; red and blue steps–parts of step-functions used for approximating chosen dispersions

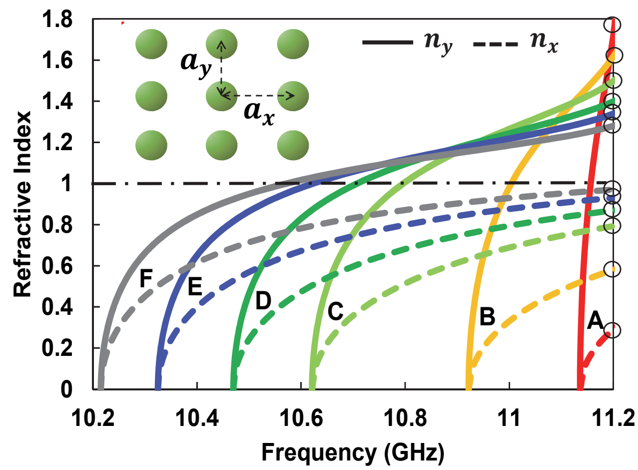


Fig. 13. Frequency dependencies of directional index components (in the 2nd transmission band at TM wave incidence) for composed of dielectric rods (ε = 35, $R$ = 2 mm) PCs with lattice constants $a_x$ and $a_y$ (in mm): A (4.95 × 6.85), B (5.2 × 7.37), C (5.75 × 8.26), D (6.2 × 8.77), E (6.8 × 9.32), and F (7.45 × 9.75).

### 2.2.3 Verifying GRIN PC- Inspired Approach to Designing PhC-based Cloak Medium

To verify the applicability of the GRIN PC- inspired approach, we represented fragments of PCs from series A-F (Fig. 13) in the cloak medium by single circular arrays. Thus we have built the cloak medium from six circular arrays. From captions to Fig. 13 it is seen that transition from one circular array to another is accompanied by gradual changes of two lattice constants (in azimuthal and radial directions). Although such changes should cause some distortions of the shapes of unit cells, we expected that these distortions would not significantly affect the index values found for respective lattice constants. Field patterns simulated at TM wave incidence on clocked object and on bare object are presented in Figs. 14a and 14b, respectively. From comparison of two figures it could be concluded that GRIN PC-inspired approach to designing the cloak medium provided an opportunity to realize predicted by TO wave front changes at wave movement around hidden object and wave front reconstruction beyond the object. Calculations of the total scattering cross-width (TSCW) for two cases have shown that TSCW of cloaked object appears to be 40% less that the TSCW of the bare object.

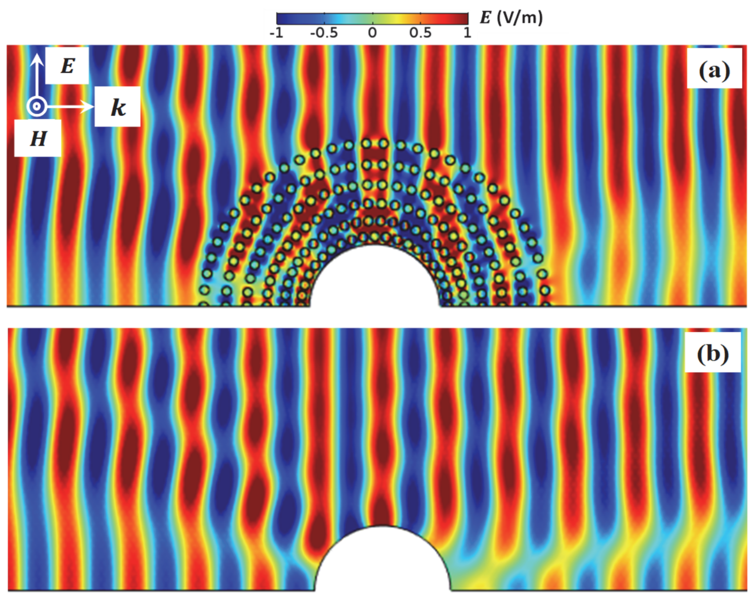


Fig. 14. Snap-shots of TM wave incidence on (a) metallic object covered by PC-based cloak and (b) bare object at frequency of 11.49 GHz.

Obtained results confirm an opportunity to use the GRIN PC-inspired approach to designing the cloak medium from fragments of PCs with rectangular lattices. This allows for realizing close to TO-prescribed spatial dispersions of radial and azimuthal index components, which control bending the wave paths around the cloaked object and speeding up waves along curvilinear paths. The proposed approach to designing cylindrical cloaks can be scaled to higher frequencies, including optical range, by scaling dimensions of dielectric rods.

# References


1. J. B. Pendry, D. Schurig, and D. R. Smith, 'Controlling Electromagnetic Fields,' Science, Vol 312, 23, June 2006.

2. Y. Nathan, B. Kundtz, D. R. Smith, and J. B. Pendry, 'Electromagnetic Design with Transformation Optics,' Proceedings of the IEEE, Vol. 99, No. 10, October 2011.

3. S. A. Cummer, B.-I. Popa, D. Schurig, D. R. Smith, and J. Pendry, 'Full-Wave Simulations of Electromagnetic Cloaking Structures,' Physical Review E, 74, 036621, 2006.

4. D. Schurig, J. J. Mock, B. J. Justice, S. A. Cummer, J. B. Pendry, A. F. Starr, and D. R. Smith, 'Metamaterial Electromagnetic Cloak at Microwave Frequencies' Science, Vol 314, 10, Nov. 2006.

5. W. Cai, U. K. Chettiar, A. V. Kildishev, and V. M. Shalaev, 'Optical Cloaking with Metamaterials,' Nature Photonics, Vol 1, April 2007.

6. D. P. Gaillot, C. Croënne, F. Zhang, and D. Lippens 'Transformation Optics for the Full Dielectric Electromagnetic Cloak and Metal–Dielectric Planar Hyperlens,' New Journal of Physics, Vol. 10, 115039, Nov. 2008.

7. E**.** Semouchkina, D. H. Werner, G. B. Semouchkin, and C. Pantano, 'An Infrared Invisibility Cloak Composed of Glass,' Applied Physics Letters*,* 96, 233503, 2010.

8. Y. A. Urzhumov and D. R. Smith, 'Transformation Optics with Photonic Band Gap Media' Physical Review Letters*,* 105, 163901, 2010.

9. E. Semouchkina, R. Duan, N. P. Gandji, S. Jamilan, G. Semouchkin, and R. Pandey, 'Superluminal Media Formed by Photonic Crystals for Transformation Optics-Based Invisibility Cloaks,' Journal of Optics, 18, 044007, 2016.

10. S. G. Johnson and J. D. Joannopoulos, 'Block-iterative frequency-domain methods for Maxwell's equations in a planewave basis,' Optics Express, 8, no. 3, 173-190, 2001.

11. W. Cai, U. K. Chettiar, A. V. Kildishev, V. M. Shalaev, and G. W. Milton, 'Nonmagnetic Cloak with Minimized Scattering,' Applied Physics Letters, 91, 111105, 2007.

12. R. C. Rumpf, J. Pazos, C. R. Garcia, L. Ochoa, and R. Wicker, '3D Printed Lattices with Spatially Variant Self-Collimation,' Progress In Electromagnetics Research, Vol. 139, 2013.

13. Y. Takayama and W. Klaus, ‘Refractive Behavior of 2D Square Lattice Photonic Crystals Determined by Reducing the Symmetry of the Unit Cell,’ Japanese Journal of Applied Physics, Vol. 41, No. 11A, pp. 6375–6379, Nov. 2002.

14. L. Peng, L. Ran, and N. A. Mortensen, ‘Achieving Anisotropy in Metamaterials Made of Dielectric Cylindrical Rods,’ Applied Physics Letters, 96, 241108, 2010.

15. P.V. Parimi, W.T. Lu, P. Vodo, J. Sokoloff, J. S. Derov, and S. Sridhar, ‘Negative Refraction and Left-Handed Electromagnetism in Microwave Photonic Crystals,’ Physical Review Letters, Vol 92, No 12, p. 127401, March 2004.

16. M. Notomi, ‘Theory of Light Propagation in Strongly Modulated Photonic Crystals: Refractionlike Behavior in the Vicinity of the Photonic Band Gap,’ Physical Review B, Vol. 62, No. 16, Oct. 2000.

17. https://www.comsol.com/model/radar-cross-section-8613.

18. D. Diedrich, A. Rottler, D. Heitmann, and S. Mendach, ‘Metal–Dielectric Metamaterials for Transformation-Optics and Gradient-Index Devices in the Visible Regime,’ New Journal of Physics, 14, 053042, 2012.

19. S. Jamilan, G. Semouchkin, N. P. Gandji, and E. Semouchkina, “Spatial dispersion of index components required for building invisibility cloak medium from photonic crystals”, Journal of Optics, 20, 045102, 2018.

20. B. Vasic and R. Gajic, “Self-focusing media using graded photonic crystals: focusing, fourier transforming and imaging, directive emission, and directional Cloaking,” Journal of Applied Physics, 110, 053103, 2011.

21. Q. Zhu, L. Jin, and Y. Fu, “Graded index photonic crystals: a review”, Annalen der Pysik, (Berlin) 527, No. 3–4, 205–218, 2015.

22. S. Jamilan, G. Semouchkin, N. P. Gandji, and E. Semouchkina, “Spatial dispersion of index components required for building invisibility cloak medium from photonic crystals,” Journal of Optics, Vol. 20, No. 4, 045102, 2018.

23. S. Jamilan and E. Semouchkina, “Employing GRIN PC-inspired approach for building invisibility cloak media from photonic crystals,” IEEE Photonics Conference, VA, USA, 2018.

# 3 Using Self-collimated Wave-guiding in Invisibility Cloaks[3]

## 3.1 Introduction

An ideal cylindrical invisibility cloak should guide incident waves around a hidden object without scattering and reflection. Transformation Optics (TO) prescribes the values of material parameter in the cloak medium suitable for such guiding [1]. However, realizing TO prescriptions is very challenging, since they request close to zero values of azimuthal index components and values of radial index components, far exceeding 1. Such values are necessary for providing superluminal phase velocities of waves along elongated paths around the target, on one hand, and for proper turning wave trajectories to support circular wave movement, on the other hand. While metamaterials have been conventionally considered as the best candidates for the cloak media, we have earlier shown that there are advantages of forming the transformation media from fragments of photonic crystals (PhCs) [2, 3]. However, it was also found that at building up the cloak of desired thickness from arrays of dielectric rods with rectangular lattices, it was not possible to realize in full all TO-prescribed values for radial components of refractive indices in the cloak medium. At the same time, it was revealed that in the cloaks, composed of concentric circular rod arrays, waves could be sent around the target using the phenomenon of self-collimation (SC) [3]. Realizing such SC effects requires turning crystallographic axes of PhC fragments that could be accomplished by gradually altering the orientation of unit cells [4]. In this work, we investigate the possibility to employ self-collimated wave-guiding, instead of using prescribed by TO high values of radial index components, at designing the cloak. The cloak was composed of rods with relative permittivity of 37.2 and radii of 3 mm for performing future experiments in microwave range. The design of the cloak can be re-scaled for optical range at using silicon nano-rods.

## 3.2 Underlying Concept, Design, and Performance of the Cloak

Figure 1 illustrates the concept of the cloak design. The wave paths controlled by SC are shown by two big arcs in the central areas of the cloak. These cloak parts were built up of rod array composed of identical unit cells with the same lattice parameters along azimuthal and radial directions. These lattice parameters had to provide the values of refractive index components equal to 1, i.e., corresponding to free space, at the cloak operation frequency. While lattice parameters were not varied on the wave paths within SC parts of the cloak, turning of wave paths was provided by SC. Orientation of unit cells, constituting SC regions, was changing from cell to cell, so that azimuthally directed sides of cells followed

[3]Reprinted from ‘S. Jamilan and E. Semouchkina, “Using Self-collimated Wave-guiding in Invisibility Cloaks,” SPIE Conference, Metamaterials XIII, 11769, 117690K, 2021’; with permission from © SPIE Publishing.

circular paths, while their radially directed sides were normal to them. Such reorientation of cells mimics bending of crystallographic axes in PhC. In the SC parts of the developed cloak design, we used four parallel rows of unit cells, bent along circular paths. Identical lattice parameters of four arrays excluded impedance mismatch at the wave movement along arcs within SC regions. Two additional transition regions at the cloak input and output (see Figure 1) were designed using TO approaches. These regions had to transform, first, wave movement along straight path at the cloak input into circular movement within SC controlled areas and then, from circular movement into straight movement at the cloak output. Figure 2 presents the results of modelling wave propagation throughout the output region at the right end of SC controlled circular arc in the upper half of the cloak. At solving the transformation problem, we employed TO-based approaches used in [5].

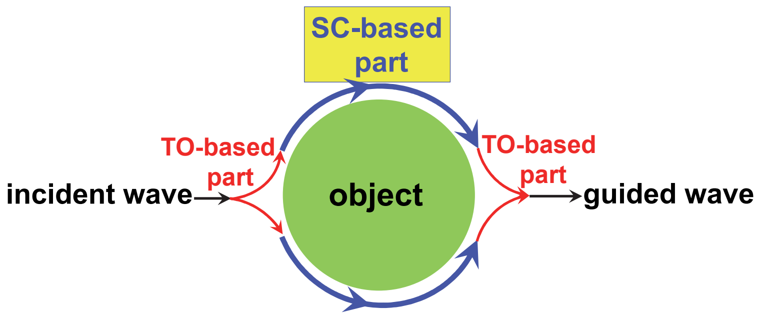


Figure 1. Cross-section of the schematic of wave flow through unidirectional cylindrical invisibility cloak, hiding cylindrical object. The cloak is employing self-collimated wave movement along circular paths between input and output.

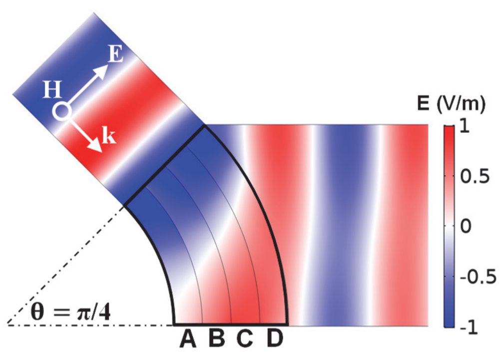


| layer | $n_\theta$ | $n_r$ |
|---|---|---|
| A | 0.3 | 0.6 |
| B | 0.4 | 0.6 |
| C | 0.5 | 0.6 |
| D | 0.6 | 0.6 |

Figure 2. Schematic of wave pattern provided by TO-based transition section of the cloak medium at the end of upper arc-type self-collimated path. Transformation medium operates with waves passing along four arc-type layers (A, B, C, and D) and starts to modify the wave movement at the dashed-dotted line marking the upper edge of θ angle. Presented field-pattern is based on the solution obtained by using COMSOL Multiphysics software.

Chosen coordinate transformation was aimed at redirecting waves, propagating along four arc-type circular paths, into output straight paths. Redirection was equivalent to turning the wavefront counterclockwise by π/4 radian. This turning was provided due to radial dispersion of azimuthal index component in the medium of TO-based cloak section at fixed values of radial index components, controlling the four arc-type paths (as seen in the Table in Figure 2). TO-prescribed azimuthal index component had the lowest value for the path A and the highest value for the path D that caused increased phase velocity of wave moving near the lower edge of the transformation medium and much slower wave propagation along the path D. As seen in Figure 2, defined by the Table dispersion of azimuthal index component allowed for realizing the desired counterclockwise turning of wavefront within the transformation medium. On the left side of the cloak, we had to form the transformation medium, inverted relatively one presented above, to allow wave moving along straight path enter the region with four arc-type wave paths (from D to A). Thus, in the left transition section, the transformation medium had to provide turning of wavefront by 45 degrees to make it parallel to dashed-dotted line marking the upper edge of θ angle. The resulting wave flow, normal to this line, had to initiate SC-controlled wave flow in the upper part of the cloak.

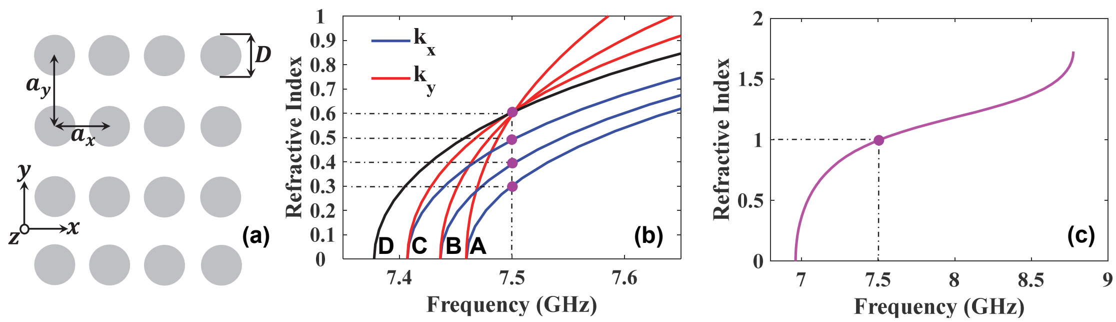


Figure 3. (a) Schematic of 2D rod array with rectangular lattice in $xy$ cross-section (diameter and relative permittivity of rods: D = 6 mm and ε = 37.2). (b) Frequency dependencies of orthogonal refractive index components for four rod arrays within their 2$^{nd}$ transmission bands under TM wave incidence, used in TO-based transition regions. Lattice constants ($a_x$ and $a_y$) in four layers of transition regions are, respectively (in mm): A (7.32, 8.74), B (7.55, 8.62), C (7.84, 8.48), and D (8.24, 8.24). (c) Frequency dependence of refractive index (2$^{nd}$ band for TM wave) in rod array with square lattice: $a_x = a_y = 9.9$ mm used in SC-based region. MPB (MIT Photonic Bands) software was used for calculating the dispersion data of rod arrays [7].

Figure 3 (b) shows frequency dependencies of index components for rod arrays representing four layers (A, B, C, and D in Figure 2) of TO-based cloak parts. These layers should respond identically in radial direction at the operating frequency of 7.5 GHz providing $n_r = 0.6$, while their indices in azimuthal direction should experience changes on the wave paths. At building the layers of arc-type transformation media, we oriented unit cells with their short sides along $x$ direction and elongated sides along $y$ direction that corresponded to azimuthal and radial directions, respectively, in the cloak medium. Thus, the curves in Figure 3 (b) were calculated for two orthogonal directions $x$ and $y$, within the 2$^{nd}$ transmission bands of arrays. It is worth noting here that building TO-based parts of the cloak from rod arrays was performed at relying on the concept of graded index (GRIN) PhCs [6]. Respective fragments of four PhCs (A, B, C, and D) included single circular arrays.

Two arc-type wave paths in the central SC-based part of the cloak were formed by the rows of unit cells properly oriented to mimic bent arrays with square lattices. The responses of these arrays are represented by the frequency dependence of their index presented in Figure 3 (c). It is seen in the figure that arrays with square lattices provided at the operation frequency of 7.5 GHz the value of index equal to 1, i.e., the value characteristic for free space. In addition, to avoid index mismatch at the boundaries of SC-based parts and TO-based regions, we properly adjusted the refractive index values in neighboring unit cells. We used matching arrays (A′, B′, C′, and D′) between SC-parts and TO-sections (A, B, C, and D). Matching arrays had to provide median indices, given in the table in Figure 4, with respect to the index of SC-parts ($n$ =1) and indices of TO-part layers. Frequency dependencies of index components within 2nd transmission bands of four rod arrays with rectangular lattices A′, B′, C′, and D′ are plotted in Figure 4. Considering the operation frequency of 7.5 GHz, lattice parameters of these PhCs were properly chosen for realizing the desired matching arrays.

| layer | $n_\theta$ | $n_r$ |
|---|---|---|
| A′ | 0.65 | 0.8 |
| B′ | 0.7 | 0.8 |
| C′ | 0.75 | 0.8 |
| D′ | 0.8 | 0.8 |

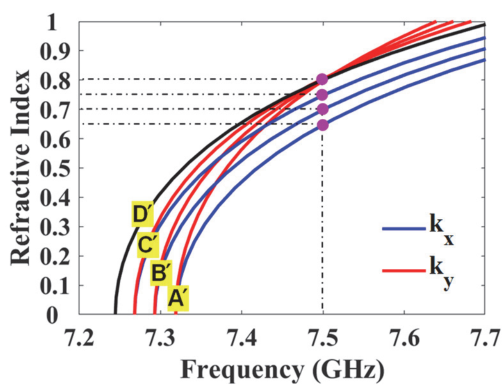


Figure 4. Frequency dependencies of orthogonal index components (2nd band for TM wave) in rod arrays for matching layers. Lattice constants ($a_x$ and $a_y$) are, respectively (in mm): A (8.03, 8.81), B (8.22, 8.78), C (8.42, 8.74), and D (8.66, 8.66).

Complete cloak medium was formed using SC-parts, TO-based regions, and matching layers composed from identical dielectric rods. The diameter of cylindrical metal object was 100 mm, and a TM polarized plane wave was used for excitation. Figure 5 allows for comparing wave patterns, observed at wave scattering by the bare metal cylinder and by the cloaked cylinder. It is seen in the figure that at the operation frequency, the designed cloak demonstrates a very good restoration of the flat wavefront beyond the object. In Figure 6, calculated total scatterings cross-width (TSCW) curves show that the cloak is reducing scattering by 40%.

SC-based cloak has a relatively small thickness, so that $R_{out} / R_{in} = 1.79$, where $R_{out}$ and $R_{in}$ are, respectively, inner and outer radii of the cylindrical cloak medium. For a cloak that was designed fully using TO-prescribed material parameters by employing rectangular-lattice arrays of similar dielectric rods, this ratio was $R_{out} / R_{in} = 3$ [8]. In addition, newly designed SC-based cloak is operating under plane-wave illumination, while SC-based devices typically work with electromagnetic beams [9]. With described above characteristics, SC-based cylindrical cloak composed of dielectric rod arrays is a promising candidate for practical applications in microwave and optical ranges.

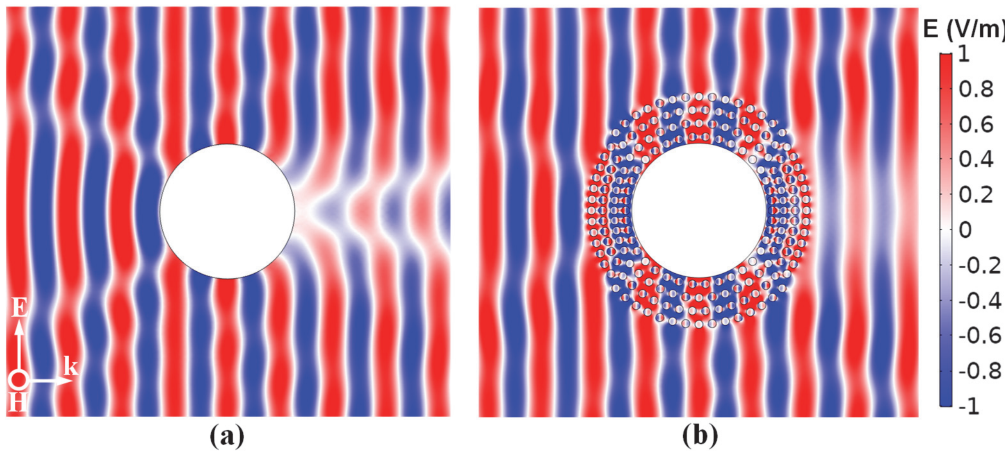


Figure 5. Simulated using COMSOL Multiphysics software wave patterns for wave passing (a) bare metal cylinder and (b) cloaked cylinder at the operation frequency (7.66 GHz).

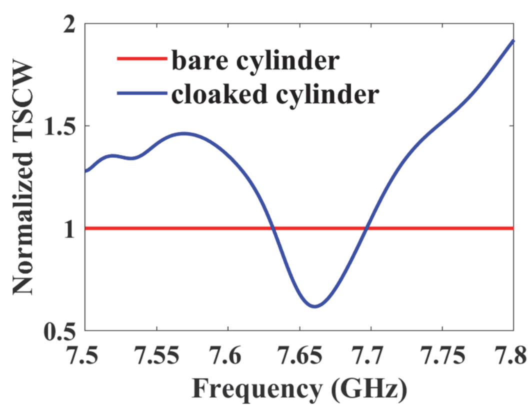


Figure 6. Total scatterings cross-widths (TSCWs) calculated for bare metal cylinder and for metal cylinder cloaked with SC-based cloak.

## References


1. Kundtz, N. B., Smith, D. R., and Pendry, J. B., "Electromagnetic design with transformation optics," Proceedings of the IEEE 99(10), 1622-1633 (2011).

2. Semouchkina, E., Duan, R., Gandji, N. P., Jamilan, S., Semouchkin, G., and Pandey, R., "Superluminal media formed by photonic crystals for transformation optics-based invisibility cloaks," Journal of Optics 18, 044007 (2016).

3. Jamilan, S., Semouchkin, G., Gandji, N. P., and Semouchkina, E., "Spatial dispersion of index components required for building invisibility cloak medium from photonic crystals," Journal of Optics 20, 045102 (2018).

4. Rumpf, R. C., Pazos, J., Garcia, C. R., Ochoa, L., and Wicker, R., "3D printed lattices with spatially variant self-collimation," Progress In Electromagnetics Research 139, 1-14 (2013).

5. Jiang, W. X., Cui, T. J., Zhou, X. Y., Yang, X. M., and Cheng, Q., "Arbitrary bending of electromagnetic waves using realizable inhomogeneous and anisotropic materials," Physical Review E 78, 066607 (2008).

6. Zhu, Q., Jin, L., and Fu, Y., "Graded index photonic crystals: a review," Annalen der Physik (Berlin) 527, 205-218 (2015).

7. Johnson, S. G., and Joannopoulos, J. D., "Block-iterative frequency-domain methods for Maxwell's equations in a planewave basis," Optics Express 8(3), 173-190 (2001).

8. Jamilan, S., Semouchkin, G., and Semouchkina, E., "Implementing photonic crystals, instead of metamaterials, in the media of transformation optics-based devices," 2018 IEEE Research and Applications of Photonics In Defense Conference (RAPID), Miramar Beach, FL, USA, 1-4 (2018).

9. Noori, M., Soroosh, M., Baghban, H., "Self-collimation in photonic crystals: applications and opportunities," Annalen der Physik 530, 1700049 (2018).

10. Jamilan, S., and Semouchkina, E., "Using self-collimated wave-guiding in invisibility cloaks," SPIE Conference, Metamaterials XIII, 11769, 117690K (2021).

# 4 Collimation Effect in Strongly Modulated Anisotropic Photonic Crystals with Near-Zero Refractive Indices[4]

## 4.1 Introduction

Development of the media with near-zero refractive indices (NZRIs) has opened new opportunities for controlling electromagnetic wave propagation [1]. Such media could be employed for realizing various unusual effects including cloaking. Especially, effective control of wave processes is expected at anisotropy of NZRI media [2, 3]. Since natural materials could not possess with NZRI, creating such media requires employing metamaterials or photonic crystals (PhCs). In particular, all-dielectric media of such types were considered as the best choice, since they allowed for overcoming the loss problems. Following [4], we have operated in this work with 2D dielectric rod arrays, which demonstrated PhC-type responses. The MPB and COMSOL software packages were used to simulate the dispersion data, S21 transmission spectra, and wave-patterns. Rods had the permittivity of 37.2 and diameter of 6 mm and were considered to be infinitely long along z-axis. We fixed directional lattice constant $a_x$ at 8 mm and changed $a_y$ from 8 mm to 14 mm.

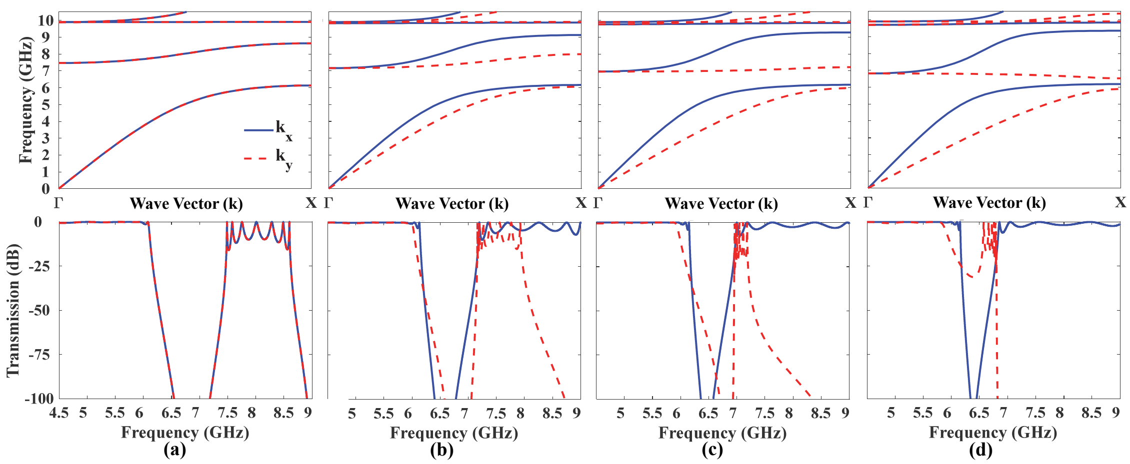


Fig. 1. Dispersion diagrams and transmission spectra for PhCs with unit cell width $a_x$ = 8 mm and the lengths: (a) $a_y$ = 8, (b) 10, (c) 12, and (d) 14 mm, when TM wave propagates in either $x$ or $y$ directions.

## 4.2 Unidirectional Transmission in Rod Arrays

The idea underlying the design of anisotropic NZRI media was based on the properties of dielectric rod arrays with rectangular lattices. We have found previously that such arrays

[4]Reprinted from 'S. Jamilan and E. Semouchkina, "Collimation Effect in Strongly Modulated Anisotropic Photonic Crystals with Near-Zero Refractive Indices," CLEO: QELS_Fundamental Science, 2021'; with permission from © The Optical Society (OSA) Publishing.

could demonstrate significant differences in wave propagation along two orthogonal directions, defined by long and short sides of unit cells [5]. In this work, we detected that extending the lengths of unit cells at fixed width caused shifting of the dispersion diagrams, characterizing wave propagation in long side direction, to lower frequencies. At proper cell lengths, the 2nd stop-band for waves moving in this direction became observed at the frequencies, corresponding to the 2nd transmission-band in the orthogonal direction, thus introducing strong anisotropy in the array properties. Figure 1 shows the changes of array dispersion diagrams at transforming the original square lattices in rectangular ones and then increasing the cell lengths at keeping their widths fixed. As seen in the figure, the second branch of dispersion diagrams for the direction defined by the long sides of unit cells gradually becomes less steep, compared to its original shape and even acquires a negative slope at the cell length equal to 14 mm. As the result, transmission spectra (S21) of arrays shift along the frequency axis, so that the 2nd transmission band for the long side direction appears located at the frequencies, corresponding to the bandgap for wave propagation along the short sides of unit cells (see Figure 1 (d)). It means that the described lattice transformation makes the array demonstrating unidirectional transmission.

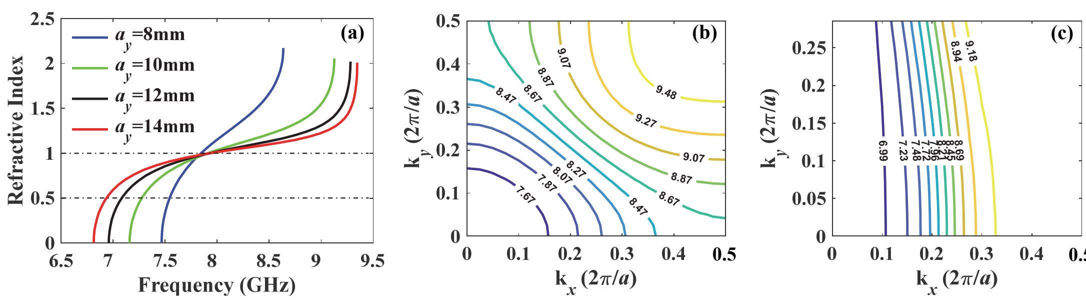


Fig. 2. (a) Frequency dependencies of refractive indices within 2nd transmission band for TM waves, propagating along $x$-axis in PhCs with unit cell width $a_x$ = 8 mm and the lengths: $a_y$ = 8, 10, 12, and 14 mm. EFCs of $f_{\mathrm{GHz}}$ ($k_x$ , $k_y$) in irreducible Brillouin zone at $a_y$ = (b) 8 and (c) 14 mm.

## 4.3 Performance of Anisotropic NZRI Medium

To realize anisotropic NZRI media, we intended to employ the specifics of rod arrays with square lattices, which demonstrated close to zero values of refractive indices near the lower frequency edges of 2nd transmission band [4]. Before employing these specifics, we had to ensure that the above property could be conserved at transforming the square lattices into rectangular ones with $a_y$ approaching 14 mm. Figure 2 (a) shows the result of calculating the refraction index values for wave propagation along the short sides of unit cells, i.e. in $x$ direction in arrays with $a_y$ changing from 8 mm to 14 mm. It is seen in the figure that at increasing $a_y$, the range of frequencies providing NZRI becomes wider, so that at $a_y$ = 14 mm, the index values remain less than 0.5 between 6.75 GHz and 7.0 GHz. It is worth noting that at these frequencies, propagation is fully suppressed along $y$-direction. Figures 2 (b) and (c) demonstrate the transformations of equi-frequency contours (EFCs) from elliptically shaped curves into flat ones at increasing $a_y$. Such flat EFCs are expected to cause strong collimation effects in PhCs. To illustrate the response of unidirectional NZRI media, we obtained wave patterns, presented in Figure 3. Fragments of dielectric rod arrays with square lattice ($a_x = a_y$ = 8 mm) and with two rectangular lattices ($a_x$ = 8 mm and $a_y$ equal to either 12 mm or 14 mm) were placed in front of the source of TM waves, which provided spreading of radiation around $x$-direction in free space. Comparison of Figures 3 (a), (b), (c), and (d) demonstrates that the media with rectangular lattices, providing unidirectional NZRI response ($a_x$ = 8 mm and $a_y$ = 14 mm), forms and guides x-directed electromagnetic beam, preventing it from becoming divergent, at the proper operating frequency of 6.85 GHz. Due to NZRI realization and superluminal wave propagation along $x$ direction in Figure 3 (d), wavelength inside PhC media ($\lambda_{PhC}$ = 130 mm) is much longer than the wavelength in free-space ($\lambda_{air}$ = 43 mm), corresponding to the refractive index value of 0.3.

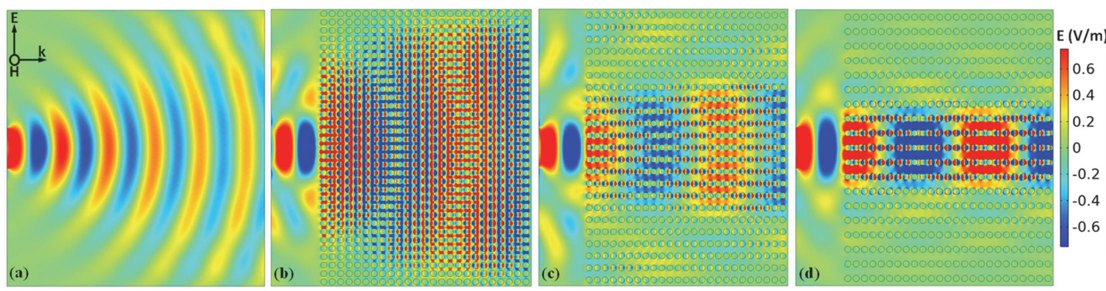


Fig. 3: Wave patterns for (a) radiation of wave source with TM polarization in free-space and in PhC media with $a_x$ = 8 mm and $a_y$ equal to: (b) 8, (c) 12, and (d) 14 mm. Frequency corresponded to the lower frequency edge of 2$^{nd}$ transmission bands for $x$-directed wave propagation.

Thus, the conducted work has shown an opportunity to design PhC-type media with NZRI properties, providing full transmission at wave incidence along one crystallographic directions and stop-band at wave incidence normally to this direction. Such types of PhCs, performing as anisotropic NZRI media, can offer collimating effects for wave sources used in microwave and photonic systems.

# References

1. L. Liberal and N. Engheta, "Near-zero refractive index photonics," Nature Photonics 11, 149-158 (2017).

2. Y. Fu et. al., "Unidirectional transmission using array of zero-refractive-index metamaterials," Appl. Phys. Lett. 104, 193509 (2014).

3. J. Luo et. al., "Arbitrary control of electromagnetic flux in inhomogeneous anisotropic media with near-zero index," Phys. Rev. Lett. 112, 073903 (2014).

4. E. Semouchkina et. al., "Superluminal media formed by photonic crystals for transformation optics-based invisibility cloaks," J. Opt. 18, 044007 (2016).

5. S. Jamilan et. al., "Spatial dispersion of index components required for building invisibility cloak medium from photonic crystals," J. Opt. 20, 045102 (2018).

6. S. Jamilan and E. Semouchkina, "Collimation effect in strongly modulated anisotropic photonic crystals with near-zero refractive indices," CLEO: QELS_Fundamental Science (2021).

# 5 Specifics of Scattering and Radiation from Sparse and Dense Dielectric Metasurfaces[5]

## 5.1 Introduction

Dielectric meta-surfaces (MSs) composed of silicon nanoparticles and exhibiting essentially lower losses compared to plasmonic MSs, attract increasing attention at the development of novel photonic de vices. In particular, it was demonstrated in [1-3] that scattering from MSs formed from dielectric resonators (DRs) made of silicon rods/disks could be controlled by changing the height-to-diameter ratio of the particles. Such geometric changes were shown to shift the frequencies of magnetic and electric Mie-type resonances in DRs up to their coincidence, when full transmission of incident waves through MSs was observed with $2\pi$ phase control [3]. These results were the reason for projecting that dielectric MSs will be the basic media for developing new optical devices, controlling both intensity and phases of scattered waves that is required for obtaining holographic images [4]. The observed phenomena were explained using the concepts of directional scattering from dielectric spheres at so-called Kerker's conditions [5, 6] that were thoroughly investigated in both microwave and optical ranges [6-10]. Similar approaches were used in following works (for example, [11]), although the physics of the observed phenomena still called for clarification. In particular, the effects of particle resonance integration in MSs were omitted from consideration in [1-3], and, instead, metamaterials concepts, assuming that the response of the entire array could be represented by the response of a single "meta-atom", were used. Meanwhile, MSs investigated in [1-3] were formed from dense DR arrays, in which interaction of particle resonance fields should be expected. In our earlier work in 2005 [12], we described such interaction and coupling phenomena, which were later observed in other works on metamaterials [13-15]. When recently conducting a set of numerical experiments [16] with the same type of arrays as those used in [3], we observed strong effects of lattice parameters on MS responses, including their forward (FS) and backward (BS) scattering. It was shown that at so small lattice constants as those used in [3], DRs in MSs appeared strongly coupled that affected observed resonance frequencies and interaction between MSs and incident waves.

In this work, we present the results of a broader investigation aimed at deeper understanding of various cooperative phenomena in dielectric MSs, including interactions between electric and magnetic resonances within DRs, as well as inter-resonator interactions in arrays. Obtained results are important for understanding the complexity of MS responses and provide the guidance for choosing optimal MS design. We start from the analysis of responses from single DRs placed in free space and then turn to the phenomena in arrays.

---

[5]Reprinted from 'S. Jamilan, G. Semouchkin, N. P. Gandji, and E. Semouchkina, "Specifics of Scattering and Radiation from Sparse and Dense Dielectric Meta-surfaces," Journal of Applied Physics, 125 (16), 163106, 2019'; with permission from © AIP Publishing.

## 5.2 Models and Methodology of Numerical Experiments

"Meta-atoms" of MSs in these studies were represented by silicon DRs of various shapes (Fig. 1a). Dielectric constant of DRs was 12.25 that is typical value for silicon at optical frequencies [17]. Cylindrically shaped DRs were similar to those employed in [3], however, in difference from [3], the diameter of DRs was not changed to control their resonances and kept equal to 240 nm. Instead, for varying resonance frequencies, the height of DRs was changed from 240 nm down to 60 nm (Fig. 1a). Such approach, first used in [16], provided an opportunity for investigating the effects of lattice parameters on MS responses. Comparing the responses of DRs of different shapes allowed for observing the transformation of well-studied responses of dielectric spheres into responses of disk-shaped DRs.

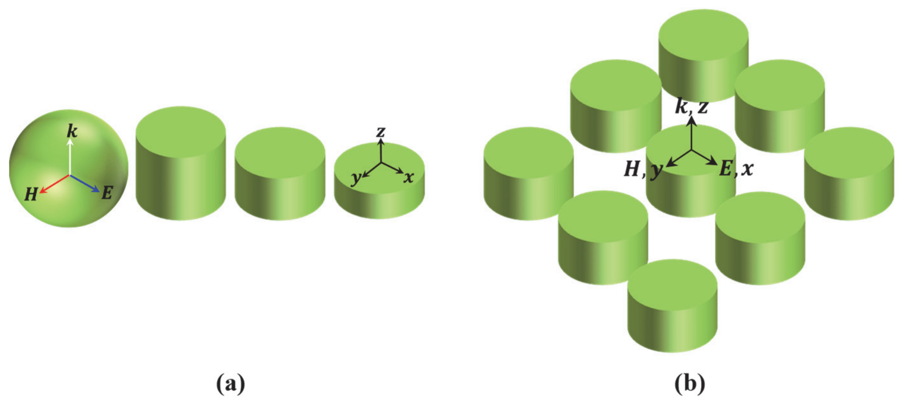


Fig. 1. Examples of (a) DRs and (b) 3 x 3 fragments of MSs used in these studies.

Simulations were performed by using Frequency Domain Solver of COMSOL Multiphysics and verified using Time Domain Solver of CST Microwave Studio software packages. Plane waves, incident normally to MSs (along Z-axis in Fig. 1), were used for excitation. To evaluate scattering from MSs, we, first, simulated S - parameter spectra, as it was done in [1-3], Such approach suggested representing periodic DR arrays by one-cell model, conventionally used at modeling homogenized metamaterials, when one cell is assumed representing the entire medium. We employed one-cell model with periodic boundary conditions (BCs) for calculating S-parameters spectra, to characterize interaction between MSs and incident waves. In addition, to describe radiation from resonating MSs, we employed proposed in COMSOL technique for evaluating FS and BS spectra from finite size samples and also simulated far-field patterns, thus considering MSs as sources of radiation comparable to antennas. The latter approach is often used at the studies of resonance scattering, which could be also referred to as resonance radiation and which is expected to play an important role in MS responses. It could be noted that at strong coupling between DRs, employment of one-cell model requested justification. However, at weak interaction between DRs, i.e. in the cases of sparse arrays, one-cell model was expected to provide adequate representation of array interaction with incident waves. To characterize resonance scattering/radiation from MSs, we used MS fragments consisting of 9 (3 x 3) unit cells (Fig. 1b), which were found to represent MSs properly, based on experiments with fragments of various sizes. Finally, to characterize resonance fields and coupling effects, we simulated field patterns in cross-sections of MS fragments applying periodic boundary conditions at their boundaries.

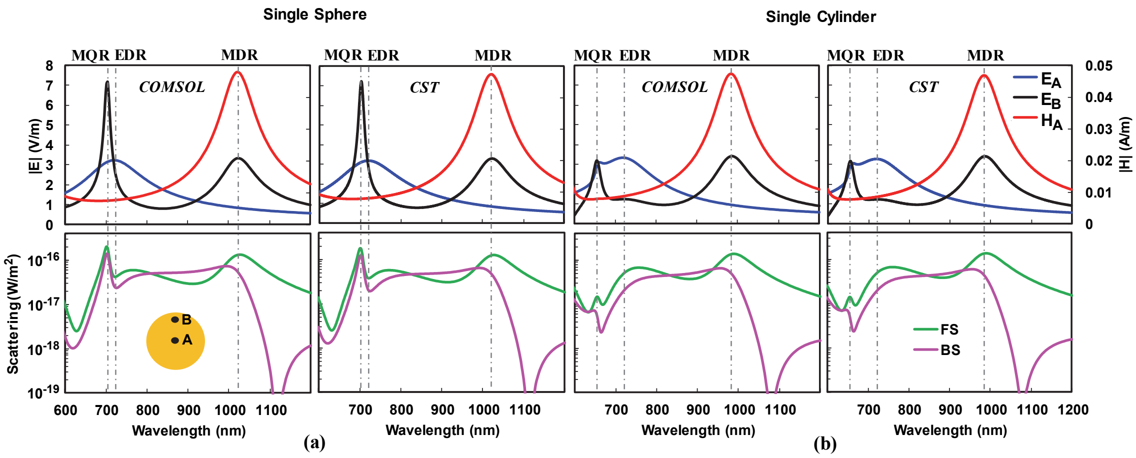


Fig. 2. Simulated using COMSOL Multiphysics and CST Microwave Studio packages spectra of signals from E- and H-field probes placed in points A and from E-field probes placed in points B (upper row) and spectra of BS and FS power density (lower row) for DRs with (a) spherical and (b) cylindrical shapes. Inset shows positions of field probes in central XZ cross-section of DRs. Diameter of spheres is 278 nm, while cylindrical DRs have both diameter and height equal to 240 nm.

## 5.3 Analysis of Resonances in Single Particles and Scattering from Them

The upper row in Fig. 2 presents spectral changes of signals from E (electric) and H (magnetic) field probes placed either in centers (points A) of spherical and cylindrical DRs excited by plane waves or in points B near the edges of Z-directed diameters of central XZ cross-sections. Signals from points A allowed for observing electric (EDR) and magnetic (MDR) dipolar resonances, while signals from points B were characterizing magnetic quadrupolar resonances (MQR) formed at blue tails of EDRs. Diameters of spherical DRs were slightly increased compared to diameters of cylindrical DRs to provide in two types of DRs similar frequencies of EDRs and MDRs. As seen in the graphs, while the strengths of dipolar resonances in two DRs are comparable, MQR in spheres is twice stronger than that in cylindrical DRs and $f_{MQR}$ for spheres is closer to $f_{EDR}$. In general, however, the spectra of responses from two DR types, as well as their BS and FS spectra, given in the lower row of Fig. 2, demonstrate similar features at $f < f_{EDR}$ ($\lambda > \lambda_{EDR}$) and do not reveal any differences at employing various software in simulations.

The spectra of BS and FS for two types of DRs demonstrate higher BS compared to FS in the range between EDRs and MDRs that is characteristic for the 2nd Kerker's condition and show deep drops of BS (at seemingly undisturbed FS) at $f < f_{MDR}$ ($\lambda > \lambda_{MDR}$) that is typical for the 1st Kerker's condition. Such similarity confirms that dipolar resonances in cylindrical DRs with heights close to their diameters are analogous to Mie resonances in spheres. Difference in BS and FS spectra of two DRs at $f > f_{EDR}$ ($\lambda < \lambda_{EDR}$) appears due to differences in MQR responses.

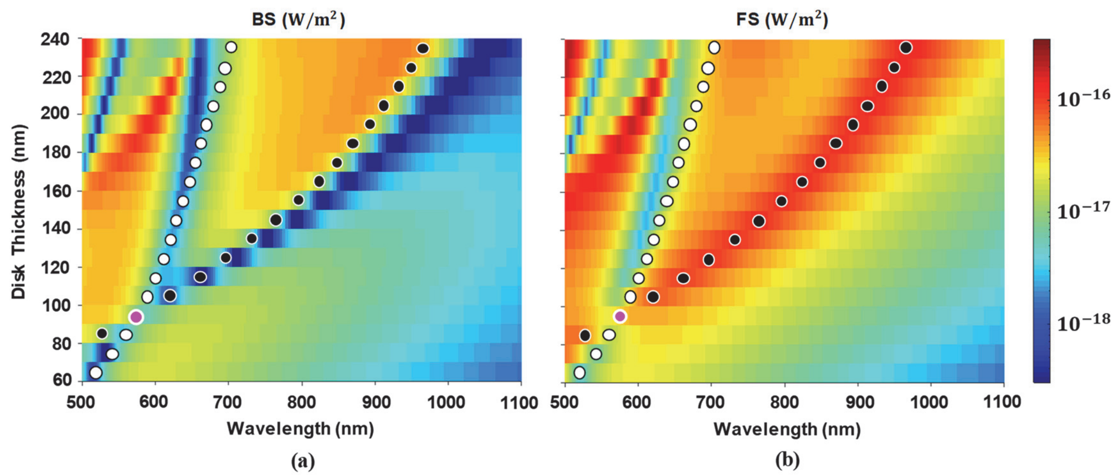


Fig. 3. Spectral distributions of (a) BS and (b) FS for single cylindrical DRs of various heights at occurrence of EDRs, MDRs, and MQRs. Diameters of DRs are equal to 240 nm. White and black colored circles mark spectral positions of EDRs and MDRs. Purple circles on two graphs mark the case, when frequencies of EDR and MDR coincide.

Fig. 3 presents spectral distributions of BS (Fig. 3a) and FS (Fig. 3b) power density, provided by single cylindrical DRs of different heights at their excitation by incident plane waves. The positions of EDR and MDR, obtained from the spectra of signals from E- and H-field probes placed in DR centers, are marked in the presented patterns by white and black circles, respectively. It is seen in the figures that the curves, representing EDRs and MDRs, cross each other at DR heights close to 90 nm that is in agreement with the data in [1-3]. However, these crossings are not accompanied by either increase of FS or BS, or by deep drops of these values, which would allow to detect specific directional scattering from MSs composed of 90 nm high DRs. It is well seen that, while MDRs provide strong and wideband FS, which gradually decreases at smaller DR heights, EDRs produce comparable FS only at DR heights close to 240 nm, while at heights below 210 nm, FS, caused by EDRs, drops down by an order of magnitude and more. BS at EDRs also looks significantly weaker than BS at MDRs at DR heights, starting from 240 nm down to, at least, 140 nm. It is worth noting here that meaningful FS and BS can be seen at MQRs, visualized at higher frequency sides of the blue colored "canyons" adjusting to the curves of EDRs. A deeper and wider "canyon" is seen in BS pattern to the right of the curve of MDRs. It seems related to realizing 1st Kerker's condition (see Fig. 2), i.e. condition for destructive interference of waves scattered by EDR and MDR in backward direction. It is important to mention that the tails of two "canyons" in BS pattern come closer to each other at DR heights of about 110 nm, when strong FS provided by MDR still exists. It shows an opportunity for obtaining directional scattering at MDR frequencies.

Fig. 4 shows changes of resonance responses and BS/FS spectra for single cylindrical DRs at decreasing their heights from 140 nm down to 90 nm (to the case when frequencies of EDR and MDR coincide). It can be seen that at the DR height of 140 nm, when EDR and MDR are still relatively far from each other, they affect BS/FS spectra differently. At EDR, both BS and FS drop down, demonstrating the same trend as could be noticed for spheres in Fig. 2, while at MDR, when FS, as in the case of spheres, remains high, BS experiences wideband descend, approaching deep drop below $10^{-19}$ W/m$^2$, which is defined by realizing the 1$^{st}$ Kerker's condition.

At the smaller DR height of h=110 nm, the Kerker's condition gets realized exactly at the frequency of MDR, It is worth mentioning that the observed effect looks accompanied by decrease of MDR strength. At further decrease of DR height down to 100 nm, the BS/FS drops lose their depths in the vicinity of EDR and the Kerker's effect also decreases, although EDR and MDR frequencies still remain different. At h=90 nm, when EDR and MDR coincide, all features of BS/FS spectra, specific for resonances, continue to degenerate, so that considering the observed scattering as clearly directional phenomenon, defined by the Kerker's effect, loses any sense.

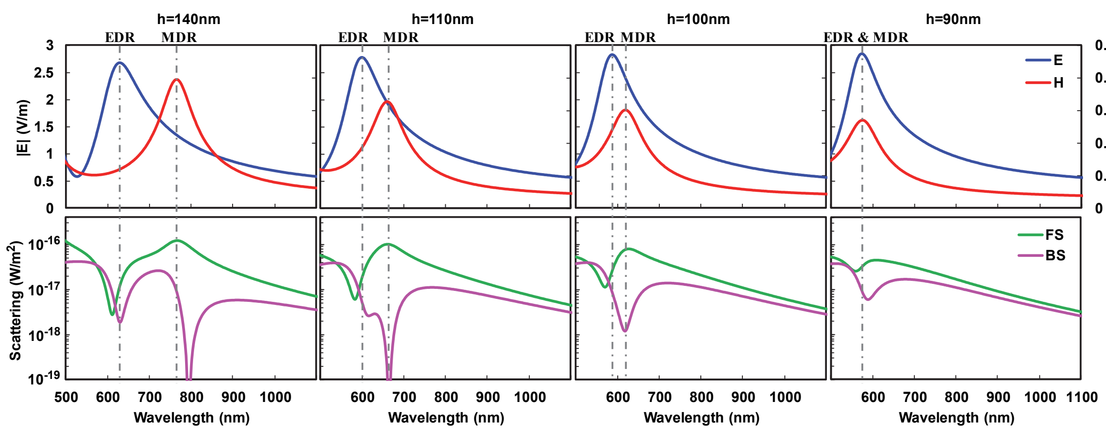


Fig. 4. Upper row: spectra of signals from E- and H-field probes placed in centers of DRs with heights from 140 nm down to 90 nm. Lower row: respective BS/FS spectra. Disk heights are indicated above the columns.

To understand the reasons, which cause deterioration of scattering capabilities of disk resonators at decreasing their heights, we have simulated field distributions in disk cross-sections at EDR and MDR in DRs of various heights. It could be inferred that in disk DRs of small heights, excitation of competing resonances could be incapable of forming authentic dipoles. Fig. 5 presents the data confirming significant distortions of resonance modes, when EDR and MDR frequencies approach each other. While at h=150 nm field patterns at both resonances still look corresponding to typical images of electric and magnetic dipoles directed along the normal to each other diameters of cylindrical DR, at DR height of 100 nm, we observe shifting of the location of electric dipole center along Z-axis and curving of H-field lines around the shifted position of the electric dipole center. At h=90nm, the above trends become enhanced, so that electric dipole starts to look as formed near the upper disk surface, while magnetic dipole – as represented by an arc of a circle. Such transformations of the resonance modes could be responsible for described above distortions in the spectra of BS and FS from disk resonators.

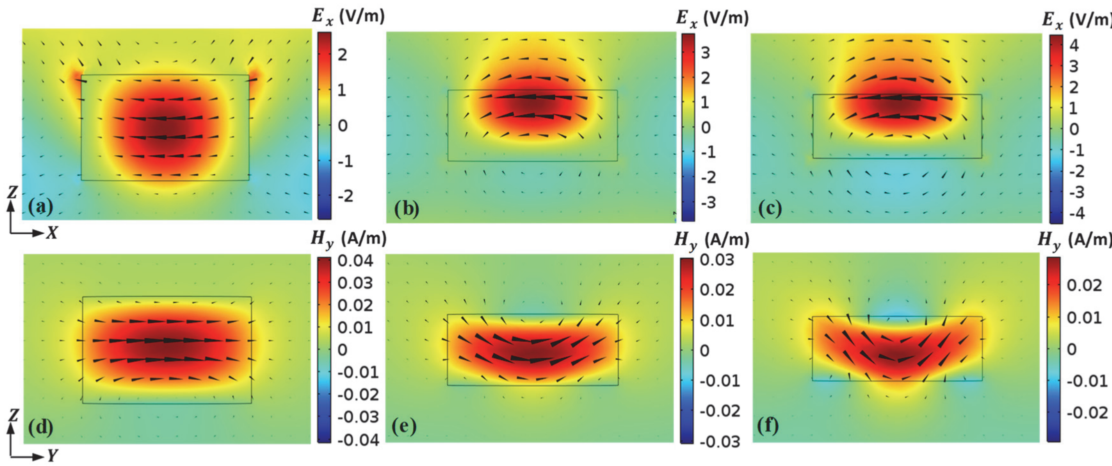


Fig. 5. Upper row – E-field patterns in XZ cross-section of DRs at EDRs: (a) λ=638nm, h=150nm, (b) λ=588nm, h=100nm, (c) λ=574nm, h=90nm. Lower row – H-field patterns in ZY cross-section at MDRs: (d) λ= 793nm, h=150nm, (e) λ=619nm, h=100nm, (f) λ= 574nm, h=90nm.

## 5.4 Effects of DR Arraying on BS/FS and S21 Spectra of MS Fragments

As we have shown earlier in [16], DR arraying could seriously affect MS responses and cause changing of their resonance frequencies and scattering parameter spectra. According to [16], such small lattice constants, as those used in [1-3], i.e. of 330 nm, made resonance fields of cylindrical DRs with diameters of 240 nm strongly coupled, so that complicated grid-like field patterns, incorporating both dipole fields inside DRs and the fields in gaps between resonators became seen in planar cross-sections of MS. These data imply that responses of dense MS could not be considered as the sum of responses from independent DRs and that effects of integration of elementary responses in MS media should be accounted for. However, in this section, we first analyze relatively soft resonance integration in MSs, expected, according to [16], at the array lattice constant of 450 nm, and then, in the following section, switch to the analysis of cases with significant integration of resonances.

Fig. 6 presents spectral distributions of BS and FS power density provided by 3 x 3 fragments of MSs composed of cylindrical DRs of various heights. From comparison with

Fig. 3 for single resonators, it is seen that the basic features of respective distributions are quite comparable. However, there are aslso some differences between distributions in Figs. 3 and 6, i.e. lower frequencies of EDRs and higher frequencies of MDRs, higher BS at both EDR and MDR, at also higher FS at EDR. It is also worth mentioning that curves marking resonances in Fig. 6 have crossings at larger DR height and at higher wavelength compared to crossings in Fig. 3. In addition, Fig. 6 demonstrates relatively high BS intensities in the spectral regions between EDR and MDR, and low FS intensities in these regions. These specific features are characteristic for realizing the Kerker's conditions of 2nd type and, correspondingly, for directional scattering with dominant backward radiation (as confirmed later in Fig. 8a). Presented data show that DR arraying provides a wide bandwidth for this phenomenon. It is also worth noting the differences in appearances of "canyons" with suppressed BS at $f < f_{MDR}$ ($\lambda > \lambda_{MDR}$) and at $f > f_{EDR}$($\lambda < \lambda_{EDR}$), and with suppressed FS at $f > f_{EDR}$($\lambda < \lambda_{EDR}$) in Figs. 3 and 6, although it is difficult to qualitatively describe these differences, since the scales of power density in two figures differ by about two orders of magnitude.

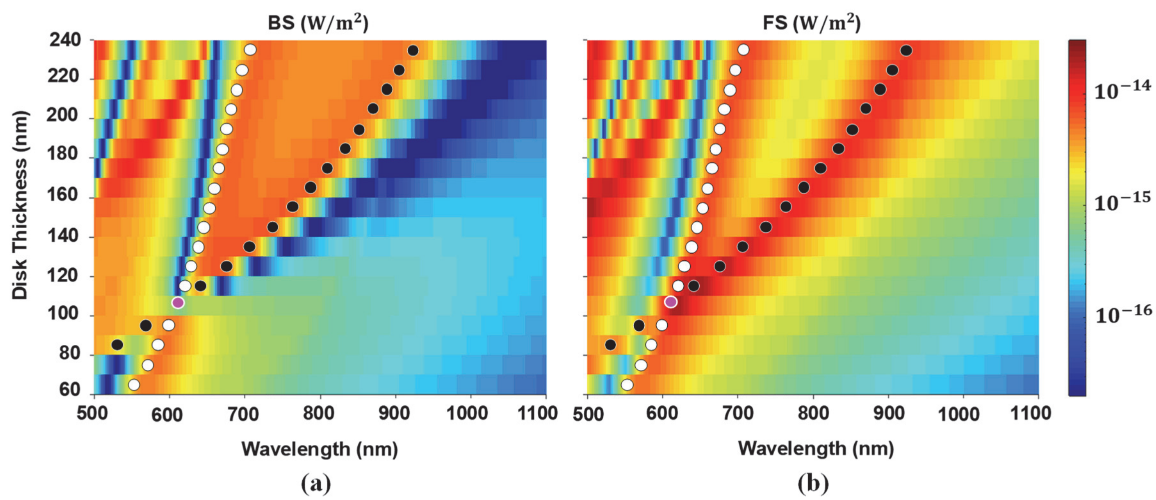


Fig. 6. Spectra distributions of BS and FS power density for 3 x 3 fragments of MSs composed of cylindrical DRs with heights ranging from 240 nm to 60 nm. Diameters of DRs are equal to 240 nm, lattice constants of MSs are 450 nm. Spectral positions of EDRs and MDRs are marked, respectively, by white and black colored circles. Purple circles on two graphs mark the case, when frequencies of EDR and MDR coincide.

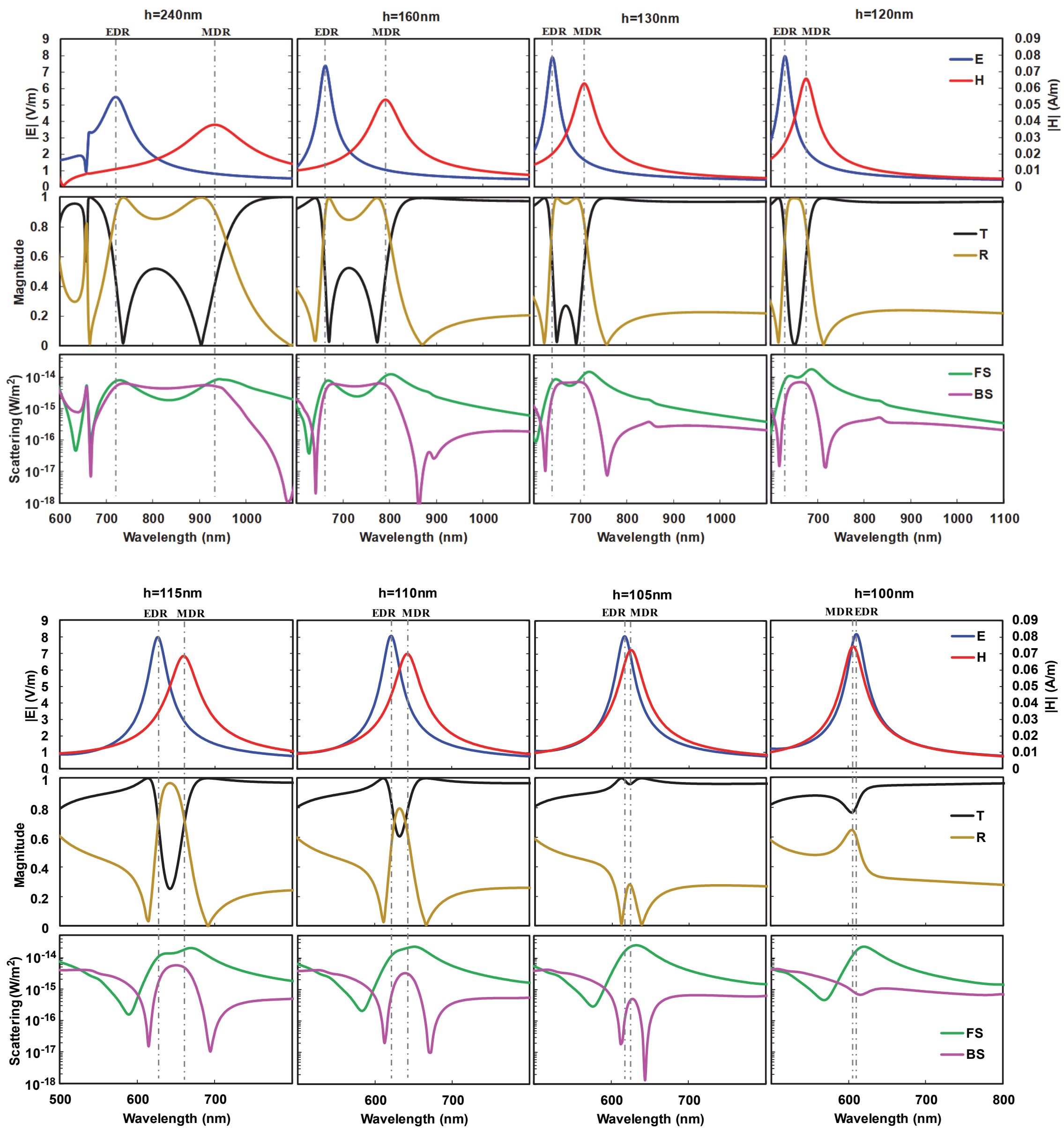


Fig. 7. Spectral distributions of EM responses from MSs differ by DR heights (shown above each column). Upper group of data – for h, nm: 240, 160, 130, and 120. Lower group of data – for h, nm: 115, 110, 105, and 100. Upper row in both groups: signals from E- and H-field probes in the centers of DRs at modeling MSs by single cells with periodic boundary conditions; middle row: S-parameters (|S21| = T and |S11| = R) simulated at above conditions; lower row: BS and FS spectra for 3 x 3 fragments of MSs.

Fig. 7 presents spectral distributions of signals from E- and H-field probes placed in DRs to control resonances in MSs, scattering parameter spectra calculated for infinite MSs, and spectral distributions of BS and FS power density characteristic for 3 x 3 fragments of the same MSs. All data were obtained for MSs composed of DRs with the heights chosen within the range from 240 nm down to 100 nm. As seen in Fig. 7, at h=240 nm, i.e. when DR responses are comparable to responses of spheres, EDR frequency for the array is close to the EDR frequency for single resonator (Fig. 1b), while MDR frequency for the array appears to be higher than that for single DR (Fig. 1b). EDR in the array looks stronger, while MDR – weaker than in the case of single resonator, and Q-factors of resonances in the array seem to be a little higher than those in the case of single DR. All these changes are expected to happen at arraying, which, in fact, should slightly decrease the space for forming the field "halos" of DR resonances. It could be noted that MQR is not distinctly seen in the spectra presented in Fig. 7, in contrast to the case of single DR, however, despite of this, MQR still seems located at the same frequency (i.e. at $\lambda$=650 nm), since field patterns in DR cross-sections (not presented here) confirm characteristic for MQR field distributions just at this frequency. MQR also appears responsible for the specific changes observed in the scattering parameter spectra and in the BS/FS spectra at $f>f_{EDR}$. In the S-parameter spectra, while moving from EDR to MQR, we see, first, a deep drop of S11, while S21 approaches the maximum value of "1". Then, at $f_{MQR}$, S21 drops down, while S11 forms a peak. The values of both BS and FS drop down closer to MQR but then at $f=f_{MQR}$ also form peaks.

At frequencies below $f_{EDR}$ ($\lambda>\lambda_{EDR}$), S21 spectrum demonstrates clear dips at frequencies close to $f_{EDR}$ and $f_{MDR}$. Such dips are often considered as a proof of resonances, which are expected to cause total reflection and no transmission for incident waves. However, it is seen from Fig. 7 that at the resonance frequencies, the values of S21 and S11 appear equal. It means that the energy scattered in forward direction becomes equal to the energy scattered in backward direction that is characteristic, in particular, for the bagel-type radiation patterns. Described features remain clearly seen at decreasing DR heights in MSs down to 120 nm, and even to 110 nm when, instead of two overlapped S21 dips, one dip is observed, which is decreasing at decreasing DR heights. It is worth noting here, however, that FS spectra do not demonstrate any dips or drops and look comparable to spectra representing the power radiated by single particles at resonances (see Fig. 2). In contrary to FS, deep drops observed in BS spectra of MS fragments appear well correlated with drops in the spectra of S11. As seen in Fig. 7, this correlation is conserved at the heights of DRs ranging from 240 nm down to 105 nm, and only at the height of about 100 nm, when frequencies of EDR and MDR coincide, it disappears because of degradation of all features of the spectra. At small DR heights, the frequencies of BS and S11 drops at $f>f_{EDR}$ ($\lambda<\lambda_{EDR}$) tend to become very close to $f_{EDR}$, while FS drops get increasingly separated from BS drops and shifted to higher frequencies (shorter $\lambda$). BS drops, which are observed at $f<f_{MDR}$ ($\lambda>\lambda_{MDR}$) in spectra of all MSs with DR heights ranging from 240 nm down to 105 nm could be, without a doubt, related to realizing Kerker's conditions of the 1$^{st}$ type as in the single resonators. In MSs with smaller DR heights, the frequencies, at which these drops occur, get significantly higher, i.e. they shift following $f_{MDR}$ to approach $f_{EDR}$. To additionally verify the relation of BS drops at $f<f_{MDR}$ to the Kerker's conditions, we simulated far-field patterns provided by radiation from MS fragments at the frequencies of interest. Fig. 8b shows that the latter BS drops mark the formation of far-fields

corresponding to directional FS expected at Kerker's conditions. Common features of BS and S11 drops at $f<f_{MDR}$ and at $f>f_{EDR}$ allow for suggesting that the latter drops are also defined by realizing conditions similar to Kerker's conditions of the 1st type. In principle, approaching these conditions at $f>f_{EDR}$ could be expected, since phase jumps of dipole field oscillations at EDR and MDR should make the relation between phases of oscillations in high-frequency tails of EDR and MDR close to the relation characteristic for $f<f_{MDR}$.. Far-field patterns characterizing radiation from MS fragments at frequencies corresponding to drops in BS and S11 at $f>f_{EDR}$ (Fig. 8c) confirm obtaining at these frequencies clearly expressed directional FS, typical for the 1st Kerker's conditions.

The features of S11 and BS/FS spectra of MSs at heights of DRs providing coincidence of EDR and MDR frequencies need additional comments. It is well seen from Fig. 7 that this coincidence leads to degradation of characteristic features of both BS and FS spectra, i.e. no deep drops can be seen any more and, therefore, a discussion about realizing Kerker's conditions either at $f<f_{MDR}$ or at $f>f_{EDR}$ loses sense. BS intensity increases all over the spectrum, approaching FS intensity. This does not allow for obtaining desirable directivity of scattering (Fig. 8d). It is interesting to note that, in difference from the data in [1-3], our data show a drop of S21 at weak peaking of S11 at the common resonance frequency of EDR and MDR. This also shows that coincidence of EDR and MDR does not provide an optimal solution for obtaining unidirectional scattering, while much better result can be achieved at employing MSs with DRs of larger heights providing close, but distant positions of dipolar resonances in the spectrum.

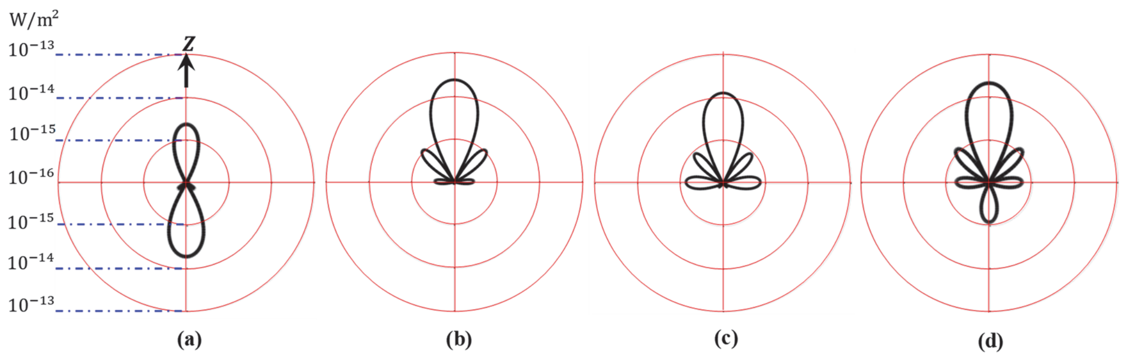


Fig. 8. Far-field patterns representing radiation from fragments of MSs: (a) at $f_{EDR}>f>f_{MDR}$, for DR heights within 120 nm<h< 240 nm, when realizing of Kerker's condition of the 2nd type is expected (exemplified at h=160nm at λ=731nm); (b) at BS drops observed at $f<f_{MDR}$, when realizing of 1st Kerker's condition is expected (exemplified at h=105nm at λ=643nm); (c) at BS drops observed near $f_{EDR}$ for smaller DR heights (exemplified at h=105nm at λ=612nm); (d) at EDR and MDR approaching coincidence, when DR height is of about 100 nm (exemplified at h=100nm at λ=624nm). Black arrow shows the direction of wave incidence.

Finally, it is worth pointing out that observed correlation between BS spectra of 3 x 3 fragments of MSs and S11 spectra, obtained for unit cells with periodic boundary conditions, i.e. for infinite MSs, confirms that at lattice parameter of 450 nm, single unit cells of MSs are still capable of representing MS responses adequately. This also confirms that 3 x 3 fragments of MSs with lattice constant of 450 nm can be used to represent radiation capabilities of the entire MSs.

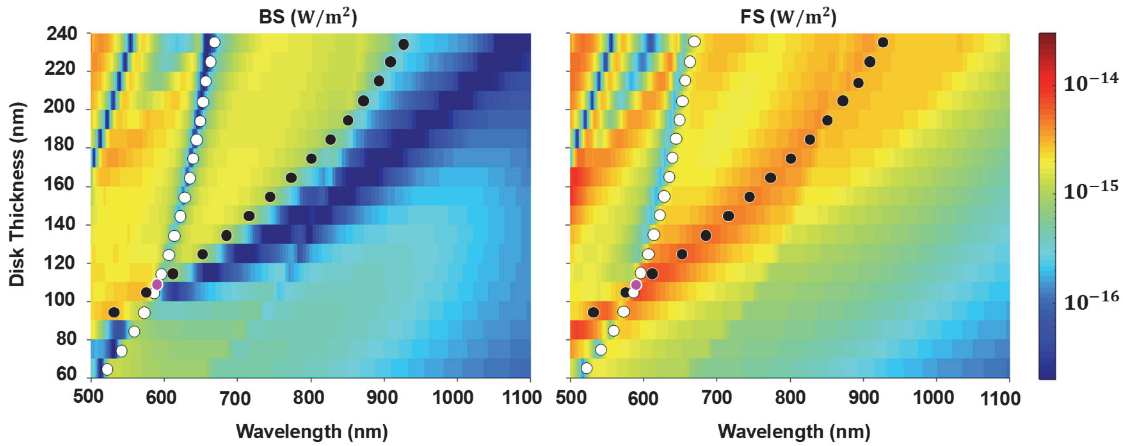


(a) (b)

Fig. 9. Spectral distributions of BS and FS power densities for 3 x 3 fragments of MSs composed of DRs with heights ranging from 240 nm to 60 nm. Lattice constants of MSs are 300 nm, diameters of DRs are equal to 240 nm. Spectral positions of EDRs and MDRs are marked, respectively, by white and black colored circles. Purple circles on two graphs mark the case, when frequencies of EDR and MDR coincide.

## 5.5 Effects of Lattice Constant Decrease on BS/FS and S21 Spectra of MS Fragments

In this section, the responses of MSs with essentially smaller lattice constants of 300 nm are investigated for comparison with the results presented in the previous section. At such small lattice constants, we earlier observed significant changes in MS performance [16], pointing out at the formation of integrated responses of the media, different from the responses of single particles. Fig. 9 presents spectral distributions of BS and FS power densities provided by 3 x 3 fragments of MSs composed of cylindrical DRs of various heights. From the comparison of Fig. 9 with Fig. 6, obtained for MSs with lattice constants of 450 nm, it is seen that, although decreasing the lattice constant down to 300 nm does not eliminate main features of spectral distributions of BS abd FS, essential changes of these distributions are obvious. First, total decrease of BS power density in the area between EDR and MDR, especially at smaller DR heights, can be observed. FS power density is also decreased, but not so strongly. In addition, FS power density becomes more uniformly distributed in the region between EDR and MDR, so that no so significant FS decrease in the cental part of this region, comparable to the decrease seen in Fig. 6, is registered. At total decrease of BS power, it seems that Kerker's conditions of the 2$^{nd}$ type could not be realized in densely packed MSs. One more visible change is blue shifts of EDR positions in the spectra. Similar EDR shifts at decreasing MSs' lattice constants were noticed in[16]. As the result of this shifting, the curve of white circles marking EDRs in BS pattern looks coinciding with the curve marking maximal canyon depths. Shifting of EDR frequencies also places the curve of white circles, connecting EDR markers, in touch with the "canyon" observed in FS pattern, while at lattice constants of 450 nm, similar curve was located at relatively significant distance from the "canyon".

This happens, since the spectral position of the "canyon" in FS pattern is more stable with respect to lattice constant changes, than spectral positions of EDRs. It follows from the data, presented in Fig. 9, that in dense MSs, EDRs are not able to support strong FS power, as they do in more sparse MSs (Fig. 6). Considering MDRs, it can be noticed that, for MSs with lattice constants of 300 nm, the curves of black circles, marking MDRs in BS/FS patterns in Fig. 9, have less steep slopes than those in Fig. 6. This means that MDR frequencies also experience blue shifts, which become bigger at smaller DR heights, although still remain smaller than EDR shifts. It is worth noting that, as the result of different characters of EDR and MDR shifting at decreasing the lattice constants, the crossing of the curves, connecting EDR and MDR markers, appears at approximately the same frequency and at appoximately the same DR height for arrays with large (450 nm) and small (300 nm) lattice constants.

Fig. 10 presents spectral distributions of signals from E- and H-field probes placed in DRs to control resonances in MSs, scattering parameters spectra calculated for infinite MSs using one-cell model with periodic boundary conditions, and spectral distributions of BS and FS power density characteristic for 3 x 3 fragments of the same MSs. The data presented in Fig. 10 were obtained, as in the previous section, for MSs composed of DRs with the heights chosen within the range from 240 nm down to 100 nm. As seen in the figure, at h=240 nm, MQR demonstrates Fano-type shape of its resonance curve and is located in the spectrum much closer to EDR, compared to the case of MSs with the lattice constant of 450 nm. Characteristic for Fano-type resonances drops of E-field probe signals down to zero on the higher frequency sides of EDRs continue to be seen at decreasing DR heights down to 120 nm, however, at this decrease, they shift further away from EDR to blue side of the spectrum. Considering the difference between S-parameters spectra for MSs with DR heights of 240 nm and 160 nm and also the difference in BS/FS spectra of respective MSs at $f>f_{EDR}$, it can be concluded that at h=160 nm the MQR related effects leave the EDR vicinity.

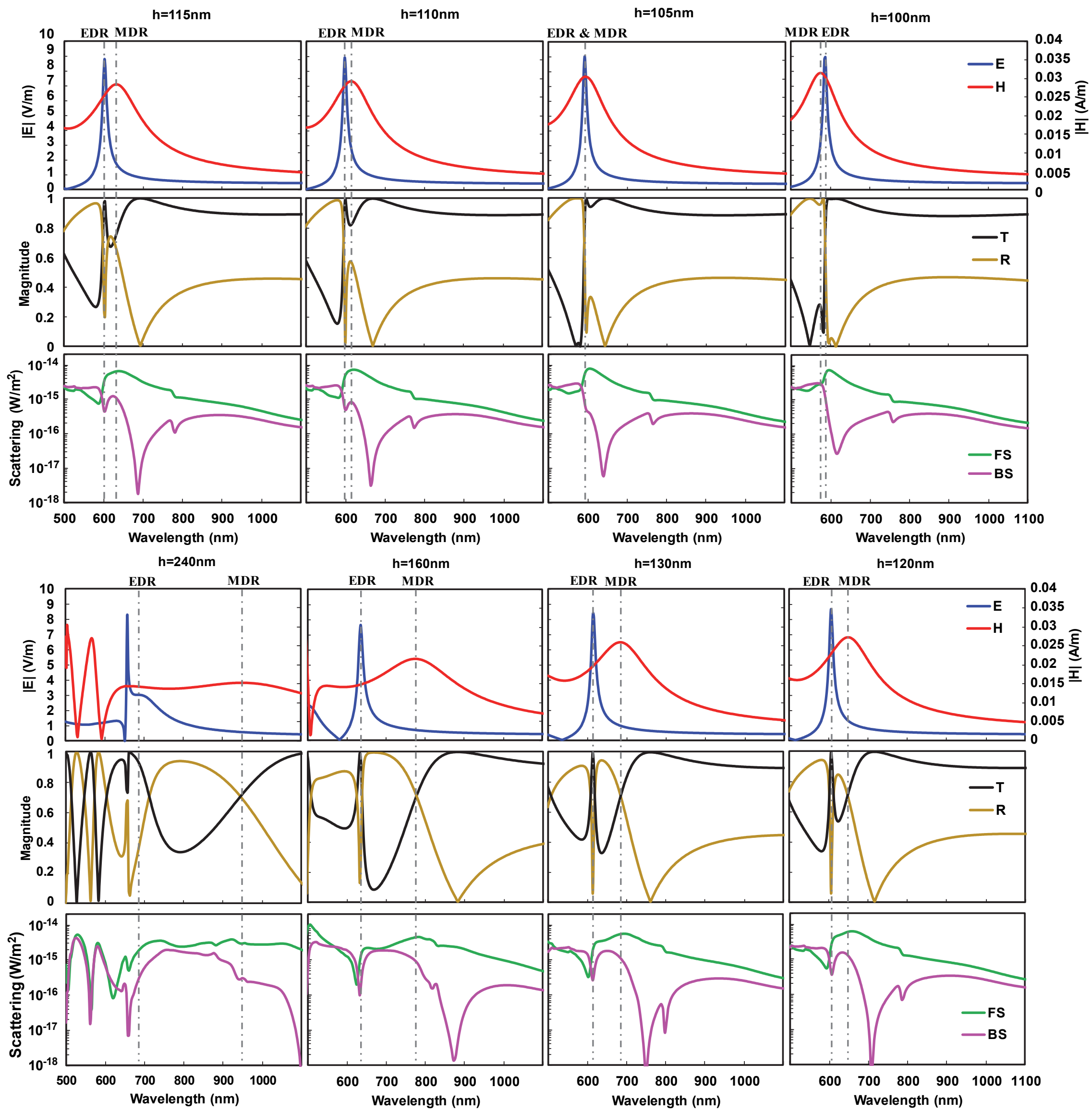


Fig. 10. Spectral distributions of EM responses from MSs, which differ by DR heights (shown above every column). Upper group of data – for h, nm: 240, 160, 130, and 120. Lower group of data – for h, nm: 115, 110, 105, and 100. Upper row in both groups: signals from E- and H-field probes located in the centers of DRs at modeling MSs by single cells with periodic boundary conditions; middle row: S-parameters simulated at above conditions; lower row: BS and FS spectra for 3 x 3 fragments of MSs.

However, a new phenomenon appears instead: a narrowband drop of the reflection coefficient S11 down to almost zero accompanied by sharp peaking of S21 parameter up to 1 exactly at EDR frequencies. At the first glance, the new phenomenon could be compared to described in Section 3 scattering in sparse MSs at $f>f_{EDR}$, which we found to be similar to the effects observed at $1^{st}$ Kerker's condition, with typical deep drops of BS at relatively high FS. However, the phenomena in sparse MSs were always observed at $f > f_{EDR}$ and not at $f=f_{EDR}$. In addition, they were not narrowband and, instead of peaks of transmission, demonstrated relatively high transmission in a wide band. Therefore, the new phenomenon with delta-function-like changes in scattering parameters spectra at $f=f_{EDR}$, especially in MSs with h=120mm and h=130 nm, resemble, rather, electromagnetically induced transparency (EIT). Taking into account observations of Fano resonances in MSs, which, as known, are related to interference processes, realization of EIT in dense MSs could be expected, even though additional studies should be conducted for clarifying the underlying physics. In any case, it is not excluded that just EIT was responsible for observed in [3] full transmission through MSs at EDR and MDR coincidence.

In difference from EDRs, MDRs in dense MSs do not show new specifics, neither in S11/S21 spectra, nor in BS/FS spectra, compared to MDRs in sparse MSs, except for the coincidence of MDR frequencies with frequencies, at which S parameter spectra demonstrate crossings of S11 and S21 spectra. It is seen from Fig. 10 that, in difference from the data for sparse MSs, S parameters spectra of dense MSs do not show deep drops of S21, demonstrating just decreased S21 values at frequencies $f_{EDR}>f>f_{MDR}$. In contrast, S11 values increase in this frequency range, especially at DR heights exceeding 120 nm. At smaller DR heights, decrease of S21 and increase of S11 looks gradually degrades because of narrowing the gap between EDR and MDR owing to the fact that blue shifts of MDRs exceeds blue shifts of EDRs. In difference from MSs with lattice parameter of 450 nm, approaching coincidence of MDR and EDR frequencies is not accompanied by disappearance of BS drop caused by realizing the Kerker's conditions. As seen in columns of Fig. 10 for two smallest DR heights, BS drops continue to be well seen in BS/FS spectra as at coincidence of resonances, so even at reversing positions of EDR and MDR in the spectra. It is worth mentioning here that FS increases at decreasing DR heights, however, the peak values of this radiation are observed at frequencies slightly exceeding the resonance frequencies. According to the results presented in Fig. 10, better directionality of scattering should be observed not at the common for EDR and MDR resonance frequency of 600 nm, but at the frequency, which provides the realization of Kerker's condition (640 nm).

To understand the reasons, defining changes of MS responses at decreasing the array packing density, we simulated field patterns in cross-sections of MSs with different lattice constants and with different DR heights. Fig. 11 presents respective distributions for electric fields.

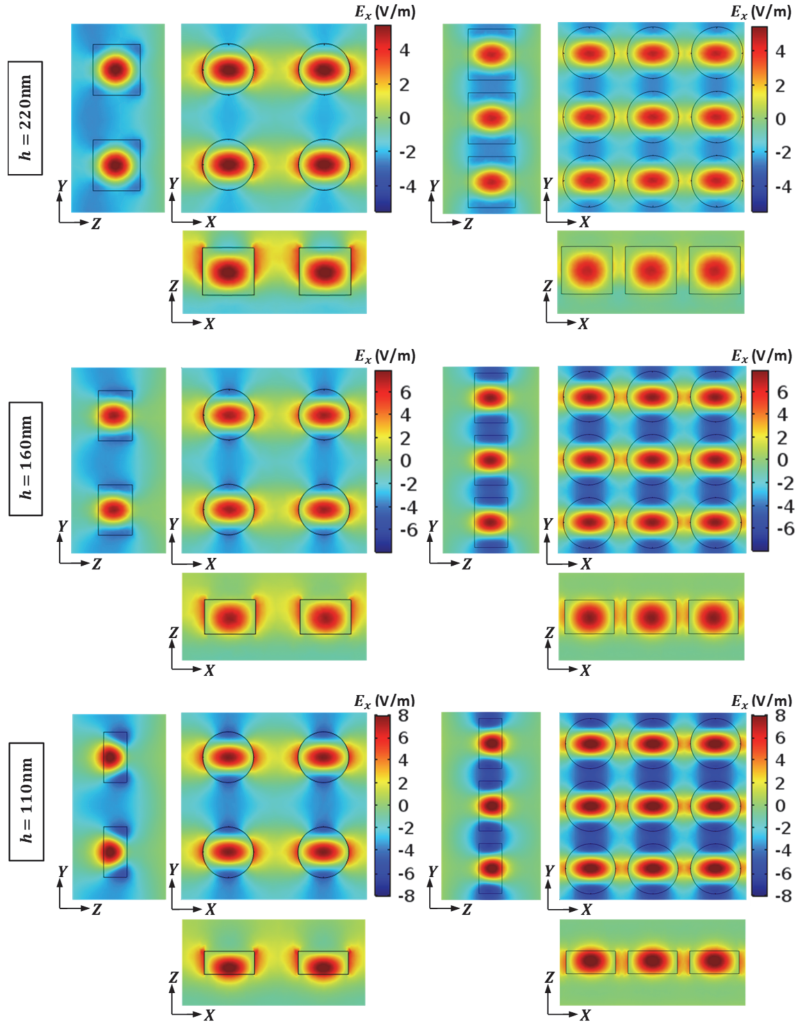


Fig. 11. Distributions of E- fields in XY, YZ, and XZ central cross-sections of MSs composed of DRs with heights: 1st row - h=220 nm; 2nd row - h=160 nm; 3d row - h=110 nm with the lattice constants: of 450 nm (left column) and 300 nm (right column). All patterns are obtained at the frequencies of EDRs.

As seen in the figure, all MSs under study have demonstrated, in their central XY cross-sections, grid-like field distributions characteristic for coupled DR arrays [18]. The lines of grids are defined by X and Y axes passing through the centers of DRs. Grid lines, going along X-axis seem to be formed by extensions of resonance fields, which accompany the formation of electric dipoles in the centers of DRs. The fields in these extensions on two sides of each X-oriented gap between DRs look co-directed with dipoles and demonstrate the trend for overlapping.  The sequences of Y-oriented gaps seem forming Y-directed lines of the grid. In Y-oriented gaps, electric fields appear directed oppositely to dipoles inside DRs. These fields can be considered as originating from electric field lines circling around neighboring resonating dipoles and overlapping within the gaps. In narrow gaps, specific for MSs with lattice constant of 300 nm (dense MSs), fields in the gaps become enhanced up to the level of fields inside DRs. The strength of gap fields also increases at decreasing the DR heights in MSs, however this effect much weaker than the effect of decreasing the lattice constant. Observed enhancement of gap fields in MSs with lattice constant of 300 nm at h<160 nm allows for considering Y-sides of field grids as chains of oppositely directed dipoles. It is not excluded that such transformation of field patterns in dense MSs makes reflection from MSs at $f=f_{EDR}$ negligible and causes characteristic for them EIT-type full transmission at frequencies of EDRs. The grids with alternating resonance fields could be also the reason for observed at decreasing DR heights degeneration of BS drops at $f=f_{EDR}$ in spectra of MSs with lattice constant of 300 nm (Fig. 10). Analyzing comparable BS drops observed in spectra of MSs with lattice constants of 450 nm at $f>f_{EDR}$ (see section 4), we assumed that they could be related to another realization of Kerker's conditions of the 1st type for interference of radiation from two dipolar resonances. Alternatively oriented dipoles could affect realization of these conditions in MSs with lattice constant of 300 nm, due to destructive interference of radiation from dipoles and resonance fields in Y-gaps.

One more interesting effect can be seen at comparison of field distributions for MSs with lattice constants of 450 nm and 300 nm at h=110nm. In YZ cross-section of MS with lattice constant of 450 nm, it is well seen that centers of electric dipoles are shifted relatively centers of DRs, similarly to that observed in Fig. 5 for single DRs. Meanwhile, in MS with lattice constant of 300 nm, no similar shifting is detected, apparently, due to decreased freedom of resonance formation in MSs with closely packed neighboring resonators.

## 5.6 Conclusion

We have investigated the directivity and power density of radiation from MSs composed of cylindrical silicon resonators, organized in square lattices, with sparse and dense packing, in spectral ranges involving magnetic and electric dipolar resonances, and magnetic quadrupolar resonance. We changed the spectral positions of resonances by varying the DR heights, while keeping their diameters constant. Decreasing the heights of resonators allowed for moving both dipolar resonances to the blue edge of the spectra and for shifting the frequencies of MDRs closer to EDRs frequencies, up to their coincidence. Such coincidence is often considered in literature as a critical condition for obtaining full transmission through MSs with $2\pi$ phase control. In this work, we intended to get a deeper insight onto the phenomenon of scattering from silicon MSs. For comparison with S-parameter spectra, we obtained BS and FS spectra and far-field patterns characterizing radiation from MS fragments. In addition, to visualize spectral changes of BS and FS in dependence on DR geometry, we simulated 3D patterns, in which color changes were used to represent variation of scattered power density.

We compared characteristics of single spherical and cylindrical DRs, to identify in the latter the resonances analogous to dipolar and quadrupolar Mie resonances in spheres. It was found that, for sparsely packed MSs (with lattice constant of 450 nm), coincidence of dipolar resonances did not provide dominant FS or full transmission of incident waves. Analysis of S-parameter spectra and BS/FS spectra allowed for detecting the realization of 1st Kerker's conditions in the range $f< f_{MDR}$ at decreasing DR heights. In addition, an opportunity was found for realizing similar conditions at $f >f_{EDR}$. The drops in BS spectra were found entirely corresponding to the drops in S11 spectra that allowed for suggesting that they both were controlled by the impedance specifics. The studies of densely packed MSs (with lattice constant of 300 nm) revealed no effects characteristic for realizing Kerker's conditions of the 1st type at $f >f_{EDR}$. Instead, at DR heights below 160 nm, the S-parameter spectra of dense MSs demonstrated full transmission and no reflection at $f=f_{EDR}$. Responses of such type are not typical for conventional resonances. They could be explained by interference phenomena providing a kind of electromagnetically induced transparency in dense MSs. Analysis of field patterns in cross-sections of dense MSs allowed for relating the observed transparency to the specifics of field distributions in dense arrays, which could be interpreted as the sets of alternating dipoles.

Thus, although the possibility to observe full transmission through dense MSs has been confirmed, it did not look related to combined two π-value jumps in phase at EDR and MDR. Coincidence of dipolar resonances was not found to be productive for directional scattering. In particular, full transmission at $f= f_{EDR}$ could be obtained at distant positions of two dipolar resonances in spectra. Our data show that better directivity could be realized at $f <f_{MDR}$ at 1st Kerker's conditions. Confirmation of realizing the Kerker's effects in MSs composed of cylindrical silicon DRs with heights in the range from 240 nm down to 100 nm presents a valuable result of these studies. In addition, we have concluded that DRs in dense MSs do not respond as independent "meta-atoms" and that their responses become defined by integrated resonance fields.

# References


1. I. Staude, A.E. Miroshnichenko, M. Decker, N.T. Fofang, S. Liu, E. Gonzales, J. Dominguez, T.S. Luk, D.N. Neshev, I. Brener, and Y. Kivshar, “Tailoring directional scattering through magnetic and electric resonances in subwavelength silicon nanodisks,” ACS Nano, 7 (9), pp. 7824–7832, 2013.

2. B.S. Luk’yanchuk, N.V. Voshchinnikov, R. Paniagua-Domínguez, and A.I. Kuznetsov, “Optimum forward light scattering by spherical and spheroidal dielectric nanoparticles with high refractive index,” ACS Photonics, 2, 993–995, 2015.

3. Y.F. Yu, A.Y. Zhu, R. Paniagua-Domınguez, Y.H. Fu, B. Luk’yanchuk, and A.I. Kuznetsov, “High-transmission dielectric metasurface with 2π phase control at visible wavelengths,” Laser Photonics Rev., 9 (4), pp. 412–418, 2015.

4. A.I. Kuznetsov, A.E. Miroshnichenko, M.L. Brongersma, Y.S. Kivshar, B. Luk’yanchuk, “Optically resonant dielectric nanostructures,” Science, 354, 6314, 2016.

5. M. Kerker, D.-S. Wang, and C. L. Giles, “Electromagnetic scattering by magnetic spheres,” J. Opt. Soc. Am., 73, pp. 765–767, 1983.

6. W. Liu and Y. S. Kivshar, “Generalized Kerker effects in nanophotonics and meta-optics,” Optics Express, 26 (10), pp. 13085–13105, 2018.

7. J.M. Geffrin, B. García-Cámara, R. Gómez-Medina, P. Albella, L.S. Froufe-Pérez, C. Eyraud, A. Litman, R. Vaillon, F. González, M. Nieto-Vesperinas, J.J. Sáenz, and F. Moreno, “Magnetic and electric coherence in forward- and back-scattered electromagnetic waves by a single dielectric subwavelength sphere,” Nat. Commun. 3, 1171, 2012.

8. S. Person, M. Jain, Z. Lapin, J. J. S´aenz, G. Wicks, and L. Novotny, “Demonstration of Zero Optical Backscattering from Single Nanoparticles,” Nano Lett., 13, pp. 1806–1809, 2013.

9. Y.H. Fu, A.I. Kuznetsov, A.E. Miroshnichenko, Y.F. Yu, and B. Luk’yanchuk, “Directional visible light scattering by silicon nanoparticles,” Nat. Commun., 4, 1527, 2013.

10. M.I. Tribelsky, J-M. Geffrin, A. Litman, C. Eyraud, and F. Moreno, “Small dielectric spheres with high refractive index as new multifunctional elements for optical devices”, Sci. Rep. 5, 12288, 2015.

11. Z. Wang, N. An, F. Shen, H. Zhou, Y. Sun, Zh. Jiang, Y. Han, Y. Li, and Z. Guo, “Enhanced forward scattering of ellipsoidal dielectric nanoparticles,” Nanoscale Research Lett., 12 (1):58, 2017.

12. E. Semouchkina, G.B. Semouchkin, M. Lanagan, and C.A. Randall, “FDTD study of resonance processes in metamaterials,” IEEE Transactions on Microwave Theory and Techniques, 53 (4), pp. 1477-1487, 2005.

13. M.S. Wheeler, J.S. Aitchison, and M. Mojahedi, “Coupled magnetic dipole resonances in sub-wavelength dielectric particle clusters,” J. Opt. Soc. Am. B, 27, 1083, 2010.

14. N. Liu and H. Giessen, “Coupling effects in optical metamaterials”, Angew. Chem., Int. Ed. Engl. 49 9838, 2010.

15. F. Zhang, L. Kang, Q. Zhao, J. Zhou and D. Lippens, “Magnetic and electric coupling effects of dielectric metamaterial,” New Journal of Physics, 14, 033031, 2012.

16. N. Gandji, G. Semouchkin, and E. Semouchkina, “Electromagnetic responses from planar arrays of dielectric nano-disks at overlapping dipolar resonances,” IEEE Conference on Research and Applications of Photonics in Defense (RAPID), 2018.

17. I. Staude, and J. Schilling, “Metamaterial-inspired silicon nanophotonics”, Nature Photonics, 11, pp. 274–284, 2017.

18. E. Semouchkina, Resonance Field Analysis and Electromagnetic Coupling Effects in Metamaterials Structures, book Chapter in “Metamaterials: Classes, Properties and Applications,” ISBN: 978-1-61668-958-2, Nova Science Publishers, pp.137-164, 2011.

19. S. Jamilan, G. Semouchkin, N. P. Gandji, and E. Semouchkina, “Specifics of scattering and radiation from sparse and dense dielectric meta-surfaces,” Journal of Applied Physics, 125 (16), 163106, 2019.

# 6 Lattice Resonances in Metasurfaces Composed of Silicon Nano-Cylinders[6]

## 6.1 Introduction

Silicon metasurfaces (MSs) demonstrate unique capabilities for controlling light propagation and scattering at the formation of Mie resonances in constituent posts or disks. The properties of MSs can be employed for realizing various photonic functionalities in sensing, imaging, light-guiding, and holographic applications [1-5]. Originally, plasmonic MSs have been developed and utilized for these purposes [2]. However, employing metal in their design caused excessive losses in optical range. Alternative MSs, composed of dielectric resonators (DRs), were found free from similar drawbacks that had opened a window for implementing efficient optical components and led to advances in photonics [1]. However, recent works on the resonance phenomena in dielectric MSs have revealed that in addition to elementary resonances, such as electric and magnetic dipolar and quadrupolar resonances (EDR, MDR, and MQR) in constituent particles, MSs are capable of supporting complicated resonance phenomena, which integrate the entire lattice due to the propagation of surface waves [3-5]. The studies of the effects of lattice periodicity on these phenomena have shown that at lattice constants, comparable to the wavelengths of radiation, diffraction of surface waves, which are initiated by elementary electric and magnetic resonances, leads to appearance of so-called lattice resonances (LRs), which significantly affect MS responses [4, 5]. Realization of LRs opens up new perspectives for developing various applications demanding field-localization or high-Q resonances [5]. This work aims to provide a deeper insight into the formation and the effects of LRs in silicon MSs. Special attention is paid to the realization of the Kerker's effects.

## 6.2 Results and Discussion

MSs under study had square lattices and were composed of silicon nano-posts with the diameters of 240 nm and with variable heights. Unit-cells of MSs with periodic boundary conditions were simulated by using COMSOL Multiphysics software package. Electric and magnetic components of the incident wave were polarized, respectively, along X and Y axes, while Z-directed wave-vector was normal to the plane of lattice. Fig. 1 presents spectral changes of MS responses at increasing the lattice constants $\Delta$. It is seen in the figure that both electric and magnetic resonance responses, registered by the probes, located in DRs' centers, demonstrate red spectral shifts in MSs with bigger $\Delta$. As the result, the curves, representing dependences of resonance positions on $\Delta$, turn towards longer wavelengths and gradually approach the lines, corresponding to Rayleigh anomalies (RAs), which play the role of asymptotes for respective dependencies. Similar effects were earlier noticed in [4] at studying planar arrays of spherical silicon resonators, organized in

[6]Reprinted from 'S. Jamilan and E. Semouchkina, "Lattice Resonances in Metasurfaces Composed of Silicon Nano-Cylinders," 14th International Congress on Artificial Materials for Novel Wave Phenomena - Metamaterials, New York, USA, Sept. 28th – Oct. 3rd, 2020'; with permission from © IEEE Publishing.

rectangular cells. Authors of [4] related the obtained data to an interplay of elementary dipolar resonances with surface lattice resonances. However, presented below data do not confirm integrating of these resonances. As seen from the presented in Fig. 1 S-parameter spectra, red shifting of electric responses creates an opportunity for realizing both electric and magnetic responses at the same wavelengths of incident light. However, at an obvious presence of LRs in MSs, such overlapping does not lead to realizing any special effects in MS transmission or reflection spectra. It should be noted that LRs, formed by surface waves, propagating in MS plane, are not expected to directly affect transmission of waves at normal incidence**.** Kerker's effect, caused by interference of EDR and MDR radiations, is well seen as deep drops in the presented S11 spectra at wavelengths, exceeding the resonance wavelengths (see dark-blue line to the right from MDRs in Fig. 1).

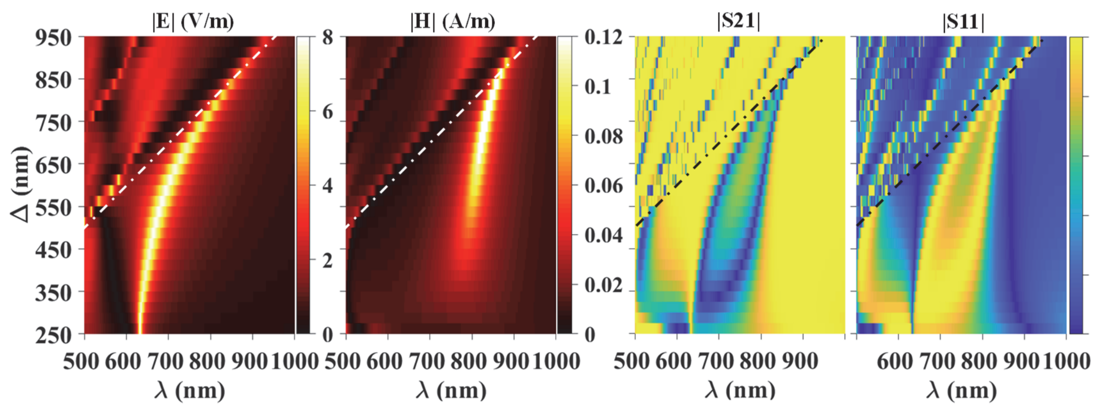


Fig. 1. Red shifting of electric and magnetic resonance responses of square-latticed MSs at increasing their lattice constants and representation of resonance responses by color images of S-parameter spectra. The heights of silicon posts were 160 nm. Positions of Rayleigh anomalies are shown by dashed-dotted lines.

According to [4], LRs gain their strength in spectral regions close to the RA lines. Thus, the data presented in Fig. 1 could be used to determine the range of lattice constants, at which clear signs of LR appearance could be expected in field distributions of MSs. Considering the electric lattice resonance, it can be concluded from Fig. 1 that the presence of LRs should be expected in E-field distributions of MSs with lattice constants in the range from 450 nm to 750 nm. These distributions in planar (XY) and normal to the MS plane (ZX) and (ZY) cross-sections are presented in Fig. 2.

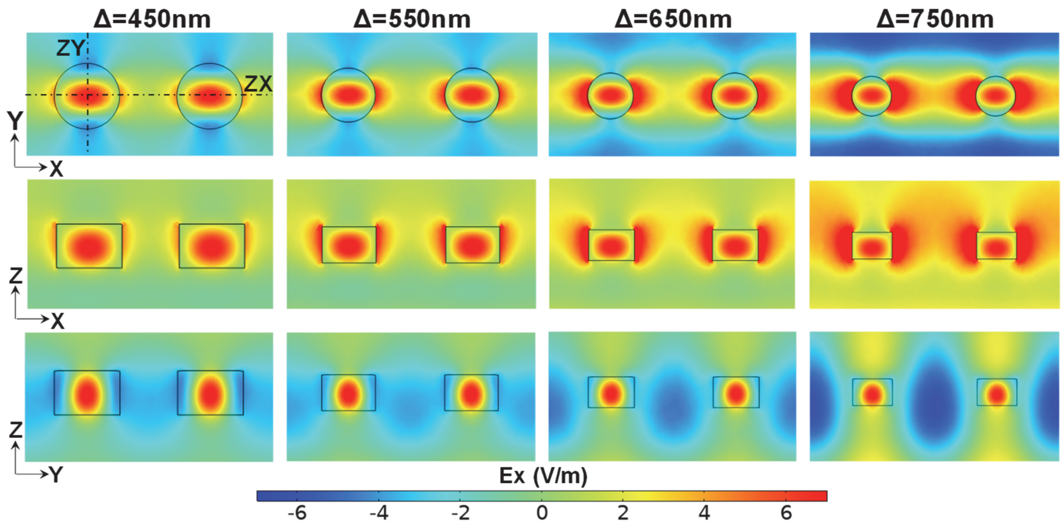


Fig. 2. Changes of gap-edge field configurations at increasing the lattice constants Δ in square-latticed MSs, composed of DRs with the heights of 160 nm and diameters of 240 nm. Field patterns in three rows were obtained, respectively, in XY, XZ and YZ cross-sections passing through DR centers. Z-axis is normal to MS plane, X- and Y- axes are co-directed with E- and H-fields of incident waves. Dashed lines show positions of ZX and ZY cross-sections.

As seen in the figure, at Δ = 450 nm, strong fields can be observed in the centers of MS resonators in all three cross-sections. The distributions of these fields correspond to the formation of the electric dipolar resonances in DRs. However, at Δ = 550 nm, the field patterns change. In addition to dipolar fields, an appearance of field spots in X-oriented gaps between resonators can be observed. These field spots look adjacent to the resonator bodies and having maximal intensity at outer surfaces of resonators. They are called further the gap-edge fields. These fields spread in air in both Z and X directions and do not look as an extension of the dipolar fields. At bigger Δ, they become much stronger, than dipolar fields inside resonators, the intensity of which does not experience visual changes. It is worth mentioning that gap-edge fields, formed at two sides of resonators, do not overlap, and therefore, can be considered as independent entities. On the other hand, the field patterns in ZY cross-section allow for suggesting that the gap-edge fields in X-oriented gaps affect the fields in Y-oriented gaps between resonators. While at Δ = 450 nm, the fields in Y-oriented gaps have relatively low intensity, being defined by dipolar fields, circling in air around resonators, then at bigger Δ, the intensity of Y-gap fields experiences a significant enhancement correlated with an enhancement of gap-edge fields in X-oriented gaps. The mechanism of this correlation has to be investigated additionally.

To ensure that the gap-edge fields can serve as the markers of LRs, the spectra of E-field signals from probes placed in special points of MSs have been simulated. As evident from the schematic in Fig. 3, P1 probe characterizes the dipolar resonance formation, P2 probe represents incident wave field within MS, and P3 probe provides information about the formation of gap-edge fields. From the data in Fig. 3 it is well seen that the peak intensity of the dipolar resonance in point P1 experiences no changes at increasing Δ, despite red shifting of the spectral positions of peaks. Intensity of background radiation (point P2) becomes less at bigger Δ, as it is expected, while the strength of the gap-edge fields in point P3 grows up significantly, so that its dual peaking even exceeds the resonance peak in point P1. Spectral positions of P3 peaks coincide with positions of electric and magnetic dipolar resonances that agrees with the suggestion that LRs are caused by the diffraction of surface waves, launched by resonance radiation.

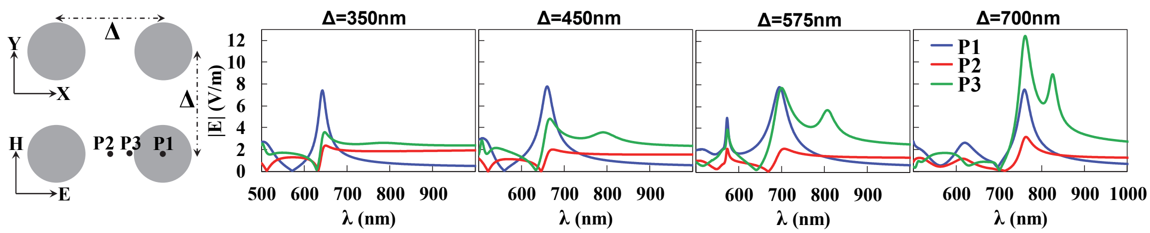


Fig. 3. Schematic of probe location and spectra of signals from respective E-field probes placed at points P1, P2, and P3 of square-latticed MSs having different lattice constants Δ. Resonator heights were 160 nm and diameters - 240 nm.

## 6.3 Conclusive Remarks

According to the obtained results, resonances inside DRs conserve their strength at the conditions, which cause strong enhancement of LRs. Thus, the formation of LRs does not inevitably affect dipolar resonances inside DRs. It could be then presumed that surface waves, responsible for the formation of LRs, do not interact with DRs in the same manner, as the plane waves, incident normally to the MS plane. Under such assumption, the formation of elementary resonances inside DRs, on one hand, and the formation of gap-edge fields, as LR markers, on the other hand, should be controlled by physically different processes. At the same time, surface waves should experience scattering at their interaction with DRs, located on their path, even though this scattering could not affect the strength of resonance fields inside DRs. Scattered fields are, most probably, collected in the spots of gap-edge fields near the centers of scattering, i.e. DRs. However, the physics underlying appearance of resonance-like field enhancements in these spots still needs clarification. Additional question, which requires further clarification, is the nature of red shifting of the resonance responses at increasing the lattice constants. Since this shifting proceeds without changing the strength of resonance fields in DR centers, it should be related to some geometric factors. In particular, it could be suggested that shifting of electric responses to longer wavelengths could be defined by coherent oscillations of dipolar fields, formed inside DRs, and gap-edge fields, formed in X-oriented gaps. Such coherence could increase the effective wavelengths of oscillations controlling the formation of resonances in the centers of DRs.

# References


1. A.I. Kuznetsov, et. al., “Optically resonant dielectric nanostructures,” Science, vol. 354, no. 6314, pp. 2472, Nov. 2016.

2. D. Khlopin, et. al., “Lattice modes and plasmonic linewidth engineering in gold and aluminum nanoparticle arrays,” Journal Opt. Society of America B, vol. 34, no. 3, 2017.

3. S. Jamilan, G. Semouchkin, N.P. Gandji, and E. Semouchkina, “Specifics of scattering and radiation from sparse and dense dielectric meta-surfaces,” J. Appl. Phys., vol. 125, p. 163106, 2019.

4. V.E. Babicheva and A.B. Evlyukhin, “Resonant lattice Kerker effect in metasurfaces with electric and magnetic optical responses,” Laser & Photonics Reviews, vol. 11, p. 1700132, 2017.

5. X. Wang, L.C. Kogos, and R. Paella, “Giant distributed optical-field enhancements from Mie-resonant lattice surface modes in dielectric metasurfaces,” OSA Continuum, vol. 2, no. 1, pp. 32-42, 2019.

6. S. Jamilan and E. Semouchkina, “Lattice resonances in metasurfaces composed of silicon nano-cylinders,” 14th International Congress on Artificial Materials for Novel Wave Phenomena - Metamaterials, New York, USA, Sept. 28th – Oct. 3rd, 2020.

# 7 Analog of Electromagnetically Induced Transparency in Metasurfaces Composed of Identical Dielectric Disks[7]

## 7.1 Introduction

The phenomenon of induced transparency of otherwise opaque medium was initially revealed in atomic gases, where it was named "electromagnetically induced transparency" (EIT) and was considered as defined by destructive quantum interference between competing electron transitions, which led to appearance of a narrowband window for the trespassing light [1-3]. Later, similar window openings at wavelengths far longer than those in atomic gases were observed in arrays of metallic meandered wires [4], coupled plasmonic resonators [5], as well as in metamaterials and metasurfaces (MSs), composed of specially designed resonators including dielectric ones [6-10]. All these structures were found capable of supporting full propagation of incident electromagnetic waves within a narrow band, while at lower or higher frequencies, waves were either completely reflected or absorbed. The fact that phenomenologically similar results were obtained in quite different substances did not seem surprising, since it was shown in [11] that basic characteristics of EIT-like phenomena in quantum gases could be modelled by using classical systems of coupled harmonic oscillators (coupled RLC circuits in electrical model or properly connected particles and springs in mechanical model).

In difference from the referenced above works on metamaterials and MSs composed of resonators with complex configuration, we observed narrow-band transparency at electric dipolar resonances in densely packed MSs formed from simple silicon resonators of cylindrical or disk shapes [12, 13]. At such MS geometry, the concept of interfering bright and dark modes in coupled resonators, which was conventionally used for explaining EIT-like phenomena in multi-resonator arrays, could not be applied. In this work, we present the results of investigations, which allow for forwarding an alternative concept, clarifying the reasons for induced transparency of MSs composed of identical disk resonators. In particular, we pay special attention to Fano-type resonances in MSs under study. These resonances, as known, are the product of interference between competing wave processes [6, 14, 15]. A deeper insight into the formation of Fano resonances in MSs allows us to understand wave processes, which define the appearance of EIT-type phenomenon in MSs under study.

It should be noted here that employing the EIT phenomena promises significant advances in optical information processing. In particular, opening a narrowband transparency window at EIT was found to result in dramatic reduction of the light group velocity, i.e. in

---

[7]Reprinted from 'S. Jamilan, G. Semouchkin, and E. Semouchkina, "Analog of Electromagnetically Induced Transparency in Metasurfaces Composed of Identical Dielectric Disks," Journal of Applied Physics, 129 (6), 063101, 2021'; with permission from © AIP Publishing.

slow light [16], enabling even complete stop of the propagating optical pulse and its storage in the atomic ensembles [17]. Similar stop was observed in waveguides, side-coupled to tunable resonators, when a photonic band structure representing a classical analogue of EIT was generated [18]. Slow light was also used in optical networks for implementing optical buffers [19]. Tunable optical buffers were recently developed by using an analogue of EIT in coupled photonic crystal cavities [20]. In [21], the EIT was used to build optical switches and wavelength converters. In [22], it was proposed to design switches and filters by using switchable EIT phenomenon in graphene-loaded MSs composed of split silicon nano-cuboids. Thus, it is expected that realizing EIT in very simple MSs will open up additional perspectives for various applications

## 7.2 Model and Methods Description

Fig. 1 presents the schematic of MS fragment, used in our studies. The structures were composed of silicon cylinders or disks with the diameters (D) of 240 nm and heights (h) varied from 100 nm to 240 nm. These cylinders/disks are further called "dielectric resonators" (DRs). Parameters of resonators were chosen to provide comparison of obtained results with the results of our earlier studies [12, 23, 24], as well as with the data, presented in well-known works on silicon MSs [25, 26]. Lattice parameters (Δ) of MSs under study were varied in the range from 275 nm to 450 nm. At smaller Δ, the structures were considered as densely packed, since the distances between DRs in such structures could be equal to 35 nm, that was much smaller than the diameters of silicon particles, while at larger Δ, the structures were considered as rather sparsely packed, since the distances between DRs approached 210 nm, i.e. became compared to the diameters of DRs. The terms "dense" and "sparse" were introduced earlier in [12, 23, 24], to stress out significant differences in responses of MS structures with different Δ.

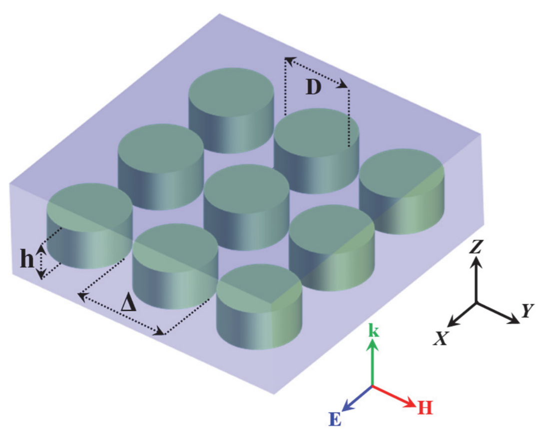


FIG 1. Schematic of MS composed of silicon nano-disks.

The studies were conducted for MSs with square and rectangular lattices. To verify the results of numerical experiments, we compared the data obtained by using two types of commercial software: COMSOL Multiphysics and CST Microwave Studio. As seen in Fig. 1, incident waves were sent normally to MS planes with electric (E) and magnetic (H) field vectors, directed along X- and Y-axes, respectively. The amplitude of incident wave's electric component was always fixed at 1 V/m. Field data and scattering parameters (S-parameters) were directly extracted from the results of simulations. In simulation models, DRs were placed in air that allowed for investigating the basic physics of MS performance without complications arising from substrate involvement. It is, however, shown in section III that inserting substrates did not deteriorate observed EIT-type effects.

As it was demonstrated in our earlier work [24], all characteristic features of MS responses could be conserved, when the structures with nano-sized particles, used in the optical range, are rescaled for operating in the microwave range, where experimental studies are much easier to perform. Therefore, in this work, experiments were performed at microwave frequencies with MSs, composed of ceramic mm- size resonators. Parameters of resonators and MSs were chosen to provide scaling of the phenomenon of induced transparency from optical to microwave range. Experimental technique is described in section IV.

## 7.3 Detecting the Transparency of Densely Packed MSs

The phenomenon of induced transparency in densely packed MSs with square lattices, composed of cylindrical silicon resonators, was first noticed in [12] at the studies of MS resonance responses in dependence on DR heights. In these studies, the lattice constant of MSs was kept on the level of 300 nm, while changes of MS responses were provided by varying the heights of constituent resonators in the range from 200 nm to 100 nm. In particular, the spectra of electric (E) and magnetic (H) field probe signals and transmission spectra S21 were investigated. The effects, reminding the EIT phenomenon, were detected in the spectra of S-parameters, which demonstrated sharp peaks of S21 up to 1 and narrow-band drops of S11 down to zero at the frequencies of electric dipolar resonances (EDRs).

Fig. 2 demonstrates EIT-like responses, simulated by using either COMSOL or CST software, for MSs with DRs placed either in air or on the PDMS substrate with relative permittivity of 2.25 and thickness of 200 nm. The observed in S-parameter spectra narrow transparency window is surprising, since the formation of Mie resonances in dielectric MSs is usually associated with spectral regions of high reflections.

Fig. 3 presents S-parameters spectra of MSs with square lattices and the spectra of E- and H-probe signals, obtained at placing the probes in the centers of DRs, at different lattice constants of MSs. Since the properties of MSs could be also modified by changing the DR heights, Fig. 3 allows for comparing the data, obtained for MSs with DRs heights of 160 nm and 130 nm.

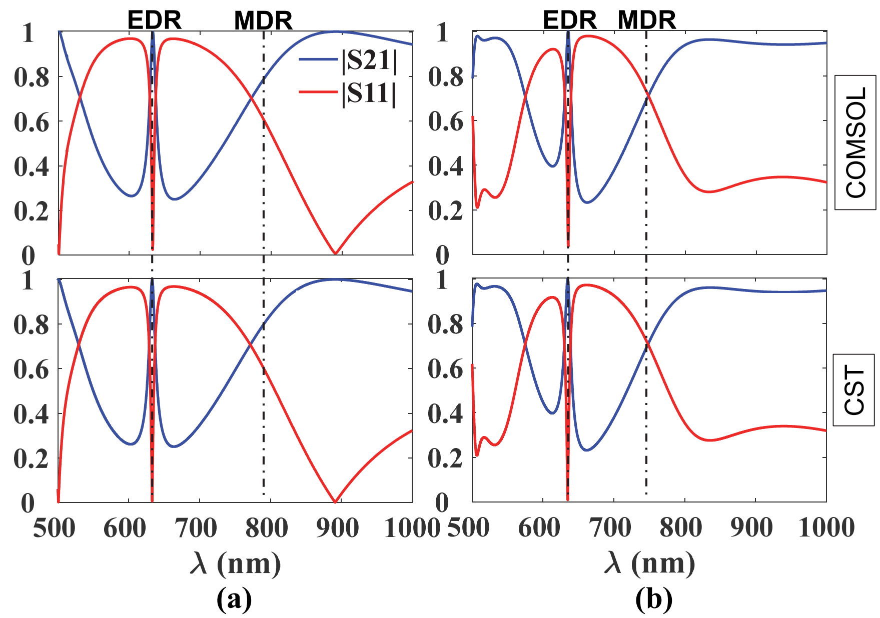


FIG 2. S-parameters spectra for MSs with square lattices and lattice constants of 275 nm, simulated by using COMSOL (upper row) and CST (lower row) software. Heights of silicon disks were 160 nm, while they were placed in (a) air and (b) on the PDMS substrate with thickness of 200 nm. Diameters of DRs were 240 nm. Spectral positions of EDRs and magnetic dipolar resonances (MDRs) are indicated by vertical dashed-dot lines.

As seen in the figure, S-parameter spectra in most dense MSs (at $\Delta < 300$ nm) exhibit the features, which are very common for multiple demonstrations of EIT in literature [4-10]. In particular, narrowband peaks of S21, combined with sharp dips of S11, are seen in the surrounding of gradually varying parts of two spectra, which are less or more symmetric with respect to EIT windows. For MSs with $\Delta < 325$ nm, no other singularities of S parameters could be found in spectral regions near EDRs, i.e. nothing disturbed the opaque property of MSs, except for peaks of S21 at deep drops of S11 at EDR frequencies.

Most symmetric with respect to EDRs EIT-type responses were observed in MSs with h = 160 nm at the lattice constant $\Delta = 275$ nm and in MSs with h = 130 nm at the lattice constant $\Delta = 300$ nm. At increasing $\Delta$, combined S21 peaks and S11 dips continued to be seen in S-parameter spectra of MSs at all values of $\Delta$ up to 400 nm. However, the symmetry of S-parameter spectra on the blue and red sides of the EIT-type singularity disappeared for the case h=160 nm at $\Delta > 300$ nm. Gradually, the two spectra, S21 and S11, became anti-symmetric in the EIT area. In particular, in addition to initial peaks of S21, accompanied by S11 dips, a wide ridge of close to unity S11 values, accompanied by dips of S21, appeared at slightly longer wavelengths. At $\Delta = 325$ nm and above, two spectra crossed each other at wavelengths between the spectral locations of their extrema. As known, similar crossings were noticed in S-parameter spectra of dipole antennas (when |S21| = |S11| = 0.7). At lattice constants of about 450 nm, sharp S21 peaks could not be seen anymore, but the tops of wide S21 ridges, formed instead of peaks, still approached the unity value at some wavelength λ, smaller than $\lambda_{EDR}$, while S11 continued to demonstrate dips down to zero. It is worth noting here that the described above changes occurred along with the appearance of deep depression of S21 on the red side of EIT-type window at Δ > 300 nm (that is especially well seen in Fig. 3 (a)). At further increasing Δ, this depression transformed into dual dips of S21, usually associated in sparse structures with two dipolar resonances (electric and magnetic ones), which were expected to cause zero transmission at total reflection. However, such direct association is not obvious from the data presented in Fig. 3, especially for magnetic resonance, since it appeared in probe signal spectra at longer wavelengths, than wavelengths of red-side S21 dips. Positions of S21 dips, located at shorter wavelengths, experienced relatively small spectral changes at increasing the Δ values, but at bigger Δ, they approached the positions of electric resonances, since the latter shifted to the red side of the spectra. Altogether, the described changes, observed at increasing Δ, transformed S-parameter spectra into configurations, which were characteristic for sparse MSs [12].

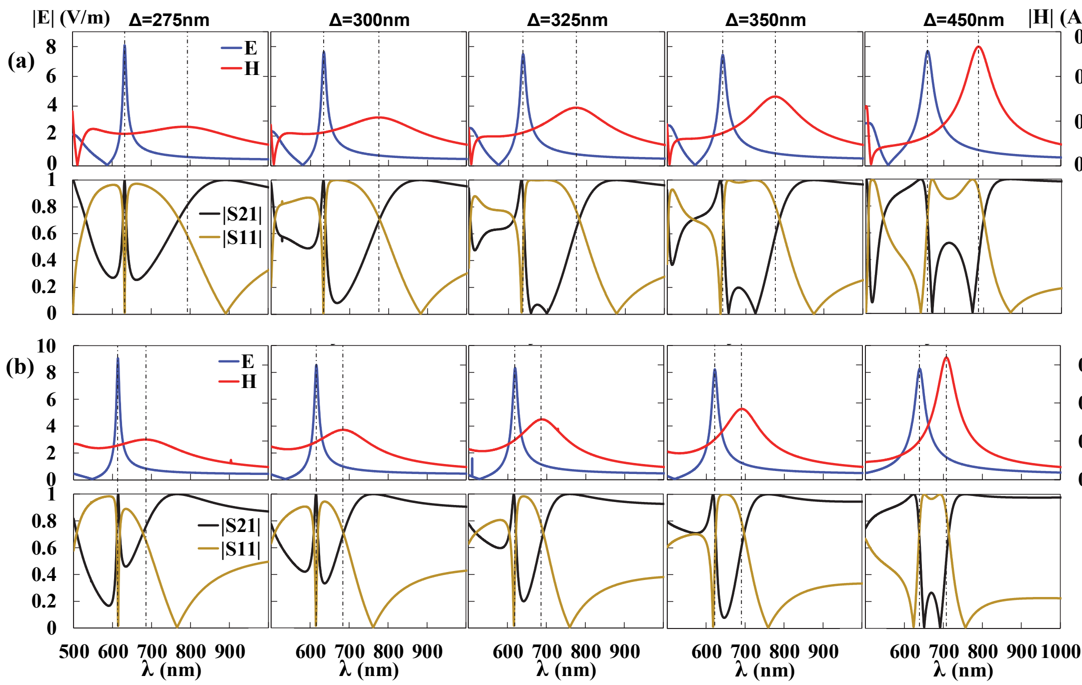


FIG 3. E- and H-field probe signal spectra and S-parameters spectra at various lattice constants of silicon MSs with square lattices, having different heights of constituent resonators: (a) 160 nm and (b) 130 nm. Diameters of resonators are 240 nm.

From the comparison of sets (a) and (b) in Fig. 3, it could be noticed that decreasing DR heights allows for shifting EIT window to shorter wavelengths, as well as for increasing the range of lattice constants, at which typical for EIT features of S-parameter spectra could be observed. However, at Δ = 450 nm, the spectra of MSs with DRs of different heights acquired similar shapes.

It is also seen in Fig. 3 that at wavelengths longer than those, corresponding to positions of red-side dips in S21 spectra and positions of MDRs in probe signal spectra, S-parameter spectra of MSs demonstrate one more singularity, i.e. regions with full transmission (|S21| = 1) and sharp drops of reflection coefficient S11 down to zero. This phenomenon is characteristic for the Kerker's effect, which is observed at interference between waves, radiated by oscillating fields of electric and magnetic resonances in MS particles. The results of our studies of this effect in MSs, composed of silicon nano-disks, were presented in our earlier work [12].

Fig. 4 provides color-scaled (3D) representations of the discussed above transformations of S-parameters spectra at increasing the lattice constants, which help to understand the factors, restricting the realization of induced transparency in MSs composed of silicon disks. It is well seen in the figure that in dense structures with $\Delta < 325$ nm, the EIT-like phenomenon reveals itself in S21 spectra as a spectrally narrow strip of red color, which corresponds to full transmission (|S21| = 1). In S11 spectra, induced transparency causes appearance of a narrow strip of dark-blue color, which corresponds to zero reflection (|S11| = 0). At increasing the $\Delta$ values, both strips become wider. However, the EIT-related strip in the image of S21 spectra becomes several times wider, when $\Delta$ changes from 325 nm to 375 nm, while similar strip in the image of S11 spectra remains relatively narrow at increasing $\Delta$ up to 450 nm.

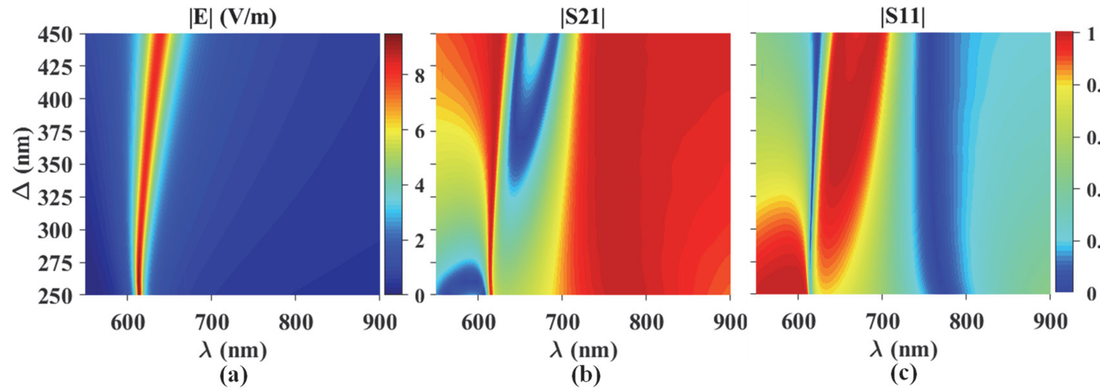


FIG 4. Effects of MS periodicity on (a) spectral positions of EDRs and on colour-scaled images of (b) S21 and (c) S11 spectra. DR heights in all MSs were kept equal to 130 nm, diameters of DR were 240 nm.

Fig. 4 also visualizes the deterioration of the symmetry of S-parameter spectra at bigger lattice constants. As seen in the image of S21 spectra, the EIT-related strip crosses identically colored light blue areas only at $\Delta < 325$ nm, while at bigger $\Delta$, the colors on two sides of the strip become contrast: red color marks close to unity values of S21, while blue color marks close to zero values of S21 that excludes any symmetry. The EIT-related strip in the image of S11 spectra passes between two identically colored red areas (with |S11| = 1) only at $\Delta < 325$ nm, while at bigger $\Delta$, the area to the left from the strip becomes colored light blue, while the area to the right turns to become dark red (with |S11| = 1) that also excludes any symmetry in S11 spectra.

In addition to deteriorating the symmetry of S-parameter spectra at increasing the array lattice constant, there is another reason, which restricts realizing EIT-type effects in sparse MSs. As it is seen from the presented data, the Q-factors of observed phenomena in MSs with bigger lattice constants look significantly decreased. In literature related to the EIT phenomenon, high Q-factors are considered as an important benefit, degrading of which can create problems for obtaining practically important slow-light effects. Therefore, it was desirable to look for opportunities to increase the range of options for realizing narrow band of EIT in MSs. For this purpose, we investigated the EIT-type phenomena in MSs with rectangular lattices. In these studies, we fixed the "dense" value of Δ (275 nm) in either X- or Y-direction, while varied the Δ value for another direction in wide range.

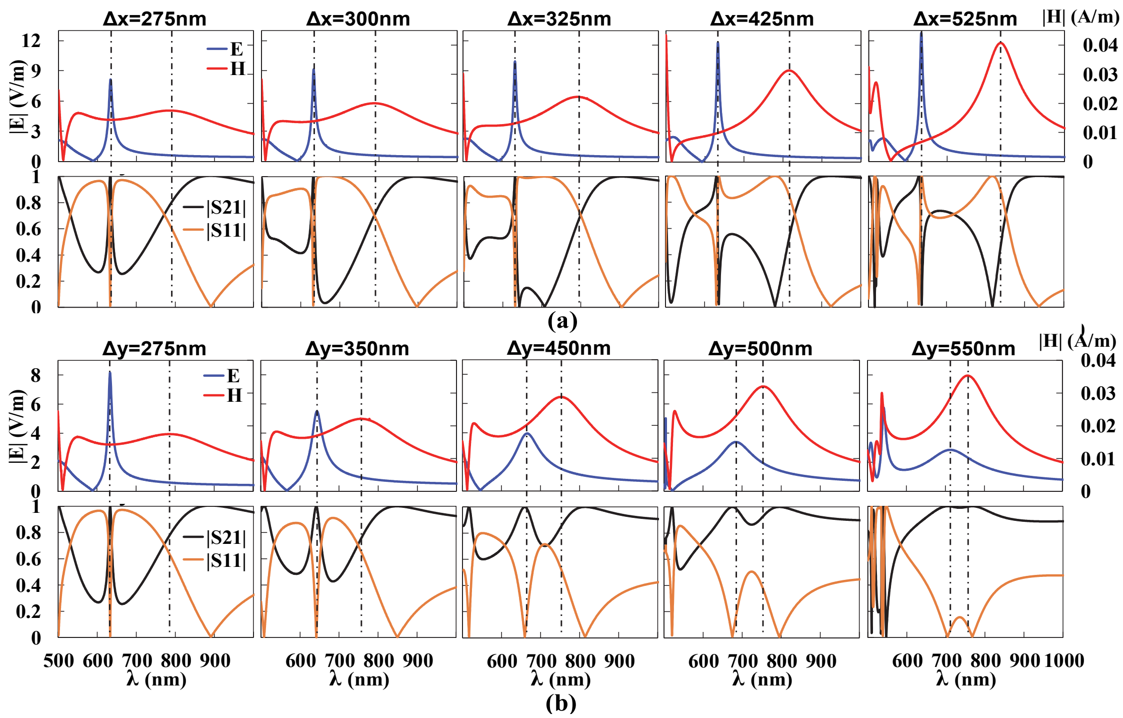


FIG 5. Transformations of E- and H-field probe signal spectra and S-parameters spectra at modifying MSs by extending their unit cells: (a) along X-axis at fixed Δy = 275 nm, and (b) along Y-axis at fixed Δx = 275 nm. Vertical dashed-dotted lines show spectral positions of EDRs and MDRs. DR heights in all MSs are 160 nm, while DR diameters are 240 nm.

Fig. 5 (a) shows, how S-parameters spectra change at extending lattice cells of MSs in X-direction, while Δy value is fixed. As seen in the figure, these changes have a lot in common with changes observed in Fig. 3 (a) for MSs with square lattices. In particular, there is similar difference in the changes of S-parameters in blue and red parts of the spectra around the EIT singularity, and similar appearance of anti-symmetric line-shapes in S21 and S11 spectra, with their crossings at close to EDR wavelengths at bigger Δ. The only difference of the case with rectangular lattices versus the case with square lattices is seen in very sharp, almost vertical, drops of S11 near EDRs and in conserved peaking of S21 curves at EDRs even at Δy = 525 nm. The similarity of the basic features of the data presented in Figs. 3 (a) and 5 (a) (both sets were obtained at DR heights of 160 nm) implies that these features are controlled by changing the Δx values, regardless of whether these changes are accompanied by similar changes of Δy, or Δy remains fixed at the value of 275 nm.

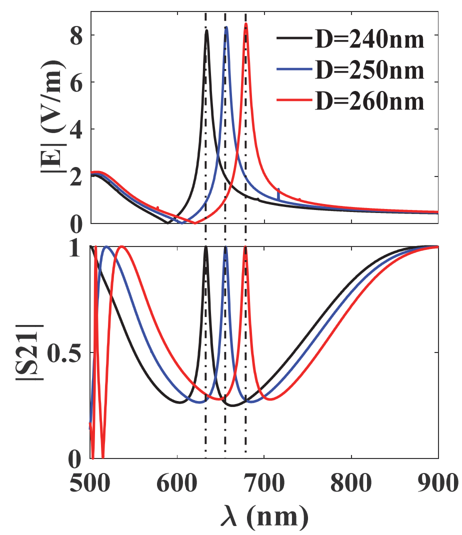


FIG 6. Simulated responses of dense MSs composed of silicon disks with identical heights of 160 nm and various diameters. DR diameters are, respectively, 240, 250, and 260 nm, and lattice constants of respective MSs are 275, 287, and 301 nm, respectively.

However, extending lattice cells of MSs in Y-direction at keeping Δx fixed at the level, characteristic for dense structures, does not produce changes in S-parameters spectra, comparable to those, observed at extending lattice cells in X-direction. As seen in Fig. 5 (b), S-parameters spectra conserve such characteristic features of EIT, as full transmission and zero reflections at EDR wavelengths, at increasing Δy up to 450 nm and even bigger values. However, the line-shapes of S11 and S21 spectra degrade at increasing Δy, in comparison with the line-shapes observed for MSs with square lattices at Δ = 275 nm. In particular, the peaks and dips of S-parameters become essentially less sharp and are characterized by much smaller Q-factors, compared to narrowband EIT-like singularities. At Δy = 500 nm and bigger, EDRs reveal themselves in S-parameter spectra by wide dips of S11 down to zero, comparable to dips observed at the Kerker's conditions, and by hill-like patterns of S21 spectra at the frequencies of EDRs. It is also worth noting that increasing Δy practically does not change spectral positions of MDRs, while the positions of EDRs demonstrate red shifts, thus bringing two resonances closer to each other. The specifics of changes in S-parameter spectra at extending lattice cells in Y-direction allows for suggesting that, in difference from extending the cells in X-direction, such lattice transformation does not deteriorate physical processes, responsible for the EIT phenomenon, while provides more options for its realization. It is worth noting that significant red shifting of EDR's spectral positions at $\Delta y > 450$ nm is apparently caused by the formation of lattice resonances, when $\Delta y$ approaches the values corresponding to appearance of Rayleigh anomalies [27]. This shift, however, does not occur in densely packed MSs.

EIT wavelength could be changed by changing EDR frequency at varying aspect ratio of DRs. In Figs. 3 (a) and (b), heights of disks were changed, while their diameters were fixed equal to 240 nm. Fig. 6 shows that an increase of DR diameters from 240 nm up to 260 nm, if DR heights are fixed equal to 160 nm and lattice constants $\Delta$ are properly adjusted, leads to red shifting EIT wavelengths. This could be used for adjusting spectral position of EIT window in dense MSs composed of identical dielectric disks.

## 7.4 Scaling MSs and Experimental Confirmation of Induced Transparency in Microwave Range

To scale MSs for performing microwave experiments, we followed the approach used in [24]. Similar to optical nano-resonators, microwave resonators were initially supposed to have relative permittivity of 12.25. Resonators were represented by disks with the diameters of 6 mm and the heights of 3.5 mm. To provide desirable MS responses, lattice constants were chosen in the range from 6.5 mm to 12 mm. As seen in Fig. 7, using the above listed parameters allowed for reproducing in S-parameter spectra of "microwave" MSs all details, characteristic for S-parameter spectra of MSs, composed of nano-resonators.

As seen in the figure, the EIT-type peak of S21 parameter, combined with the dip down to zero of S11 parameter, was obtained for microwave MS at the frequency of electric dipolar resonance. Similar to the case of optical MSs, this singularity in S-parameter spectra of microwave MSs was accompanied by the enhancement of reflections on both sides of S21 peak that allowed for describing the phenomenon as appearance of a narrow-band transparency window for incident waves in otherwise opaque medium. Similar to optical case, S-parameter spectra of microwave MS demonstrated crossing of S21 and S11 spectra at the frequency, close to the frequency of magnetic dipolar resonance, and also the features, characteristic for the Kerker's effect (at f = 20 GHz) [12, 24].

Since the frequency, corresponding to the S21 peak in the spectrum of microwave MS appeared to be higher, than that convenient for experiments, the permittivity of DRs had to be increased. The results of simulations, presented in Fig. 8, show, how the frequency range, necessary for the observation of induced transparency in microwave MSs, changes at varying the values of dielectric permittivity of the resonator material.

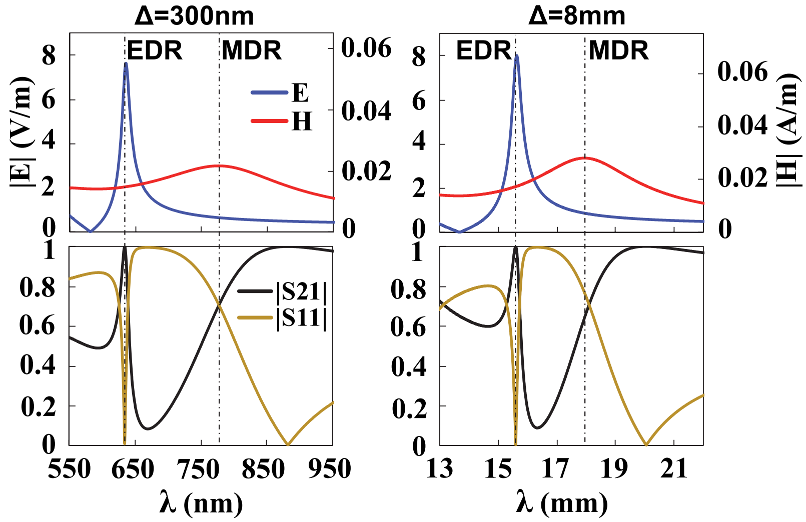


FIG 7. Upper row: simulated E- and H-field signals from probes located in centers of MS resonators. Lower row: simulated S-parameter spectra of MSs. Left column: optical MSs with lattice constant of 300 nm, composed of DRs with h = 160 nm, D = 240 nm, ε = 12.25. Right column: microwave MSs with lattice constant of 8 mm, composed of DRs with h = 3.5 mm, D = 6 mm, ε = 12.25.

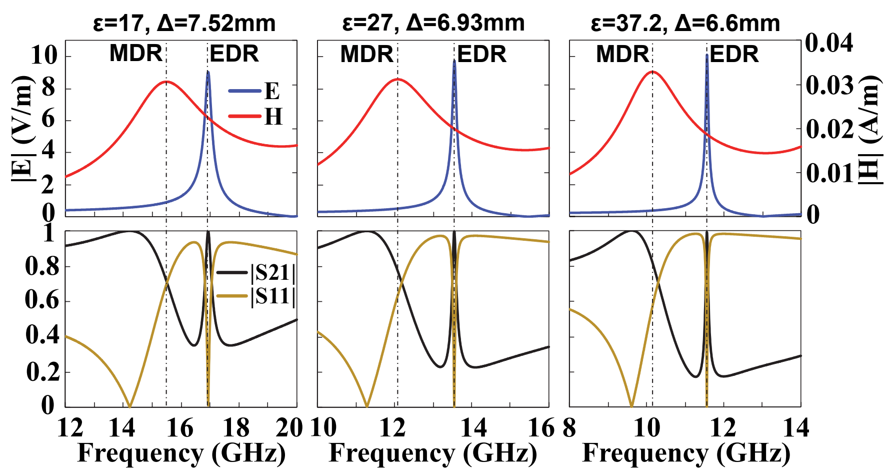


FIG 8. Upper row: simulated E- and H-field signals from probes located in centers of MS resonators. Lower row: simulated S-parameter spectra for densely packed MSs, composed of DRs with h = 3 mm D = 6 mm. The relative permittivity of DRs in three MSs, from left to right, is equal to 17, 27, and 37.2, respectively.

As seen in Fig. 8, the desired frequency range, centered around 11 GHz, is achievable in MSs, composed of resonators with the relative permittivity close to 40, instead of 12.25. Presented in Fig. 8 data also show that increasing the permittivity of dielectric material improves the shape of the singularity, representing the induced transparency, i.e. the Q factor of related S21 peak. In addition, MSs' responses on both sides of the singularity demonstrate strongly opaque properties of the medium. Based on the obtained data, arrays of ceramic resonators with the diameters and heights of, respectively, 6 mm and 3 mm, and the relative permittivity of 37.2, have been selected for microwave experiments.

Fig. 9 shows the schematic of experimental setup with MS sample. The samples were representing arrays of disk resonators with square lattices of various lattice constants. Arrays were fixed on paper boards by using double-sided sticky tape. As seen in Fig. 8, MS sample was placed between two identical X-band horn antennas (with operating frequencies from 8 GHz to 12 GHz), transmitting and receiving ones. Horn antennas were connected by standard 50-ohm coaxial cables to Agilent vector network analyzer with the frequency range 10 MHz - 20 GHz.

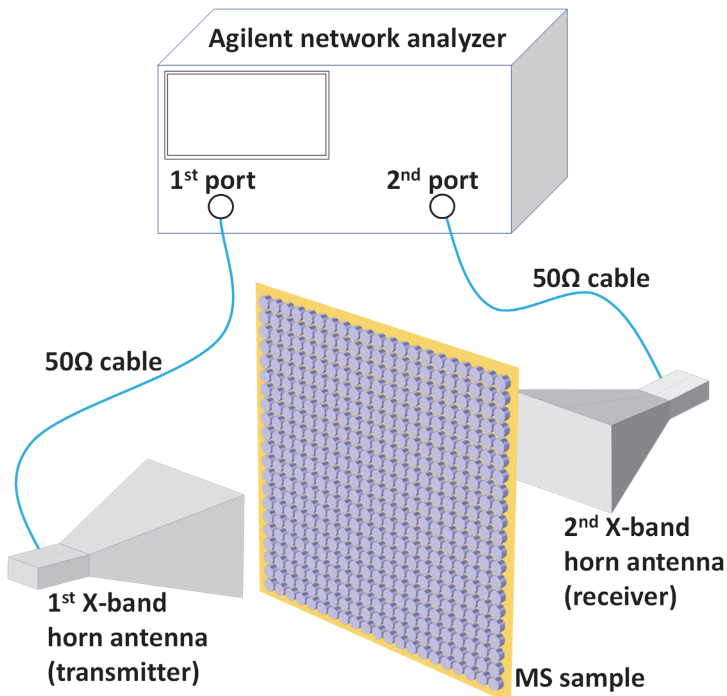


**FIG 9.** Schematic of experimental setup with the vector network analyzer, two X-band horn antennas, operating in the range of 8 GHz – 12 GHz, 50-ohm coaxial cables, and MS sample.

The responses of four MS samples with different lattice constants are presented in Fig. 10. As seen in the figure, simulated and experimental spectra of S-parameters demonstrated good agreement. In particular, at $\Delta$ = 8 mm, both spectra showed dual dips of S21 on the red side of the small peak with full transmission. This peak was located at about 11.6 GHz, i.e. very close to the frequency of electric dipolar resonance, detected in the probe signal spectrum in Fig. 8, while dual dips, associated with reflections from dipolar resonances, were related to magnetic response at about 11 GHz and to electric response at the frequency, close to 11.5 GHz. It should be noted that in our earlier works [12, 24] we observed appearance of related to dipolar resonances dual dips constants are presented in Fig. 10. As seen in the figure, simulated and experimental spectra of S-parameters demonstrated good agreement. In particular, at Δ = 8 mm, both spectra showed dual dips of S21 on the red side of the small peak with full transmission. This peak was located at about 11.6 GHz, i.e. very close to the frequency of electric dipolar resonance, detected in the probe signal spectrum in Fig. 8, while dual dips, associated with reflections from dipolar resonances, were related to magnetic response at about 11 GHz and to electric response at the frequency, close to 11.5 GHz. It should be noted that in our earlier works [12, 24] we observed appearance of related to dipolar resonances dual dips of S21 in relatively sparse MSs, composed of nano-resonators. These dips were related to conventional reflections from resonating nano-elements. As seen in Fig. 10, at decreasing the lattice constant to Δ = 7.3 mm, two dips in simulated spectra came closer to each other and at Δ = 7 mm, they merged in one dip. At decreasing the lattice constant down to Δ = 6.6 mm, S21 spectrum acquired the shape, quite similar to that of a typical EIT-type spectrum, with narrow peak of full transmission, located between symmetrical spectral parts with very low, opaque-type transmission. From the experimental S21 spectrum, obtained at Δ = 6.6 mm, it is not obvious that the spectral location of the peak with full transmission coincides with the position of electric dipolar resonance. However, comparison with the simulated probe signal spectrum, presented in Fig. 8 for MS with Δ = 6.6 mm, confirms this fact. Conducted experiments with microwave MSs have confirmed that the phenomenon of induced transparency, revealed originally by simulations for MSs, composed of silicon nano-resonators, can be also realized in dense MSs, composed of ceramic microwave resonators.

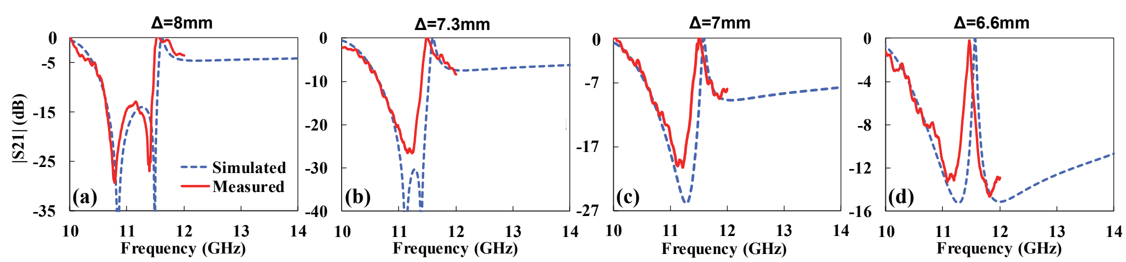


**FIG 10.** Measured and simulated |S21| spectra (in dB) for MSs, composed of dielectric disks with the diameters and the heights of, respectively, 6 mm and 3 mm and relative permittivity of 37.2 at four various lattice constants ranging from 8 mm to 6.6 mm.

## 7.5 Analysis of Electric Field Distributions and Search for Interference Partners at Fano Resonances

It is presumed that EIT is caused by interference between light-controlled processes, which are defined either by the specifics of excitation paths, as it is the case in atomic gases [1-3], or by the specifics of overlapping electromagnetic fields in arrays of coupled resonators, when excitation is provided by only one source, such as plane wave [4, 6]. In the case of

MSs, composed from resonators of only one type, the concept of coupling between resonators of various types, responsible for the formation of either dark, or bright modes, does not seem adequate. In literature, bright mode typically refers to a resonance, directly excited by incident radiation in one type of resonators of the EIT system. Dark mode is a secondary resonance in another type of resonators, excited by the bright mode through coupling effects. It is usually assumed that destructive interactions between bright and dark modes can induce the transparency of multi-resonator EIT system.

In order to explain appearance of induced transparency in MSs, composed of identical resonators, we had to look for alternative partners of interference. With this purpose, we analyzed Fano-type responses, observed at the studies of dipolar resonances in MSs. These responses often demonstrated zeros of the signals, characteristic for Fano resonances. As known, such zeros could be considered as the product of destructive interference, which, in the case of Fano resonances, is usually expected between wideband background/incident radiation and narrowband resonance scattering [6, 14]. To obtain more information about interference parties, we investigated Fano-type responses at some specific locations in MSs. Our previous studies of field distributions in planar cross-sections of MSs [12, 23, 24] have shown that in dense structures with square lattices useful information could be provided not only by the resonance fields inside DRs, but also by the fields, formed in the gaps between resonators in the X- and Y-oriented rows of DRs, as well as by the fields in the centers of geometric cells.

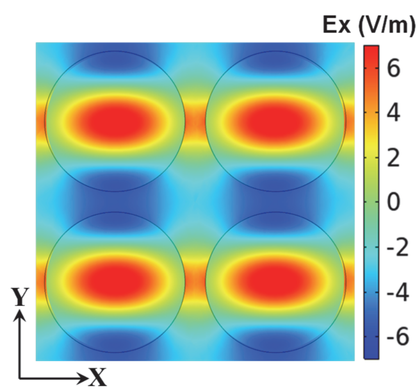


FIG 11. E-field distribution in central planar cross-section of a square-latticed MS at the wavelength of EDR's peak (λ = 634 nm). The heights and diameters of resonators are, respectively, 160 and 240 nm. The lattice constant is 275 nm.

Fig. 11 exemplifies electric field pattern, observed in planar XY cross-section of the geometric cell of MS with square lattice at the frequency of EDR. It is well seen that resonating dipoles are confined within DRs and provide strongest fields in DR centers. Electric fields in the gaps between resonators, arranged along X direction, with which dipolar electric fields are co-directed, look uniformly distributed within the gaps, even at increasing the lattice constant. This means that resonance fields do not fully control fields in the gaps. As it was found in numerical experiments, at bigger lattice constants, the strengths of gap fields could decrease, when the strengths of dipolar fields demonstrated almost no changes. It allows for suggesting that fields, seen in X-oriented gaps between DRs, include contributions from incident waves, which interfere with dipolar fields. In such case, these contributions from incident waves can be considered as background fields.

Although electric fields in the gaps between resonators, arranged along Y direction, look directed oppositely to dipolar fields formed inside the resonators, they are apparently defined by field lines, originating from dipoles and passing in air around the resonators [23]. The strength of these fields in each of Y-oriented gaps is the result of combining field lines, coming from dipoles formed in neighboring resonators arranged along Y direction. Therefore, the strength of these fields can be a measure of coupling between resonators.

Another specific feature of the field pattern in Fig. 11 is seen in relatively weak blue colored fields in the centers of MS geometric cells. These fields are co-directed with the fields in Y-oriented gaps, i.e. are opposite to dipolar fields formed inside resonators. However, they do not seem to be of the same origin, as that of the gap fields. At bigger lattice constants, these fields were found to strengthen and to contribute to the formation of specific field distributions, represented by parallel X-oriented field lines of alternating polarity and lattice-defined periodicity. Such type of distributions could be related to the formation of standing surface waves.

The presented analysis shows that field patterns, similar to that given in Fig. 11, integrate electric fields of different origins. The studies of these fields should be helpful for deeper insight into the physics of wave processes in MSs.

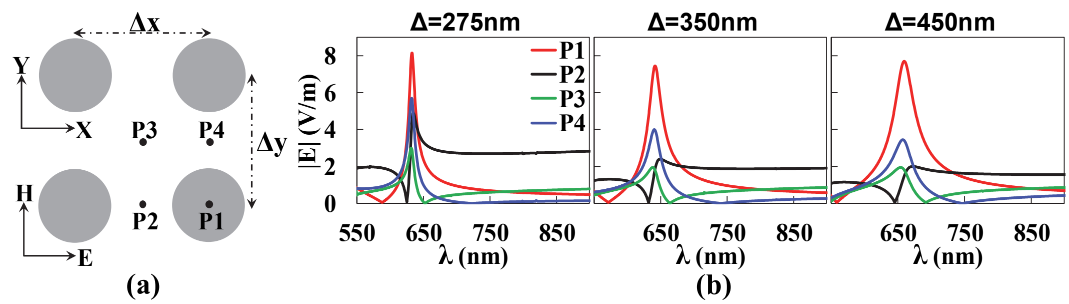


FIG 12. (a) Geometric schematic of MS lattice cell with four points, chosen for placing E-field probes in planar MS cross-section; (b) spectra of signals from E-field probes, placed according to the schematic shown in (a) in MSs with different lattice constants Δ. Resonator heights are 160 nm, and their diameters are 240 nm.

Fig. 12 uses the schematic of one geometric cell of MS with square lattice to show the positions, which were chosen for placing E-field probes. Point P1, located in the center of DR, is used for characterizing the formation of dipolar resonances (EDRs). Point P2, placed in the middle of the gap between resonators arranged along X direction, can describe interstitial fields in X-oriented rows of DRs. Point P3 is used for judging about the surface wave contribution in field distributions. Point P4 is employed to characterize interstitial fields in Y-oriented rows of resonators.

As seen in Fig. 12, the spectra of signals from all probes in MSs with different lattice constants demonstrate features, typical for Fano-type resonances, and resonance maxima look located close to the wavelengths, characteristic for spectral positions of EDRs. In points P1, P3, and P4, beyond the spectral region defined by EDR-related phenomena, probe signals do not demonstrate any specific features, except for decaying, while in point P2, on the contrary, probe signals conserve significant strengths and remain stable in wide spectral ranges from 700 nm to 900 nm and above. The intensity of these stable signals is maximal in densest structures, while it decreases significantly in MSs with bigger lattice constants. The observed specifics of P2 signals justify the suggestion that they originate from incident waves, while their stable values in air-filled interstitials can be defined by incident fields distributed in non-uniform air-dielectric medium. At increasing the $\Delta$ values, the voltage associated with incident fields has to be applied to sparser rows of resonators with wider air gaps that explains decreasing the field magnitudes in air gaps. This consideration is in favor of earlier made suggestion that the fields in X-oriented gaps can represent background fields, required for the formation of Fano-type responses.

## 7.6 Fano Resonances and Interference Processes

To analyze Fano resonances, revealed by signals from four E-field probes, we consider presented in Fig. 13 spectra of probe signal magnitudes and phases, along with the field patterns, observed at zero signals of respective Fano line-shapes. The data presented in Fig. 13 were obtained for the dense MS with the lattice constant of 275 nm.

We start from analyzing the spectra of probe signals and field patterns, to draw first conclusions about interference processes in MSs under study, and then employ the spectra of probe signal phases for providing deeper insight. As seen in Fig. 13 (a), the probe signal spectrum, obtained at point P1, demonstrates typical for EDR resonance peak at 634 nm with characteristic for Fano-type resonance zero signal in the line-shape at 588 nm, i.e. far from the peak. Since the strength of EDR fields at 588 nm is significantly decreased, it can be expected that the background radiation, destructive interference of which with resonance fields causes zero in the line-shape of P1 signal, is also weak. The data presented in Fig. 13 (b), do not contradict these expectations, despite seemingly strong background fields in air-filled interstitials of X-oriented rows of DRs at 588 nm. In fact, the strength of background fields inside DRs, where they compete with resonance fields, should be much smaller than it is in air, since the value of DR’s dielectric constant is equal to 12.25.

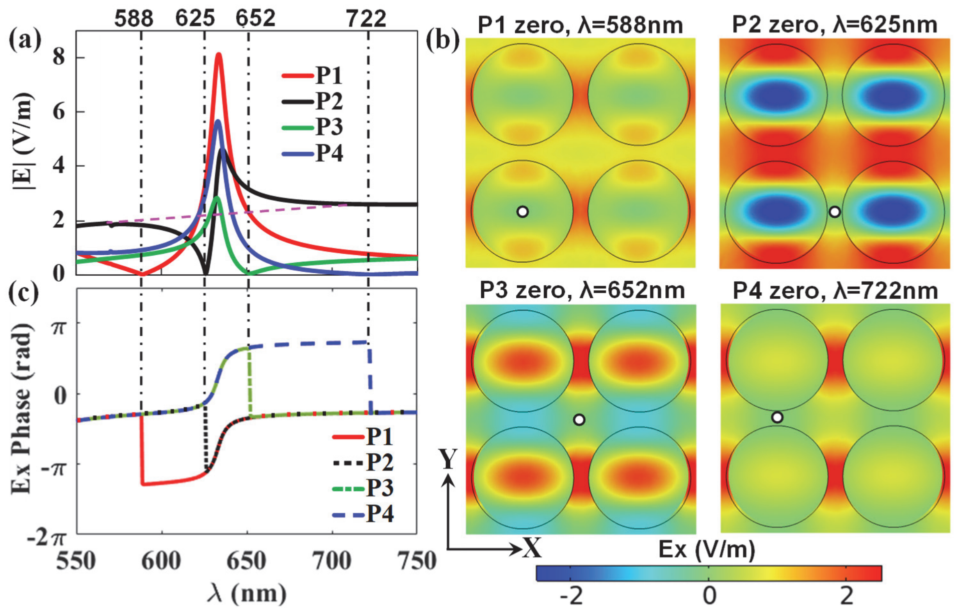


FIG 13. (a) Spectra of E-field probe signals in four points of MS geometric cell (see Fig. 12 (a)); (b) field patterns in planar cross-sections of MS at wavelengths of zero signals in line-shapes of Fano resonances (see Fig. 13 (a)); and (c) spectra of probe signal phases in four points. Circles in field patterns exemplify zero field locations. MS lattice constants are equal to 275 nm, DR heights are 160 nm, and DR diameters are 240 nm. Dashed purple line in Fig. 13 (a) shows extension of the background portion of P2 signal.

The spectrum registered at point P4, which should characterize dipolar fields, circling around resonators, also demonstrates a peak at the EDR wavelength of 634 nm. However, the respective Fano-type line-shape at point P4 has its zero in the red portion of the spectrum, i.e. at 722 nm that agrees with the opposite polarity of fields in Y-oriented gaps, with respect to the polarity of dipolar fields inside resonators. The spectrum of P2 signal reveals classic Fano-type line-shape in the vicinity of EDR. It is characterized by a peak on the red side of EDR and by a deep drop down to zero on the blue side of EDR. These features allow for suggesting that Fano resonance in point P2 is defined by interference of background radiation and signals, radiated by EDRs. At $\lambda = 625$ nm, corresponding to the location of zero in the Fano line-shape at point P2, the respective field pattern in Fig. 13 (b) demonstrates zero fields in X-oriented gaps that tells about total suppression of background/incident radiation in these gaps by the fields, radiated from resonating dipoles. Destructive interference of two fields is the result of their $\pi$-value phase difference, which will be confirmed below at the analysis of phase changes given in Fig. 13 (c).

It should be accentuated here that competing wave processes, which define the appearance of Fano resonances, should be in phase at constructive interference and should be shifted by $\pi$ radians at destructive interference. Therefore, if one of two processes does not change the phase in the spectral range, corresponding to the transition from constructive to destructive interference at Fano resonance, then the second process must experience phase shift by $\pi$ radians in the same spectral range. In the case under consideration, the formation of dipolar resonances should be accompanied by changes of the phase of resonance oscillations by $\pi$ in the spectral range between red and blue ends of the resonance line-shape. This knowledge should be kept in mind at the analysis of phase changes, which probe signals experience at the formation of Fano responses in the chosen four points of MSs.

As seen in Fig. 13 (c), the spectra of probe signal phases at Fano resonances in all four points of MS cross-section, experience at least one jump up by $\pi$ radians at moving along the spectra from longer to shorted wavelengths. However, spectral positions of these jumps are specific for probe locations, since jumps occur at the wavelengths, corresponding to zeros in the line-shapes of respective Fano resonances.

In addition to sharp jumps, all spectra of probe signal phases demonstrate gradual decrease of signal phases by $\pi$ radians in the range of wavelengths, corresponding to the EDR region in P1 spectrum. This decrease is apparently due to switching of the phase of resonance oscillations by $\pi$ radians at dipolar resonances. The fact, that similar changes are observed in P2, P3, and P4 spectra, indicates that they are controlled by EDR-caused radiation. In difference from gradual changes, sharp jumps by $\pi$ radians in the spectra of probe signal phases indicate that at zero signals in Fano line-shapes, defined by destructive interference of competing wave processes, there is a change of the leader in this competition.

Clarification of the nature of competing wave processes can be exemplified by the case of P2 signal. It is seen in Fig. 13 (c) that, while the phase of P2 signal coincides with the phase of P1 signal in the range 750 nm > $\lambda$ > 625 nm, the phases of two signals become different by $\pi$ radians after the $\pi$-value jump up of P2 phase at $\lambda$ = 625 nm. Sin-phase changes of P1 and P2 signals in the red portion of EDR-related spectral range indicate that in this spectral portion, P2 signal is controlled by EDR, as it is expected, considering the radiation from resonating dipoles. The fields, induced by the radiation, apparently define peaking of P2 signal at $\lambda$ = 636 nm that marks the maximal result of constructive interference. Subsequent drop of P2 signal at shorter wavelengths should be related to conversion to destructive interference between background radiation and fields, induced by radiation from EDRs, since the latter gradually switches its phase by $\pi$ radians. In difference from resonance fields, background radiation experiences no phase switching and, therefore, finally becomes $\pi$ radians different in phase with respect to resonance fields on the blue side of EDR. This fact defines mentioned above destructive interference between background radiation and fields induced by EDR that leads to zero probe signal in X-oriented gaps (point P2) at $\lambda$ = 625 nm. Since gradual switching of the phase of P1 signal by $\pi$ is almost completed at the wavelengths, corresponding to the $\pi$ radians jump in P2 phase spectrum, this jump cannot be related to the resonance phenomenon. Instead, it is reasonable to suggest that the jump in P2 spectrum is the result of prevailing of background fields over decaying fields induced by resonance radiation on the blue side of EDR. It is obvious that at λ < 625 nm, decaying radiation from EDR becomes incapable of balancing the background radiation, so that the latter starts to control the phase of P2 signal.

Exemplified above approach to analyzing spectral changes of probe signal phases can be similarly employed for clarifying the nature of processes, defining the formation of Fano resonance at other probe locations.

## 7.7 Fano Resonances and Induced Transparency

Conducted analysis of Fano resonances in MSs under study, helped us to reveal the specifics of interference processes in these structures. In order to relate these processes to appearance of the EIT phenomenon, it is worth recalling the approaches, used in the first works on EIT [1-3]. Fig. 14 shows a typical schematic, employed for explaining zero energy absorption at EIT in atomic gases. The central idea was that no energy spending could be provided due to destructive interference between the competing transitions 1-2 and 3-2.

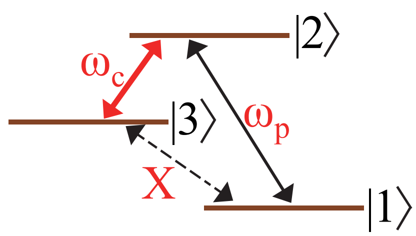


FIG 14. Three levels schematic used to explain the role of coupled transitions between states 3 and 2 for eliminating the energy absorption.

Thus, quantum interference was assumed capable of controlling the entire optical response, in particular, of eliminating the absorption and the refraction (linear susceptibility) at the resonant frequency. In such case, from the side of observer, located in state 1, the situation could be seen as absence of any transitions between state 1 and state 3. The reality of such situation was in details analyzed in [28].

Considering EIT in MSs under study, an analogy with the case of atomic gases could be seen in destructive interference between background/incident radiation and radiation from dipolar resonances, which was shown to be critical for the signals in point P2. In fact, for an observer, located in point P2, MS response at zero signal in the Fano line-shape will be seen as identical to the case with no background radiation and, so, with no presence of incident waves in the MS. In this case, the observer should not expect any absorption or refraction of incident waves, as well as their reflection (at zero susceptibility and zero index). Therefore, it seems logical to assume that at zero signal in the Fano line-shape in point P2, nothing prevents waves from transmitting without losses through MS and, so, the conditions for EIT could be realized.

It is worth pointing out here that the spectral distance between the positions of EDR and zero signal in Fano line-shape in point P2 is just a few nanometers at $\Delta = 275$ nm. Therefore, in S-parameter spectra, the EIT position appears almost indistinguishable from the EDR position. More accurate studies of EDR and EIT spectral positions at varying the $\Delta$ values are desired to additionally verify the character of correlation between two phenomena.

It could also be noticed that we did not observe EIT-like phenomena associated with magnetic dipolar resonances (MDRs). The reason for this could be seen in Fig. 3. As seen in the figure, in dense MSs, Q-factors of MDRs are very low. In sparse MSs, Q-factors of MDRs become higher, however, sparse MSs do not create conditions for superposition of fields required for the formation of Fano-resonances.

## 7.8 Conclusions

Numerical experiments with MSs, composed of identical cylindrical silicon nano-resonators, have shown that these structures can demonstrate full narrowband transparency for normally incident plane waves at the frequencies of EDRs. In MSs with square lattices, this EIT-like phenomenon has been observed only at the lattice constants in the range between 275 nm and 325 nm, i.e. in densely packed MSs

The studies of electric field distributions in planar cross-sections of MSs and of signal spectra from E-field probes, placed in characteristic points of MS's unit cells helped us to identify physical processes, defining the specifics of Fano resonances observed at various probe locations. In particular, it was shown that Fano resonances, detected in the gaps between resonators, arranged along E-field direction, were controlled by interference between background radiation and waves, radiated by resonance fields, formed inside DRs. Well known switching of the phase of resonance oscillations by π radians at the resonance frequency made this interference transforming from constructive to destructive at passing the resonance. Destructive interference provided suppression of background radiation and full MS transparency at the frequencies of zero signals in Fano line-shapes, registered at the described above locations. The wavelengths of spectral positions of the above zero signals were found to be just about several nanometers shorter than the EDR wavelengths that created an illusion of coincidence of EIT and EDR effects.

## 7.9 Acknowledgement

The authors would like to thank Fatemeh Safari for her collaboration at performing microwave experiments.

# References


1. O. A. Kocharovskaya and Y. I. Khanin, “Population trapping and coherent bleaching of a three-level medium by a periodic train of ultrashort pulses”, Sov. Phys. JETP, 63, 945, 1986.

2. K. J. Boller, A. Imamoglu, and S. E. Harris, “Observation of electromagnetically induced transparency”, Physical Review Letters, 66, pp. 2593–2596, 1991.

3. S. E. Harris, “Electromagnetically induced transparency”, Phys. Today, 50 (7), 36, 1997.

4. N. Papasimakis, V. A. Fedotov, N. I. Zheludev, and S. L. Prosvirnin, “A metamaterial analog of electromagnetically induced transparency”, Physical Review Letters, 101 (25), 253903, 2009.

5. S. Zhang, D. A. Genov, Y. Wang, M. Liu, and X. Zhang, “Plasmon-induced transparency in metamaterials”, Physical Review Letters, 101, 047401, 2008.

6. N. Papasimakis and N. I. Zheludev, “Metamaterial-induced transparency: sharp Fano resonances and slow light”, Optics and Photonics News, 20 (10), pp. 22-27, 2009.

7. S. Y. Chiam, R. Singh, C. Rockstuhl, F. Lederer, W. Zhang, and A. A. Bettiol1, “Analogue of electromagnetically induced transparency in a terahertz metamaterial”, Physical Review B, 80, 153103, 2009.

8. Y. Yang, I. I. Kravchenko, D. P. Briggs, and J. Valentine, “All-dielectric metasurface analogue of electromagnetically induced transparency”, Nature Communications, 5, 5753, 2014.

9. B. Han, X. Li, C. Sui, J. Diao, X. Jing, and Z. Hong, “Analog of electromagnetically induced transparency in an E-shaped all-dielectric metasurface based on toroidal dipolar response”, Optical Materials Express, 8 (8), 2197, 2018.

10. M. Qin, C. Pan, Y. Chen, Q. Ma, S. Liu, E. Wu, and B. Wu, “Electromagnetically induced transparency in all-dielectric U-shaped silicon metamaterials”, Applied Sciences, 8, 1799, 2018.

11. L. Garrido Alzar, M. A. G. Martinez, and P. Nussenzveig, “Classical analog of electromagnetically induced transparency”, American Journal of Physics, 70 (37), 2002.

12. S. Jamilan, G. Semouchkin, N. P. Gandji, and E. Semouchkina, “Specifics of scattering and radiation from sparse and dense dielectric meta-surfaces”, Journal of Applied Physics, 125 (16), 163106, 2019.

13. S. Jamilan, G. Semouchkin, N. P. Gandji, and E. Semouchkina, “Electromagnetically induced transparency and lattice resonances in metasurfaces composed of silicon nanocylinders”, AES 2019, Lisbon, Portugal, July 2019.

14. B. Luk'yanchuk, N. I. Zheludev, S. A. Maier, N. J. Halas, P. Nordlander, H. Giessen, and C. C. Tow, “The Fano resonance in plasmonic nanostructures and me”, Nature Materials, 9 (9), 707–715, 2010.

15. R. Pant, S. Shakthi, and A. B. Yelikar, “Wideband excitation of Fano resonances and induced transparency by coherent interactions between Brillouin resonances”, Scientific Reports, 8, 9175, 2018.

16. L. V. Hau, S. E. Harris, Z. Dutton, and C. H. Behroozi, “Light speed reduction to 17 metres per second in an ultracold atomic gas”, Nature*,* 6027, p. 594, 1999.

17. D. F. Phillips, A. Fleischhauer, A. Mair, R. L. Walsworth, and M. D. Lukin, “Storage of light in atomic vapor”, Physical Review Letters, 86 (5), 2001.

18. M. F. Yanik and S. Fan, “Stopping light in a waveguide with an all-optical analog of electromagnetically induced transparency,” Physical Review Letters, 93, 233903, 2004.

19. R. S. Tucker, P. C. Ku, and C. J. Chang-Hasnain, “Slow-light optical buffers: capabilities and fundamental limitations”, Journal of Lightwave Technology, 23 (12), pp. 4046-4066, 2005.

20. S. A. Schulz, A. A. Liles, and L. O’Faolain, “Tunable optical buffer through an analogue to electromagnetically induced transparency in coupled photonic crystal cavities”, ACS Photonics, 5 (5), pp. 1827–1832, 2018.

21. H. Schmidt and R. J. Ram, “All-optical wavelength converter and switch based on electromagnetically induced transparency”, Applied Physics Letters, 76, 3173, 2000.

22. G. Sun, S. Peng, X. Zhang, and Y. Zhu, “Switchable Electromagnetically induced transparency with toroidal mode in a graphene-loaded all-dielectric metasurface”, Nanomaterials (Basel), 10 (6), 1064, 2020.

23. N. P. Gandji, G. Semouchkin, and E. Semouchkina, "Electromagnetic responses from planar arrays of dielectric nano-disks at overlapping dipolar resonances", IEEE Research and Applications of Photonics in Defense Conf. (RAPID), 2018.

24. S. Jamilan, N. Gandji, G. Semouchkin, F. Safari, and E. Semouchkina, "Scattering from dielectric metasurfaces in optical and microwave ranges", IEEE Photonics Journal*,* 11 (3), 2019.

25. Staude, A. E. Miroshnichenko, M. Decker, N. T. Fofang, S. Liu, E. Gonzales, J. Dominguez, T. S. Luk, D. N. Neshev, I. Brener, and Y. Kivshar, "Tailoring directional scattering through magnetic and electric resonances in subwavelength silicon nanodisks", ACS Nano, 7 (9), 7824, 2013.

26. I. Kuznetsov, A. E. Miroshnichenko, M. L. Brongersma, Y. S. Kivshar, and B. Luk'yanchuk, "Optically resonant dielectric nanostructures", Science, 354, 6314, 2016.

27. S. Jamilan and E. Semouchkina, "Lattice resonances in metasurfaces composed of silicon nano-cylinders", 14th Intern. Congress on Artificial Materials for Novel Wave Phenomena – Metamaterials, N.Y., USA, 2020.

28. M. Fleischhauer, A. Imamoglu, and J. P. Marangos, "Electromagnetically induced transparency: optics in coherent media", Review of Modern Physics, 77, 633, 2005.

29. S. Jamilan, G. Semouchkin, and E. Semouchkina, "Analog of electromagnetically induced transparency in metasurfaces composed of identical dielectric disks", Journal of Applied Physics, 129 (6), 063101, 2021.

# 8 Summary and Future Works

## 8.1 Summary

In Chapter 1, we introduced the concepts of transformation optics (TO), which presents a new tool for developing electromagnetic and photonic devices with advanced functionalities, in particular invisibility cloaks. We explained that realization of TO-based devices requests designing artificial media with unusual properties. While conventional metamaterials (MMs) fail to provide desired responses at high frequencies, artificial media composed from all-dielectric constituents such as dielectric photonic crystals (PhCs) can be another candidate for developing TO-based devices. Furthermore, we explained that metasurfaces (MS) made of 2D arrays of dielectric resonators (DRs) are another class of all-dielectric artificial media for employment in flat devices controlling propagation and scattering of electromagnetic waves.

Chapter 2 described our approach for realizing TO-prescribed cylindrical invisibility cloak by using anisotropic PhCs. First, we clarified the functions of TO-prescribed azimuthal and radial indices having, respectively, near-zero and bigger than unity values. It was observed that both index dispersions are essential for accelerating waves travelling in the cloak media and for properly turning waves around hidden objects. Then, we studied responses of anisotropic PhCs composed from dielectric rod arrays with rectangular lattices under TM polarized illumination. We found out that frequency-dependencies of directional refractive indices of such PhCs in their 2nd transmission bands demonstrate values that are compatible with TO-prescribed azimuthal and radial index dispersions. However, at a reasonable thickness of the cylindrical cloak medium, it was seen that TO prescribes bigger radial indices in inner layers of the cloak, overstepping the degree of index anisotropy in rectangular lattice PhCs. We proposed to reduce the ideal TO prescriptions to mitigate the problem. Our analysis verified that a cloak medium with precisely modified radial index dispersion providing smaller values in inner layers of the cloak and bigger values in outer layers of the cloak, in comparison with ideal TO prescriptions for radial index, provides a nearly perfect cloaking effect. For realizing cloak prototype, we approximated the reduced index dispersion with a step-function. Then, we found lattice parameters of rectangular lattice PhCs that could provide approximated indices at the operating frequency. We coiled fragments of these PhCs around a metal cylinder in concentric circular arrays. In the cloak medium, short sides of rectangular cells were oriented along azimuthal direction, while long sides of the cells were directed along radial direction. Rods were infinite along z-axis. Obtained wave patterns showed that cylindrical cloak media composed from dielectric rod arrays with rectangular lattices could provide desired wave-front restoration at the operating frequency. Scatterings of the metal cylinder was also significantly reduced by the designed cloak medium.

In Chapter 3, considering the challenges met at realizing TO prescribed radial indices, we proposed to refuse from TO prescriptions in the cylindrical cloak medium and employ self-collimation (SC) phenomenon in PhCs for turning waves around hidden object. We bent

PhC fragment comprising four identical arrays of dielectric rods with square lattice to realize the SC effect. We also designed transformation regions in the left and right sides of the cylindrical cloak medium to transform the wave movement from straight in free space into curvilinear in the SC-part of the cloak. These transformation parts were realized by using dielectric rod arrays with rectangular lattices. Obtained results revealed that SC-based cylindrical cloak media can provide cloaking effect. Our designed SC-based cylindrical cloak had a smaller thickness, i.e. less ratio of outer/inner radii, in comparison with TO-based cloak realized in Chapter 2. Furthermore, our SC-based cloak media properly worked under plane wave incidence, while devices operating based on SC phenomenon usually work for electromagnetic beams.

In Chapter 4, we realized the media with unidirectional high-anisotropic near-zero refractive index properties. In PhCs with rectangular-lattices composed of dielectric rod arrays, we found that for specifically selected lattice parameters, superluminal propagation with near-zero refractive indices could be formed along short sides of PhC's cells, while propagation along long sides of the cells was totally prohibited. This phenomenon was detected at the lower edge of 2nd transmission band considering TM waves moving along short sides of the PhC's cells. Such PhCs demonstrated flat equi-frequency contours (EFCs) in the operating frequency range. Flat EFCs were expected to provide substantial collimation effect. For verifying the response, we placed a fragment of high-anisotropic NZRI PhC in front of a divergent radiation. It could effectively collimate, confine, and guide the incident wave along short sides of the PhC's cells.

In Chapter 5, we investigated resonance and scattering phenomena in metasurfaces (MSs) formed from 2D arrays of dielectric resonators (DRs). We studied the electric and magnetic dipolar resonances (EDR and MDR) in a single subwavelength dielectric cylinder by controlling their spectral positions. We varied the height of the cylinder at a fixed diameter. The optimum directional scattering from a single dielectric disk was detected when there was a specific spectral distance between peak frequencies of EDR and MDR and they were not coinciding, as often assumed in literature. In addition, we altered the periodicity of dielectric disk arrays in MSs and characterized their responses in terms of scattering and radiation. Our results demonstrated that periodicity of arrays significantly affected electromagnetic responses of MSs. In particular, in densely packed MSs, a sharp transmission peak was excited at the frequency of EDR, opposing conventionally expected response of EDR. We considered this type of response in dense MSs as analogous to the phenomenon of electromagnetically induced transparency (EIT).

In Chapter 6, we explored the interactions between EDRs/MDRs formed inside DRs in MSs with the lattice resonances (LRs). We increased the lattice constants of dielectric disk arrays up to values where it was comparable to the wavelengths of ED and MD resonances. This resulted in red shifting of the EDR and MDR frequencies at approaching Rayleigh Anomaly (RA). We obtained near-field patterns and observed that formation of LRs is associated with excitation of strong field spots in the gaps nearby edges of DRs. We suggested that coherent oscillations of these field spots with dipolar resonance fields that were formed inside DRs, enhanced the effective wavelengths of oscillations and led to red shifting of elementary Mie resonances at emergence of LRs. Our results also illustrated the changes in scattering responses of MSs affected by interactions of LRs with EDRs and MDRs.

Results presented in Chapter 7 discussed the nature of extraordinary narrow-band transmission that was detected in dense MSs at EDR. In literature, devices with EIT-like responses typically have complex designs. Our results demonstrated that EIT-like response could be realized in simple MSs composed of identical dielectric disks. We studied the formation of destructive/constructive interferences and Fano resonances in dense MSs by recording electric field intensity and phase signals in several spatial points chosen in MS Plane. Analysis of interactions between resonant fields inducing $\pi$ radian phase shifts clarified the origin of Fano responses. Diminishing background scattering nearby EDR's frequency, rendered the dense MS transparent.

## 8.2 Future Works

Described above studies can be inspiring for future potential works at designing and utilizing all-dielectric artificial media. We used anisotropic PhCs with rectangular lattice arrays of dielectric rods for designing cloaks and collimators. We suggest using PhCs with rectangular lattices in other advanced electromagnetic and photonic devices such as beam splitters and modulators. A collimator can be engineered to enhance the far-field directivity of an antenna radiation and to boost the efficiency and connectivity in a communication system. We designed our PhC media with mm-sized ceramic rods with permittivity of 37.2 for conducting experiments in microwave regime. However, designing anisotropic PhC media from silicon nano-rods appears important for optical applications. At designing the SC-based cloak, we obtained a mismatch between indices of SC and TO parts. Improving the design of the cloak to mitigate this problem can lead to further reduction of hidden object's scattering.

We studied the responses of infinitely periodic dielectric MSs at employing single unit-cell models with periodic boundary conditions. However, practical applications of MSs incorporate finite MS samples. Therefore, it is imperative to explore the responses of finite fragmental MSs and characteristics of the formation of MDRs, EDRs, and LRs in them. We observed that an EIT-like response emerged at EDR frequencies in dense MSs. Investigating an opportunity for realizing such effect at MDRs in MSs can be the subject of future research. It was seen that formation of LRs created high intensity localized field spots in the gaps nearby DRs' edges in the MSs. Benefits of these field spots can be considered for advancing super-oscillatory applications that request localized intense fields with a low-loss response.

We used anisotropic PhCs made of infinite rods for realizing invisibility cloaks. Therefore, our designed cloak media were bulky. We propose to realize new types of compact invisibility cloaks by employing and designing dielectric MSs. It is worth noting that it was seen that at specific frequencies, back scattering of MSs was suppressed.

# A Letters of Permission

## A.1 Permission to reprint the article from IOP Publishing

Can I use my article as part of my thesis/dissertation after it has been published with IOP?

When you transfer the copyright in your article to IOP, we grant back to you certain rights, including the **right to include all or part of the Final Published Version of the article within any thesis or dissertation.** Please note you may need to obtain separate permission for any **third party content** you include within your article. Please include citation details, "© IOP Publishing. Reproduced with permission. All rights reserved". The only restriction is that if, at a later date, you want to share your thesis/dissertation online, permission to include the Final Published Version of the article within the online version of your thesis/dissertation will need to be sought from IOP. Alternatively, you may choose to replace the article in the online version of your thesis/dissertation with either a Preprint or the Accepted Manuscript version (if the embargo period has passed), provided you comply with our Preprint or Author Rights: Accepted Manuscript policy, as relevant.

CCC Marketplace™

This is a License Agreement between Saeid Jamilan ("User") and Copyright Clearance Center, Inc. ("CCC") on behalf of the Rightsholder identified in the order details below. The license consists of the order details, the CCC Terms and Conditions below, and any Rightsholder Terms and Conditions which are included below.

All payments must be made in full to CCC in accordance with the CCC Terms and Conditions below.

| | | | |
|---|---|---|---|
| Order Date | 24-Jul-2021 | Type of Use | Republish in a thesis/dissertation |
| Order License ID | 1135634-1 | Publisher | IOP Publishing |
| ISSN | 2040-8986 | Portion | Chapter/article |

LICENSED CONTENT

| | | | |
|---|---|---|---|
| Publication Title | Journal of Optics | Rightsholder | IOP Publishing, Ltd |
| Date | 01/01/2010 | Publication Type | e-Journal |
| Language | English | URL | http://iopscience.iop.org/2040-8986/ |
| Country | United Kingdom of Great Britain and Northern Ireland | | |

REQUEST DETAILS

| | | | |
|---|---|---|---|
| Portion Type | Chapter/article | Rights Requested | Main product |
| Page range(s) | 1-9 | Distribution | Worldwide |
| Total number of pages | 9 | Translation | Original language of publication |
| Format (select all that apply) | Print, Electronic | Copies for the disabled? | No |
| Who will republish the content? | Author of requested content | Minor editing privileges? | No |
| Duration of Use | Life of current edition | Incidental promotional use? | No |
| Lifetime Unit Quantity | Up to 499 | Currency | USD |

NEW WORK DETAILS

| | | | |
|---|---|---|---|
| Title | DEVELOPING ELECTROMAGNETIC AND PHOTONIC DEVICES BY USING ARTIFICIAL DIELECTRIC MATERIALS | Institution name | Michigan Technological University |
| | | Expected presentation date | 2021-08-02 |
| Instructor name | Saeid Jamilan | | |

| | | | |
|---|---|---|---|
| Title, description or numeric reference of the portion(s) | Spatial Dispersion of Index Components Required for Building Invisibility Cloak Medium from Photonic Crystals | Title of the article/chapter the portion is from | N/A |
| Editor of portion(s) | N/A | Author of portion(s) | S. Jamilan, G. Semouchkin, N. P. Gandji, E. Semouchkina |
| Volume of serial or monograph | N/A | Issue, if republishing an article from a serial | N/A |
| Page or page range of portion | 1-9 | Publication date of portion | 2018-03-21 |

## A.2 Permission to reprint the article from IEEE Publishing

### Thesis / Dissertation Reuse

**The IEEE does not require individuals working on a thesis to obtain a formal reuse license, however, you may print out this statement to be used as a permission grant:**

*Requirements to be followed when using any portion (e.g., figure, graph, table, or textual material) of an IEEE copyrighted paper in a thesis:*

1) In the case of textual material (e.g., using short quotes or referring to the work within these papers) users must give full credit to the original source (author, paper, publication) followed by the IEEE copyright line © 2011 IEEE.
2) In the case of illustrations or tabular material, we require that the copyright line © [Year of original publication] IEEE appear prominently with each reprinted figure and/or table.
3) If a substantial portion of the original paper is to be used, and if you are not the senior author, also obtain the senior author's approval.

*Requirements to be followed when using an entire IEEE copyrighted paper in a thesis:*

1) The following IEEE copyright/ credit notice should be placed prominently in the references: © [year of original publication] IEEE. Reprinted, with permission, from [author names, paper title, IEEE publication title, and month/year of publication]
2) Only the accepted version of an IEEE copyrighted paper can be used when posting the paper or your thesis on-line.
3) In placing the thesis on the author's university website, please display the following message in a prominent place on the website: In reference to IEEE copyrighted material which is used with permission in this thesis, the IEEE does not endorse any of [university/educational entity's name goes here]'s products or services. Internal or personal use of this material is permitted. If interested in reprinting/republishing IEEE copyrighted material for advertising or promotional purposes or for creating new collective works for resale or redistribution, please go to http://www.ieee.org/publications_standards/publications/rights/rights_link.html to learn how to obtain a License from RightsLink.

If applicable, University Microfilms and/or ProQuest Library, or the Archives of Canada may supply single copies of the dissertation.

## A.3 Permission to reprint the article from SPIE Publishing

Dear Saeid,

Thank you for seeking permission from SPIE to reprint material from our publications. SPIE shares the copyright with you, so as author you retain the right to reproduce your paper in part or in whole.

Publisher's permission is hereby granted under the following conditions:

(1) the material to be used has appeared in our publication without credit or acknowledgment to another source; and

(2) you credit the original SPIE publication. Include the authors' names, title of paper, volume title, SPIE volume number, and year of publication in your credit statement.

Best wishes on your dissertation. Please let me know if I may be of any further assistance.

Best,

Katie Sinclair

Editorial Assistant, Publications

SPIE – the international society for optics and photonics

## A.4 Permission to reprint the article from OSA Publishing

Dear Saeid,

Thank you for contacting The Optical Society.

For the use of material from S. Jamilan, E. Semouchkina, "Collimation Effect in Strongly Modulated Anisotropic Photonic Crystals with Near-Zero Refractive Indices," 2021 CLEO Conference, Fundamental Sciences, 2021:

> OSA only has copyright for the compilation of the conference proceedings, not the individual papers themselves. As the authors retain copyright to the individual paper, an OSA credit statement is not needed, although we do request a complete citation be included in any publication or adjacent to any posting.

While your publisher should be able to provide additional guidance, OSA prefers the below citation formats:

> For citations in figure captions:
>
> [Reprinted/Adapted] with permission from [ref #] © The Optical Society. (Please include the full citation in your reference list)
>
> For images without captions:
>
> Journal Vol. #, first page (year published) An example: Biomed. Opt. Express 6, 793 (2015)

Please let me know if you have any questions.

Kind Regards,

Hannah Greenwood

Hannah Greenwood

July 19, 2021

Authorized Agent, The Optical Society

## A.5 Permission to reprint the article from AIP Publishing

Authors do **not** need permission from AIP Publishing to:

- quote from a publication (please include the material in quotation marks and provide the customary acknowledgment of the source)
- reuse any materials that are licensed under a Creative Commons CC BY license (please format your credit line: "Author names, Journal Titles, Vol.#, Article ID#, Year of Publication; licensed under a Creative Commons Attribution (CC BY) license.")
- reuse your own AIP Publishing article in your thesis or dissertation (please format your credit line: "Reproduced from [FULL CITATION], with the permission of AIP Publishing")
- reuse content that appears in an AIP Publishing journal for republication in another AIP Publishing journal (please format your credit line: "Reproduced from [FULL CITATION], with the permission of AIP Publishing")
- make multiple copies of articles–although you must contact the Copyright Clearance Center (CCC) at www.copyright.com to do this

Dear Dr. Jamilan:

You are permitted to include your published article in your thesis, provided you also include a credit line referencing the original publication.

Our preferred format is (please fill in the citation information):

"Reproduced from [FULL CITATION], with the permission of AIP Publishing."

If the thesis will be available electronically, please include a link to the version of record on AIP Publishing's site.

Please let us know if you have any questions.

Sincerely,

**Susann LoFaso**

*Manager, Rights & Permissions*

**AIP Publishing**

1305 Walt Whitman Road | Suite 300 | Melville NY 11747-4300 | USA